ATOMISTIC SIMULATIONS AND COMPUTATIONS OF CLAY MINERALS AT GEOLOGIC CARBON SEQUESTRATION CONDITIONS

by

Meysam Makaremi

BSc, Najafabad Azad University, 2003

MSc, University of Tehran, 2007

Submitted to the Graduate Faculty of

the Swanson School of Engineering in partial fulfillment

of the requirements for the degree of

Doctor of Philosophy

University of Pittsburgh

2015

UNIVERSITY OF PITTSBURGH

SWANSON SCHOOL OF ENGINEERING

This dissertation was presented

by

Meysam Makaremi

It was defended on

March 18th 2018

and approved by

Albert C. To, Ph.D., Associate Professor, Department of Mechanical Engineering and Materials Science

Kenneth D. Jordan, Ph.D., Richard King Mellon Professor and Distinguished Professor of Computational Chemistry, Department of Chemistry

Peyman Givi, Ph.D., James T. MacLeod Professor, Department of Mechanical Engineering and Materials Science

Paolo Zunino, Ph.D., Assistant Professor, Department of Mechanical Engineering and Materials Science

Dissertation Advisors: Albert C. To, Ph.D., Associate Professor, Department of Mechanical Engineering and Materials Science,

Kenneth D. Jordan, Ph.D., Richard King Mellon Professor and Distinguished Professor of Computational Chemistry, Department of Chemistry

ATOMISTIC SIMULATIONS AND COMPUTATIONS OF CLAY MINERALS AT GEOLOGIC CARBON SEQUESTRATION CONDITIONS

Meysam Makaremi, PhD

University of Pittsburgh, 2015

Classical atomistic simulations are carried out to study carbon sequestration at deep underground formations. In classical simulations, formulas and equations are inherently different from those used in continuum and quantum calculations. Here, in contrast to continuum approaches such as the finite element method, interactions of atomic particles are computed, and unlike quantum techniques such as the density functional theory, calculations are not restricted to a limited number of atoms, therefore a balance between accuracy and computational cost makes classical atomistic techniques the best candidate to study layered materials in numerous situations.

The success of CO_2 sequestration depends on diverse parameters related to the depth and type of the underground formations. In this work, chemical, physical, and geometrical characteristics of formations are investigated. Different types of interlayer cation (Na^+ and Ca^{2+}), intercalated molecule (water and CO_2), and clay structure (montmorillonite (MMT) and beidellite (BEI), and pyrophyllite (PPT)) are investigated as chemical parameters. Rotational degree of layers, pressure, temperature and chemical potential are considered as geometrical and physical variables.

Using free energy calculations, stable energy states due to the intercalation of water and carbon dioxide to smectite structures are predicted. For hydrated systems, three states consisting of interlayer spacing values 9-10, 11.5-12.5 and 14.5-15.5 Å, respectively called 0W, 1W and 2W hydration state are found. For systems including mixed H_2O-CO_2 intercalation, the amount of adsorbed CO_2 alters and reaches its peak at the sub-first hydration levels.

Another fascinating result emerges by simulating the binary MMT-CO_2 system. The global minimum is found at the dry (0W) state which explains why there is no experimental observation of pure CO_2 adsorption on the MMT surface. Finally, ternary smectite-H_2O-CO_2 simulations show that the amount of adsorbed CO_2 in the clay phase is higher than that of bulk phase suggesting that the underground formation is a proper option to store extensive volumes of the green house gas carbon dioxide.

TABLE OF CONTENTS

LIST OF TABLES

LIST OF FIGURES

PREFACE

This work wouldn't have been accomplished without help of many people. I am grateful to my advisor, Professor Kenneth Jordan, for his support and patience. Also, I would thank to my PhD committee members, Professor Peyman Givi, Professor Albert To and Professor Paolo Zunino, for their valuable comments and advice. My appreciation goes to my NETL collaborator, Dr. Evgeniy Myshakin, for his friendship and collaboration including our fruitful Saturday meetings.

I would thank to my colleagues and friends; Mahdi Mohebbi, Kamran Karimi, Ozan Karalti, Vamsee Voora, Keith Werling, Anshuman Thakur, Rozita Laghaei, Michael Deible, Xun Wang, Togo Odbadrakh, Kaye Archer, Reddy Samala, Kevin Gasperich and Abhijeet Das.

I dedicate this work to my dearest people, my parents, for their unconditional love, support, and for their valuable life lessons.

1.0 INTRODUCTION

1.1 MOTIVATION

Over the past few decades, rapid development of CPU's has revolutionized scientific computing and has introduced computer modeling as a robust method to probe the properties of complex materials at the atomic and subatomic scales. Atomistic simulations can be carried out by using two different techniques, classical molecular mechanics and quantum mechanical methods, each of which has unique advantages, one provides the computational efficiency by using relatively simple principles, while the other provides accuracy by including quantum effects. Classical molecular mechanics methods are based on Newtonian mechanics and consider atoms as the smallest particles interacting through classical force fields. Electronic structure (quantum mechanical) methods based on the Schrödinger equation explicitly deal with electrons and nuclei. The classical force field parameters can be determined from experimental measurements or quantum mechanics calculations. Systems with millions of atoms can be simulated by using classical force field methods, while one is generally limited to several hundred atoms with quantum mechanical methods, even when utilizing a large number of parallel processors[1, 2]. Since in this work, large systems need to be modeled, we will apply only the classical techniques to carry out the simulations.

Classical techniques can be divided into molecular dynamics (MD) and Monte Carlo (MC) methods. Molecular dynamics is deterministic and calculates the time evolution of a process by solving classical equations of motion, whereas Monte Carlo is a stochastic procedure, and explores the phase space by random sampling. Moreover, based on statistical mechanics, a classical or quantum ensemble is defined as a collection of systems under the same physical conditions, such as constant volume (V), temperature (T), pressure (P), num-

ber of atoms (N) and chemical potential (μ)[3], by which the realistic conditions of a process can be described. For instance, carbon sequestration requires constant chemical potential, pressure and temperature to reach the equilibrium state at the deep sedimentary formations, so the μPT ensemble is able to appropriately simulate this process.

In carbon sequestration supercritical CO_2 ($scCO_2$) is injected into underground sedimentary formations, such as saline aquifers, depleted oil, gas resources, or coal beds. These formations are deeper than 800 meters, where high pressures allow sha5028 filling property for a long time[4]. CO_2 storage mostly consists of three phases interacting with each other which include liquid water, $scCO_2$, and solid clay phases. The fluid phases (H_2O and CO_2) intercalate into the interlayer of the solid phase, and may cause swelling of the clay phase[5, 6, 7, 8, 9, 10, 11, 12, 13].

Swelling of clay minerals, a family of layered materials which swell in the presence of water and CO_2, has been the subject of several experimental and computational studies. Using in situ XRD measurements, Schaef *et al.*[14] reported that the intercalation of dry $scCO_2$ in Ca-exchanged montmorillonites (Ca-MMTs), a type of clay mineral, can lead to either expansion or shrinkage of the clay structure depending on the initial hydration state. Giesting *et al.*[15] employed XRD diffraction method for Na-exchanged montmorillonites (Na-MMTs) and found that the partially hydrated clay experiences expansion in the presence of CO_2 at both gaseous and supercritical phases, while the dehdrated clay is unaffected in both conditions. In a recent study, using XRD and IR spectroscopy, Loring *et al.*[16] investigated the intercalation process by applying variably wet $scCO_2$ (including H_2O concentrations from 0 to 16 mmol/g) and observed that Na-MMT strongly adsorbs CO_2 molecules at low water concentrations ($\sim$ 0-4 mmol/g). Botan *et al.*[17] applied grand canonical Monte Carlo (μVT-MC) simulations to investigate the role of CO_2 intercalation on the swelling process and reported that the hydrated Na-MMT is able to adsorb CO_2; however, no change happens to the dimensions of the clay structure upon the CO_2 adsorption. In previous work[18], molecular dynamics simulations carried out in the NPT ensemble showed that the CO_2 adsorption is drastically affected by the initial hydration conditions of the clay.

The expansion process is controlled by numerous parameters that can be divided into geometrical, physical, and chemical categories. Three main thermodynamics variables consist

of the surrounding temperature, pressure and chemical potential of the interacting components containing counterions, water and CO_2 molecules. Chemical aspects include the size of the interlayer cations, the location of isomorphic substitutions (happening in tetrahedral, octahedral sheets or both) and the magnitude of layer and interlayer charges[19, 20, 21, 22]. Furthermore, the multiplicity and arrangement of smectite layers can be mentioned as geometrical parameters. Multiplicity includes the type of different layers in a clay sample, *i.e.* they may contain only a single type, or they might be composed of dissimilar types such as illite/smectite, and beidellite/montmorillonite. Arrangement implies the configuration and placement of different clay layers with respect to each other, and they may not be exactly juxtaposed and can be shifted or rotated due to mechanical and thermal stresses[23].

In the first step of this work, the response of clay to rotational (turbostratic) disorder is investigated. Occurring due to the rotation of clay layers with respect to each other around the normal axis of the clay surface, the disorder has been frequently observed in natural samples[24, 25], while in the modeling of clay minerals, it is generally ignored with the assumption that similar layers are consequently stacked in the space to decrease the computational cost. However, it is compelling to model the rotated structures resembling natural lab samples to precisely investigate the clay behavior due to water and carbon dioxide intercalation.

In the next step, the clay adsorption and expansion behaviors are studied by performing multiphase Gibbs ensemble Monte Carlo (GEMC) simulations. In previous studies[26, 27, 28, 29, 18], mostly molecular dynamics simulations including NPT and NVT ensembles were carried out to evaluate the smectite behavior. These simulations involve a fixed number of components (N); while, the chemical potential (μ) of interacting phases is constant at the equilibrium point, and the number of interlayer species may fluctuate, therefor to study the clay adsorption behavior it is essential to employ methods containing a fixed μ allowing water and carbon dioxide to transfer between phases. In another study[17] by Botan *et al.*, the grand canonical Monte Carlo (μVT-MC) approach including the constant chemical potential was used to study the mixed H_2O-CO_2 intercalation, although they disregarded the structures including small basal distances (d-spacing $= 9.5 - 12$ Å) including significant energy minima therefore necessary to interpret the clay behavior at the dry and nearly dry

conditions. Moreover, chemical potential calculation in the μVT-MC method is burdensome, and it has to be determined precisely to obtain reliable outcomes.

As a summary, we try to find answer for the following questions in the first step.

- How can one model clay mineral layers including the turbostratic disorder?
- How do the energetic and structural properties of clay change with respect to the degree of rotation?
- How does the disorder effect on the distribution of interlayer species?
- How does the type of interlayer cations influence the response of MMT to the rotation?
- What components of the internal energy are significantly affected as a response the disorder?

And at the second step we answer the following questions.

- How can one apply the multi-component GEMC technique to simulate interacting phases at deep underground formations and cap rocks?
- What are the stable energy states of smectite with respect to pure H_2O and CO_2 intercalations?
- What is the swelling behavior under the influence of the mixed H_2O-CO_2 intercalation for an extensive range of interlayer spacing values ($9.5 - 17.5$ Å)?
- What is the role of isomorphic substitution on the clay expansion behavior?
- How does smectite surface adsorb water and carbon dioxide molecules?
- What values of interlayer spacing result in the maximal amounts of CO_2 adsorption?
- What is the effect of isomorphic substitution on the CO_2 adsorption and its behavior inside the intelayer space?
- Can underground smectite formations be proper options to store extensive amounts of carbon dioxide?

1.2 CLAY MINERALS

Smectites, also called clay minerals, are a family of layered clays which expand in the presence of water. As illustrated in Fig. 1, these materials consist of TOT (2:1) layers in which there are three sheets, two tetrahedral (T) sheets and one octahedral (O) sheet placed between the tetrahedral ones. In the smectite structure, each silicon atom is surrounded by four oxygen atoms, three of which, called basal oxygens, are linked together and form the tetrahedral sheet, while the last of which, called the apical oxygen, with hydroxyl groups together form the octahedral sheet. Another property of the clay mineral is to experience isomorphic substitutions, in tetrahedra, octahedra or both, by which Si^{4+} of the tetrahedral sheet is substituted by Al^{3+}, or octahedra Al^{3+} is replaced by Mg^{2+} or Fe^{2+}. The substitutions result in negative charges for the layer that are neutralized by interlayer cations such as Na^{+}, K^{+}, Li^{+}, Ca^{2+} and Mg^{2+}. In the octahedral sheet the main cation can be bivalent, *e.g.* Fe^{2+}, or trivalent, *e.g.* Al^{3+}, creating two groups of smectites, called trioctahedral and dioctahedral, respectively. In trioctahedral smectites, all of the octahedral sites are occupied, while in dioctahedral smectites, two-thirds of the sites are occupied.

Moreover, depending on the location of the hydroxyl groups with respect to the octahedral vacancy, there are two types of dioctahedral clays. If hydroxyl groups are placed on the opposite sides of the vacancy, the smectite is trans-vacant, otherwise, it is called cis-vacant. Pyrophyllite is a basic dioctaheral clay lacking substitutions, or intercalated cations, thus having a neutral structure. A counterpart of pyrophyllite is Montmorillonite (MMT) in which the main octahedral cation, Al^{3+}, is replaced by a divalent cation such as Mg^{2+}. If instead of the octahedral sheet, tetrahedral sheets suffer an isomorphic substitution, such as Si^{4+}/Al^{3+}, the clay is called beidellite (BEI). These clay minerals are named on the basis of their interlayer cation *e.g.* Na-MMT when the clay is montmorillonite and the counterion is sodium. In the rest of this study, we mainly focus on MMTs and BEIs which are major components of the underground formations, in addition we only consider the trans-vacant configuration of smectites in our calculations, because these kinds of minerals are more common in nature, and the previous simulations of this group and studies of other groups[30, 31] show similar computational results for both trans and cis-configurations[21, 32].

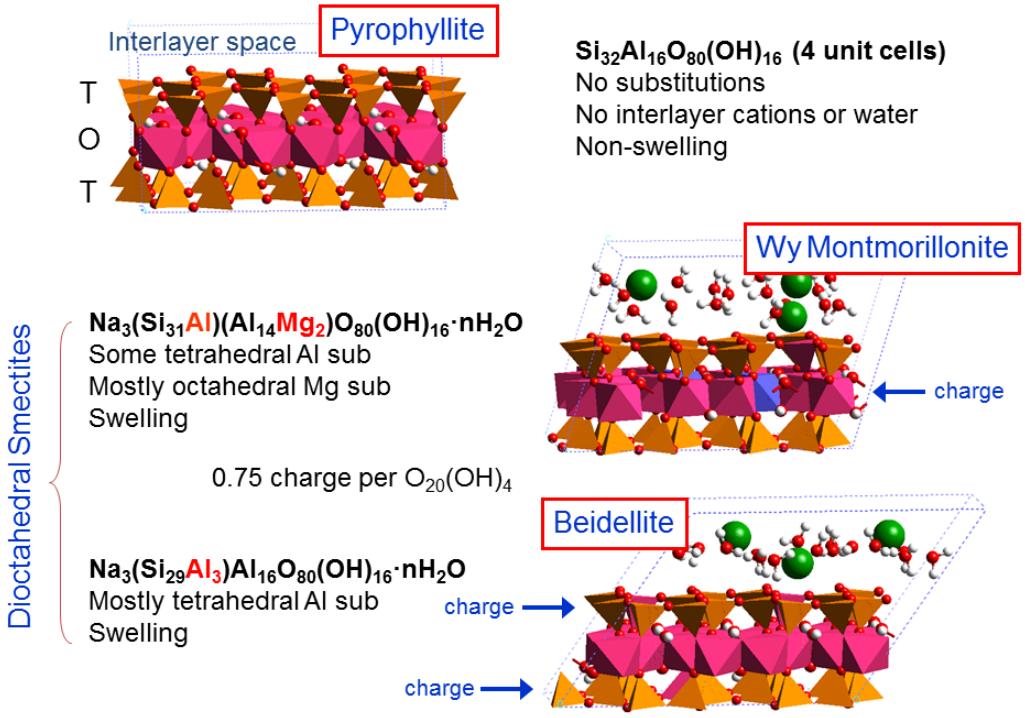

Figure 1: Structure of 2:1 (TOT) dioctahedral clays. Each layer consists of two tetrahedral sheets and one octahedral sheet. Color coding of atoms consists of orange, purple, blue, green, red and white for Si, Al, Mg, Na, O and H.

1.3 SWELLING MECHANISM

Swelling of smectite layers can be classified into two categories, crystal and osmotic swelling. Crystal (short-range) expansion happens when the interlayer spacing is $\sim$ 9-20 Å. All smectites can experience this process occurring in a step-wise fashion in 0W, 1W, and 2W hydration states with zero, one and two intercalated water layers in the interlayer space, accordingly[34, 35, 36, 37]. The hydration states are thermodynamically comparable to phases, and the transitions between states mirror phase transitions. The second category

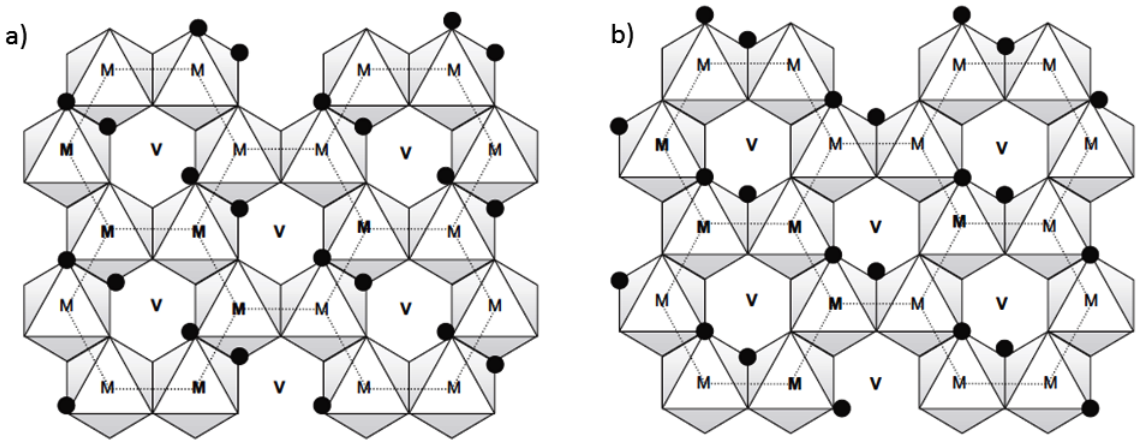

Figure 2: Trans-vacant (a) and cis-vacant (b) configurations of the octahedral sheet in dioctahedral smectites[33]. Solid black circles denote hydroxyl groups. V and M indicate vacancies and octahedral centers, respectively.

is the osmotic (long-range) swelling consisting of larger interlayer distances ($\sim$ 20-130 Å) and takes place only in the clay minerals containing intercalated cations such as Li^+ and Na^+ with high hydration tendency. Massive volumes of water are adsorbed into the clay as a result of the larger concentration of cations inside the interlayer space than that of the neighborhood region to equilibrize the concentration in both sides[38]. In this study, we only focus on the crystal swelling which is prevalent in smectites at the deep carbon dioxide storage conditions.

To have a better understanding of the crystal expansion, we can analyze the behavior of Na-MMT in the presence of water. At the beginning, suppose that the montmorillonite is in the dry state (0W), so Na^+ cations are fully adsorbed on the clay surface. In the presence of low amounts of water, the clay starts swelling due to the hydration tendency of interlayer counterions, and it expands to the first hydration state (1W) with a H_2O/Na^+ ratio $\sim$ 3-4, and a layer spacing $\sim$ 11.5-12.5 Å in which water molecules are placed in the center of the interlayer and make hydrogen bonds to basal oxygens of the MMT surface, while the cations still remain adsorbed to the clay surface. With adsorption of more water molecules, the clay

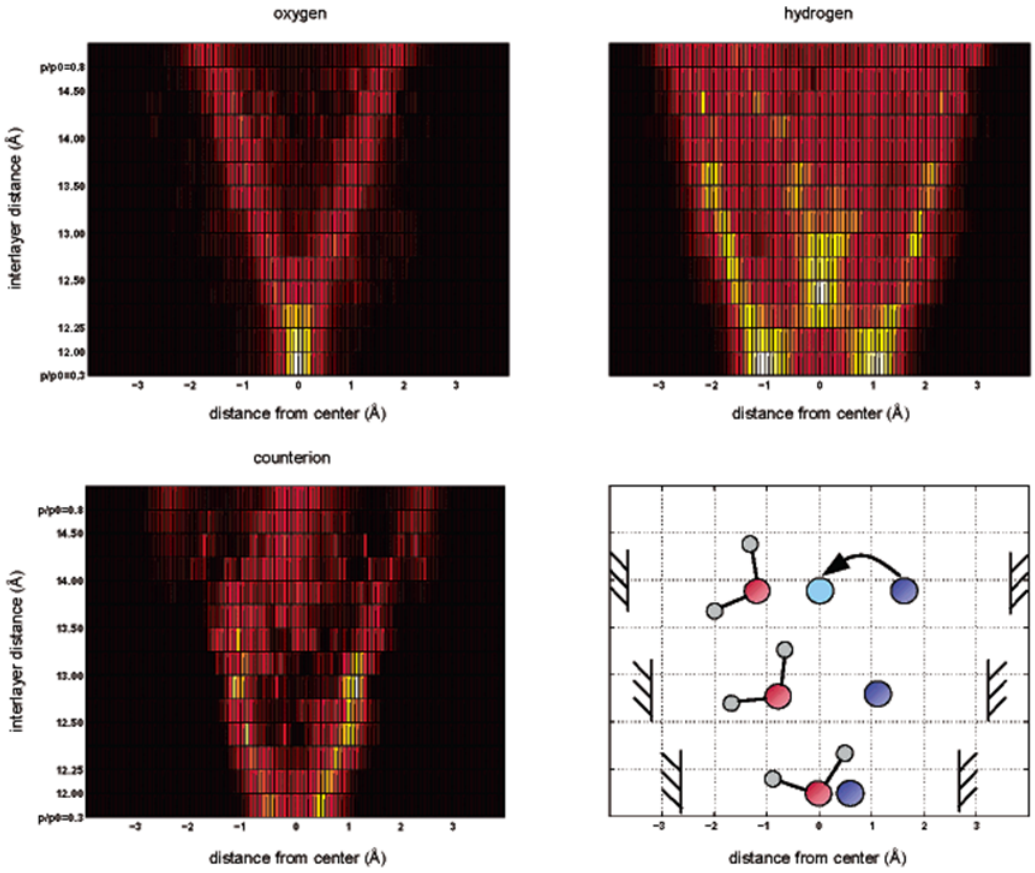

Figure 3: Distribution of interspace components; water oxygen (upper left), water hydrogen (upper right), and Na^+ (lower left) in the clay interspace during the 1W/2W swelling transition[22]. In the lower right picture, red, white and blue circles represent oxygen, hydrogen and Na, respectively.

expands to the second hydration state (2W), in which counterions move to the center of the interspace and are completely hydrated by water molecules leading to an interlayer distance $\sim$ 14.5-15.5 ($H_2O/Na^+ \sim$ 8-9). This process is depicted in Fig. 3[39, 22].

1.4 SWELLING THERMODYNAMICS

Diestler *et al.*[40] and Bordarier *et al.*[10] used the slit micropore model to explain the thermodynamics of the swelling process. The internal energy equation of a pore can be defined as

$$\begin{aligned} dU = & TdS + \mu dN + \sigma_{xx} s_y s_z ds_x + \sigma_{yy} s_z s_x ds_y \\ & + \sigma_{zz} s_x s_y ds_z + \tau_{zx} s_x s_y dl_x + \tau_{zy} s_x s_y dl_y. \end{aligned} \tag{1.1}$$

Where i and j are index notations. T, S, μ, N, σ_{ii}, τ_{ij}, respectively, represent the temperature, entropy, chemical potential, number of molecules, normal stress and shear stress. s_i and l_i are Cartesian components of the micropore represented in Fig. 4.

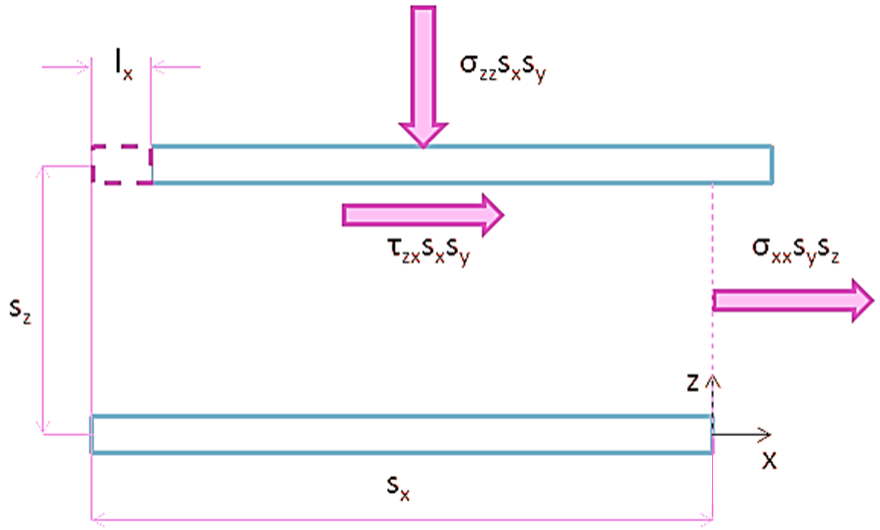

Figure 4: Slit micropore structure including position and force components.

Moreover, the free energy and isostress free energy are, respectively, defined as

$$F = U - TS - \mu N, \tag{1.2}$$

$$\Phi = F - \sigma_{zz} A\, s_z, \tag{1.3}$$

where A is the surface area of the clay. The difference in the swelling free energy for the wall separation Δs_z can be written as

$$\Delta\Phi = \Delta F - \sigma_{zz} A \, \Delta s_z, \tag{1.4}$$

by using equations (1.1) and (1.4), and fixing dimensions in all directions except the z direction. Considering the fact that μ and T are constant at the phase equilibrium,

$$\Delta\Phi = A \int_{s_z^0}^{s_z} (\sigma_{zz}(s'_z) - \sigma'_{zz}) ds'_z, \tag{1.5}$$

where σ'_{zz} is the applied constant stress. By eliminating the isotropic part of the stress tensor (bulk pressure) from the stress terms, the equation can be rewritten as a pressure based equation

$$\Delta\Phi = -A \int_{s_z^0}^{s_z} (P_{zz}(s'_z) - P'_{zz}) ds'_z, \tag{1.6}$$

in this equation $P_{zz}(s'_z)$ and P'_{zz} are the clay normal (disjoining) and applied pressure, respectively. Therefore by the calculation and integration of the clay phase pressure, the clay expansion and contraction behavior can be investigated.

In addition, Smith[41] suggested another method to study the phenomenon from average potential energies of the hydrated clay. He claimed that the global energy minimum corresponds to the minimum of the immersion energy (Q),

$$Q = \langle U(N) \rangle - \langle U(N^0) \rangle - (N - N^0) U_b, \tag{1.7}$$

in this equation, $\langle U(N) \rangle$ and $\langle U(N^0) \rangle$ are, respectively, the average clay energy with N adsorbed molecules, and the average reference energy with N^0 adsorbed molecules; and U_b is the bulk phase energy of adsorbed molecules.

1.5 OVERVIEW AND SCOPE

The objective of this work is to use molecular mechanics methods to study the effect of H_2O and CO_2 intercalation on the swelling behavior of smectites, in particular montmorillonite and beidellite. Two techniques, classical Monte Carlo and classical molecular dynamics, are employed to achieve this objective. The former is a successful candidate in the calculation of structural factors of clay minerals, while the latter evaluates the dynamic properties of the system.

In chapter 2, classical computational methods are described. The governing relations and ensembles are briefly discussed, and finally the classical force fields used to study smectites, water and carbon dioxide are introduced.

In chapter 3, by performing classical NPT-MD and NVT-MD simulations, energetic and structural properties of turbostratic MMT structures including consecutive rotated layers are analyzed. Two different approaches, the position constraining and enforced rotation, are utilized to spell out the role of rotation; the first approach is proper for rotated layers stemming from geological formations, and the second one is qualified for layers under short-term torsion stresses attributed to the supercritical CO_2 injection. The result suggests that turbostratic formation leads to different effects on dry and intercalated MMT structures: in one it has a stabilizing effect, while in the second it is energetically unfavorable. Moreover, the effect of the disorder on the distribution of interlayer components is studied for different structures including different amount of H_2O and CO_2, and it is found that the distribution is impacted by the Moiré pattern[23] stemming from the rotation of clay surfaces.

In chapter 4, the application of multiphase Gibbs ensemble Monte Carlo (GEMC) with constant number of molecules, pressure and temperature (NPT-GEMC) to specify clay adsorption and expansion behavior is described. For the first time we use the GEMC technique to calculate the equilibrium properties of Na-MMT and Na-BEI at fixed temperature, pressure and chemical potential for a full range of basal d-spacing values ($9.5 - 17.5$ Å) and for different forms of molecular intercalation consisting of the pure intercalation including only two components, solid-fluid (MMT-H_2O or MMT-CO_2), and the mixed intercalation containing three components solid-fluid-fluid, (MMT-H_2O-CO_2). Since CO_2 has two differ-

ent physical phases at T = 348.15 K (gaseous at lower pressures, and supercritical fluid at higher pressures) simulations are carried out at two P-T conditions with pressures 25 and 125 bar, and the same temperature 348.15 K. Normal clay pressure and swelling free energy are calculated to evaluate the clay stable states, and next the transport properties of interlayer species at stable states are investigated by performing NVT-MD simulations.

In chapter 5, the results of this work are summarized, and the ongoing-future studies are introduced.

2.0 CLASSICAL MODELING OF CLAY MINERALS

2.1 OVERVIEW AND PERSPECTIVE

Classical molecular dynamics (MD) and Monte Carlo (MC) approaches are employed extensively to simulate nanoscale processes and phenomena in computational science and engineering fields. The first approach assigns initial velocities to particles and solves the equations of motion to deterministically calculate atomic trajectories and to probe the energy surface of the system, while the second method evolves trajectories in the phase space by random motions discovering the configurations with minimal internal energies. Each method offers different advantages and abilities, and has to be chosen with respect to the system under study and the desired properties. Monte Carlo simulations are carried out to compute physical variables of the system by averaging over all accepted configurations, so they are generally fast. Molecular dynamics calculations provide the time-dependent evolution of the system presenting the ability to compute dynamic properties such as atomic diffusion which can be compared with experimental NMR and FTIR data. Furthermore, broadly speaking "as an unwritten rule", in the modeling of layered materials, MD systems consist of flexible layers and variable interlayer distances, while Monte Carlo systems involve rigid sheets and constant interlayer spacing values to increase the computational efficiency[2].

In section 2.2, basic principles and relations of molecular dynamics are introduced. The Monte Carlo approach and its different ensembles, such as Gibbs ensemble Monte Carlo, are the topics of section 2.3. In section 2.4, classical force fields used for CO_2, water and minerals of this study are reviewed.

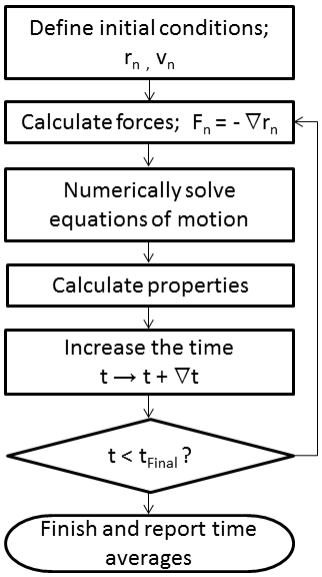

Figure 5: Molecular dynamics algorithm.

2.2 MOLECULAR DYNAMICS METHOD

In a nutshell, molecular dynamics solves physical equations of motion to predict the movement of particles in the phase space. At the start point, initial conditions such as initial positions and velocities are defined, and by applying classical potential functions (force-fields) atomic and molecular forces are determined in next step (the most computationally expensive part). Then, by using Newton's laws of motion and considering a time-step, the new configuration of the system is identified. The last two steps are iteratively repeated until the final time condition is met, and finally time averages of thermodynamic quantities are reported. A simplified flowchart of a MD program is illustrated in Figure 5.

2.2.1 Equations of Motion

The Lagrangian function ($L(\vec{q}, \dot{\vec{q}})$) is defined as,

$$L = K - U, \tag{2.1}$$

$\vec{q}$, $\dot{\vec{q}}$ are the generalized position vector and its time derivative. K and U are the kinetic and potential energy, respectively, and the equation of motion[42] can be written

$$\frac{d}{dt}(\partial L/\partial \dot{q}_i) - \partial L/\partial q_i = 0, \tag{2.2}$$

here, t is the time and i represents the spacial coordinate. By replacing common kinetic and potential energy formulas in this equation, the force on atom n can be extracted as

$$\vec{f_n} = \vec{\nabla}_{r_n} L = -\vec{\nabla}_{r_n} U, \tag{2.3}$$

in which $\vec{r}$ is the atomic coordination vector. If the generalized momentum is defined as $p_i = \partial L/\partial \dot{q}_i$, equation (2.1) converts to

$$\dot{p_i} = \partial L/\partial q_i. \tag{2.4}$$

The relation between the Lagrangian and Hamiltonian is defined as

$$H(\vec{p}, \vec{q}) = \sum_i \dot{q}_i p_i - L(\vec{q}, \dot{\vec{q}}), \tag{2.5}$$

and the Hamilton's equations can be written

$$\begin{aligned} \dot{p_i} &= -\partial H/\partial q_i, \\ \dot{q_i} &= \partial H/\partial p_i, \end{aligned} \tag{2.6}$$

or in Cartesian coordinates, they become

$$\begin{aligned} \dot{\vec{p}}_n = \vec{f_n} &= -\vec{\nabla}_{r_n} U, \\ \dot{\vec{r}}_n &= \vec{p}_n/m_n, \end{aligned} \tag{2.7}$$

where m is the atomic mass. Also, we can extract

$$\vec{f_n} = m_n \ddot{\vec{r}}_n. \tag{2.8}$$

By solving differential equations (2.7) and (2.8), one can simulate the kinematic of atoms in a thermodynamic system[3].

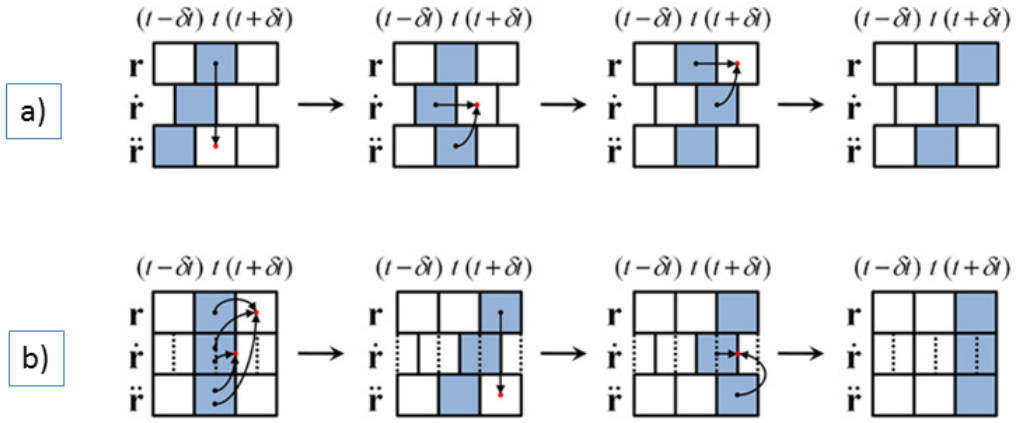

Figure 6: Finite difference schemes used in MD simulations[3]. a) The leap-frog algorithm. b)The velocity Verlet algorithm.

2.2.2 Finite Difference Method

Finite difference methods (FDM) numerically solve differential equations, therefore these methods are implemented in the MD algorithm to generate atomic trajectories in the phase space by solving ordinary differential equations (2.7) and (2.8). Two FDM's, widely used for MD simulations, are chosen for this study. The first one is the leap-frog algorithm[43] which can be written as

$$\begin{aligned} r(t+\delta t) &= r(t) + \delta t\, v(t+\delta t/2), \\ v(t+\delta t/2) &= v(t-\delta t/2) + \delta t\, a(t), \\ v(t) &= \frac{1}{2}[v(t+\delta t/2) + v(t-\delta t/2)], \end{aligned} \tag{2.9}$$

r, v, a, t and δt are, respectively, the position, velocity, acceleration, time and time increment. The second method, called the velocity Verlet scheme[3], can be described as

$$
\begin{aligned}
r(t+\delta t) &= r(t) + \delta t\, v(t) + \frac{1}{2}\delta t^2\, a(t), \\
v(t+\delta t/2) &= v(t) + \frac{1}{2}\delta t\, a(t), \\
v(t+\delta t) &= v(t+\delta t/2) + \frac{1}{2}\delta t\, a(t+\delta t)],
\end{aligned}
\tag{2.10}
$$

these two algorithms are illustrated in Figure 6.

2.2.3 Physical Quantities

In molecular dynamics, physical quantities are calculated by averaging over the total number of particles in the system; for instance, the temperature is computed by taking the average of atomic velocities,

$$
< T >= \frac{1}{3(N-1)k_B} < \sum_n m_n \vec{v}_n \,.\, \vec{v}_n >, \tag{2.11}
$$

$\vec{v}_n$ is the velocity on atom n, k_B is the Boltzmann constant, and N is the total number of atoms. The pressure is computed as,

$$
< P >= \frac{N k_B < T >}{V} + \frac{1}{3V} < \sum_{n_1} \sum_{n_2} \vec{F}_{n_1 n_2} \,.\, \vec{r}_{n_1 n_2} >, \tag{2.12}
$$

where V is the total volume of the system, $\vec{F}_{n_1 n_2}$ and $\vec{r}_{n_1 n_2}$ are the atomic force and distance between atoms n_1 and n_2.

MD simulations can be performed in various ensembles in which different physical variables such as the number of atoms (N), volume (V), temperature (T), pressure (P), and chemical potential (μ) are kept fixed or constrained. For this study, all MD simulations are carried out in NVT or NPT ensembles. The NVT ensemble includes the fixed number of particles and volume, and the temperature is constrained by a thermostat; such as Andersen[44], Berendsen[45] and Nosé-Hoover[46] thermostats. In the NPT ensemble, besides the temperature, the pressure is also constrained by employing a barostat, while the number of atoms is constant. Andersen[44], ParrinelloRahman[47], Berendsen[45] and Nosé-Hoover[46] can be mentioned as popular barostats.

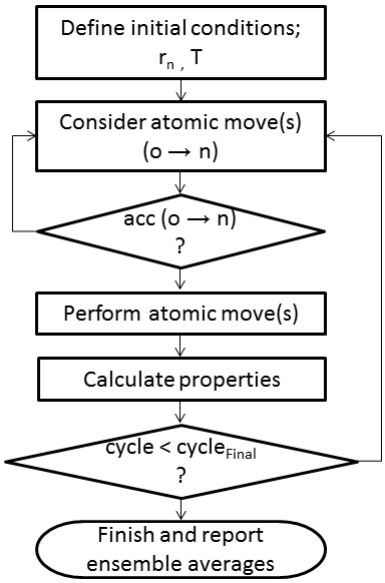

Figure 7: Monte Carlo algorithm.

2.3 MONTE CARLO METHOD

This method stands on stochastic sampling. Assume that, initially, a system is in state o. By choosing a random move the possibility of the system's evolution to state n is surveyed through the evaluation of energy surface, therefore if the new configuration is more stable than the older one, the movement will be accepted. Otherwise, the move might be rejected or accepted depending on a random number selection, and if the move is rejected the system will remain in state o. The process is repeated in a loop to probe all of the possible energy minima of the system.

2.3.1 Metropolis Monte Carlo

The heart of Monte Carlo is random sampling, but it must be efficient and acute, especially when we deal with systems including atomic interactions which may consist of an incalculable number of states, seldom of which involve low energy. To resolve this issue, Metropolis

et al.[48] suggested to use importance sampling which considers only a limited number of random states according to their state probabilities. The state probability (ρ) means the probability that a system is in a certain state and is related to the ensemble of the system, e.g for NVT system the state probability can be defined as

$$\rho(\vec{r}) = \frac{\exp(-\beta U(\vec{r})}{\int d\vec{r} \exp(-\beta U(\vec{r})}, \tag{2.13}$$

here, $\beta = (k_B T)^{-1}$, in which k_B and T are the Boltzmann constant and temperature, respectively. This sampling procedure imposes a chain of states called a Markov chain which contains two properties: first, the number of possible states is finite, and second, every new state is only related to its preceding one[3].

The Monte Carlo detailed balance condition describes that for an infinitely long simulation,

$$\rho(\vec{r_o})\pi(o \to n) = \rho(\vec{r_n})\pi(n \to o), \tag{2.14}$$

in which o and n defines old and new states, $\pi(o \to n)$ and $\pi(n \to o)$ are probabilities of moving from the old state to the new one and vice versa, and π can be expressed as

$$\pi(o \to n) = \alpha(o \to n)\, acc(o \to n), \tag{2.15}$$

where, α and acc are the probabilities of selection and acceptance of a move, accordingly. One can assume $\alpha(o \to n)$ is equal to $\alpha(n \to o)$ due to microscopic reversibility, so the detailed balanced relation can be described as

$$acc(o \to n) = \exp[-\beta(U(n) - U(o))]\, acc(n \to o). \tag{2.16}$$

As a result, the acceptance conditions can be defined

$$acc(o \to n) = min\{1,\, \exp[-\beta(U(n) - U(o))]\}. \tag{2.17}$$

A Metropolis Monte Carlo schematic is shown in Figure 7.

2.3.2 Monte Carlo Ensembles

Each MC system depending on its ensemble needs a sort of random moves to evolve in the phase space. For instance, to simulate a NPT system, one needs to consider particle transfer and volume adjustment moves to insure that the temperature and pressure are in equilibration, while the number of particles is fixed. Some popular Monte Carlo ensembles are introduced as follows:

1. **Canonical Ensemble (NVT)**

   The number of atoms N and the volume V of the system are constant in this ensemble, therefore the system only needs atomic transfer moves to gain thermal equilibrium,

$$acc(o \to n) = min\{1, exp[-\beta(U(n) - U(o))]\}. \tag{2.18}$$

2. **Isobaric-Isothermal Ensemble (NPT)**

   This system includes two types of movement, the particle transfer and volume change, to equiliberate the temperature (T) and pressure (P). The transfer attempt is similar to that of the previous ensemble, whereas the volume adjustment move can be described as

$$\begin{aligned} acc(o \to n) = min\{1, exp[-\beta(U(n) - U(o) + P(V(n) - V(o)) \\ -N\beta^{-1}\ln(V(n)/V(o)))]\}, \end{aligned} \tag{2.19}$$

   where, $V(n)$ and $V(o)$ contain the energies of the new and old configuration, accordingly.

3. **Grand-Canonical Ensemble (μVT)**

   Grand-canonical ensemble encapsulates constant chemical potential (μ), volume (V) and temprature (T), and it consists of two different moves involving internal and external particle transfers, accordingly for the thermal and chemical equilibration at a fixed volume. Again the acceptance condition for the first move is similar to equation (2.16), but external transfers can be classified into two categories: particle insertion and particle deletion attempts; respectively, as follows:

$$acc(N \to N+1) = min\{1, \frac{V}{\Lambda^3(N+1)} exp[-\beta(U(N+1) - U(N) - \mu)]\}, \tag{2.20}$$

$$acc(N \to N-1) = min\{1, \frac{N\Lambda^3}{V} exp[-\beta(U(N-1) - U(N) + \mu)]\}, \tag{2.21}$$

here, Λ is the thermal de Broglie wavelength.

4. **The Gibbs Ensemble**

A system of interacting particles necessitates constant chemical potential, pressure and temperature at the equilibrium point. To have a well-defined ensemble, atleast one of the variables needs to be extensive, and since all of the three quantities are intensive, a μPT ensemble is not imaginable. To solve this issue, one might consider a large NPT system where different phases coexist and lead to the chemical equilibrium inside the box. Although, in theory this solution is possible, when there are several interacting phases in a single box, we need to consider an extensively large system, because, typically, there are mountainous energy barriers between phases due to phase interfaces consisting of substantial number of particles. As a result this, solution can be inefficient and costly, especially for the systems containing more than two coexisting phases[49].

The Gibbs ensemble Monte Carlo (GEMC)[50, 51] was suggested to remedy this difficulty. This method considers several boxes (one per each phase) directly interacting without any interface through three sorts of movement: intra-box transfer, inter-box displacement and volume adjustment. The intra-box transfer requires the acceptance condition (2.16), whereas, inter-box exchange moves are defined as,

$$\begin{aligned} acc(N_1, N_2 \to N_1 + 1, N_2 - 1) &= min\{1, \frac{N_1 V_2}{(N_2+1)V_1} exp[-\beta(U(n) - U(o))]\}, \\ acc(N_1, N_2 \to N_1 - 1, N_2 + 1) &= min\{1, \frac{N_2 V_1}{(N_1+1)V_2} exp[-\beta(U(n) - U(o))]\}, \end{aligned} \tag{2.22}$$

here, the first condition checks the possibility of an atomic transfer from box 1 to box 2, while the second relation investigates the possibility of the opposite move from box 2 to box 1. The volume move can be written as

$$acc(o \to n) = min\{1, \frac{V_1(n)}{V_1(o)}^{N_1} \frac{V_2(n)}{V_2(o)}^{N_2} exp[-\beta(U(n) - U(o))]\}, \tag{2.23}$$

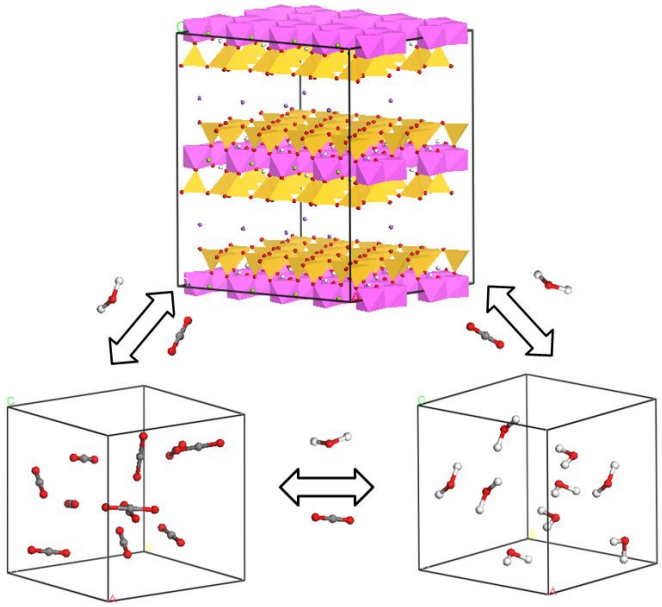

Figure 8: A schematic of a multiphase Gibbs ensemble monte carlo simulation including three different boxes (phases).

Moreover, GEMC simulations can be carried out in the canonical Gibbs ensemble (NVT-GEMC); involving a fixed number of molecules, volume and temperature; or in the isobaric-isothermal Gibbs ensemble (NPT-GEMC); with a constant number of molecules, pressure and temperature. To evaluate the phase transition of a pure substance; *e.g.* water vapor-liquid phase transition; the NPT-GEMC method is not applicable because the phase transition happens in a 1-D line in the two dimensional P-T phase diagram. As a consequence, both of the intensive variables, pressure and temperature, can not be predetermined, so NVT-GEMC approach is employed at a fixed temperature, and the other variable, the pressure, is evaluated by fixing its conjugate extensive variable, volume[49]. To study the equilibrium conditions of a multiple-substance system, such as the ternary smectite-H_2O-CO_2 system at carbon sequestration P-T conditions, NPT-GEMC is chosen to provide thermal, mechanical and chemical equilibration for the system.

2.4 POTENTIAL FUNCTION

Force-fields (potential functions) consist of atomic interaction parameters and formula, and generally divided into two terms, nonbonded and bonded energies. The nonbonded (noncovalent) part includes pairwise energy components such as electrostatic and Lennard-Jones (called L-J and containing attractive dispersion (van der Waals) and repulsive terms); while, bonded (covalent) part involves covalent energy terms like bond stretching, angle bending and dihedral energies.

To carry out exact classical simulations, considering accurate force-fields is vitally important, therefore we select Clayff[52] force-field developed in Sandia National Laboratory, which is widely used to study clay minerals. This force-field has the following equation

$$E_{total} = E_{Coul} + E_{L-J} + E_{stretch} + E_{bend}, \tag{2.24}$$

in which, E_{Coul}, E_{L-J}, $E_{stretch}$ and E_{bend} are electrostatic (Coulombic), L-J, bond stretching and angle bending energy terms and they can be described as

$$\begin{aligned} E_{\text{Coul}} &= \frac{q_i q_j}{4\pi\epsilon_0 r_{ij}}, \\ E_{\text{L-J}} &= 4\epsilon_{ij}[(\frac{\sigma_{ij}}{r_{ij}})^{12} - (\frac{\sigma_{ij}}{r_{ij}})^{6}], \\ E_{Stretch} &= \frac{1}{2}k_s(r_{ij} - r_0)^2, \\ E_{Bend} &= \frac{1}{2}k_b(\theta_{ijk} - \theta_0)^2. \end{aligned} \tag{2.25}$$

where, q is the atomic charge, e is the elementary charge of an electron, ϵ_0 is the vacuum permittivity, and ϵ_{ij} and σ_{ij} are the Lennard-Jones energy and distance parameters, respectively. r_{ij} and r_0 denote the distance between atoms i and j, and the reference distance, while θ_{ijk} and θ_0 define the angle between vectors r_{ij} and r_{jk}, and the reference angle. Also, k_s and k_b are the bond stretching and angle bending stiffness constants, accordingly. The bonded and nonbonded parameters of this force-field are depicted in table 1, 2 and 3. In addition pairwise parameters for dissimilar atoms are calculated from the Lorentz-Berthelot mixing rules[3]

$$\sigma_{ij} = \frac{1}{2}(\sigma_i + \sigma_j), \quad \epsilon_{ij} = \sqrt{\epsilon_i \epsilon_j}. \tag{2.26}$$

Table 1: Clayff Force-field[52] Nonbonded Potential Parameters.

atom type	symbol	charge [e]	ϵ [kcal/mol]	σ [Å]
water hydrogen	h*	0.4100		
hydroxyl hydrogen	ho	0.4250		
water oxygen	o*	-0.8200	0.1554	3.5532
hydroxyl oxygen	oh	-0.9500	0.1554	3.5532
bridging oxygen	ob	-1.0500	0.1554	3.5532
bridging oxygen with oct. substitution	obos	-1.1808	0.1554	3.5532
bridging oxygen with tet. substitution	obts	-1.1688	0.1554	3.5532
bridging oxygen with double substitution	obss	-1.2996	0.1554	3.5532
hydroxyl oxygen with substitution	ohs	-1.0808	0.1554	3.5532
tetrahedral silicon	st	2.1000	1.8405×10^{-6}	3.7064
octahedral aluminum	ao	1.5750	1.3298×10^{-6}	4.7943
tetrahedral aluminum	at	1.5750	1.8405×10^{-6}	3.7064
octahedral magnesium	mgo	1.3600	9.0298×10^{-7}	5.9090
hydroxide magnesium	mgh	1.0500	9.0298×10^{-7}	5.9090
octahedral calcium	cao	1.3600	5.0298×10^{-6}	6.2484
hydroxide calcium	cah	1.0500	5.0298×10^{-6}	6.2428
octahedral iron	feo	1.5750	9.0298×10^{-6}	5.5070
octahedral lithium	lio	0.5250	9.0298×10^{-6}	4.7257
aqueous sodium ion	Na	1.0	0.1301	2.6378
aqueous potassium ion	K	1.0	0.1000	3.7423
aqueous cesium ion	Cs	1.0	0.1000	4.3002
aqueous calcium ion	Ca	2.0	0.1000	3.2237
aqueous barium ion	Ba	2.0	0.0470	4.2840
aqueous chloride ion	Cl	-1.0	0.1001	4.9388

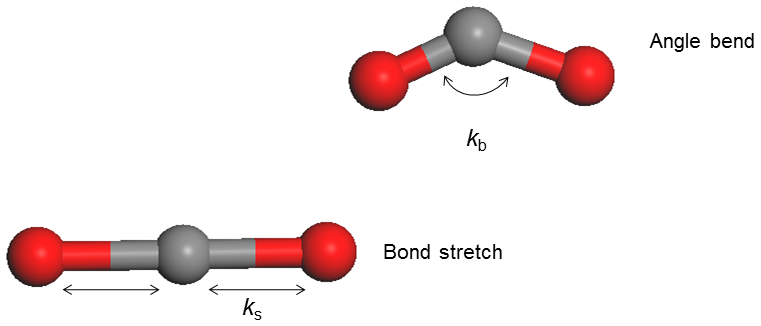

Figure 9: Bond stretching and angle bending configurations.

To deal with CO_2 interactions, a model[53] recently developed by the Sandia Lab group is applied, and the SPC model[54] is considered for water molecules.

Table 2: Clayff Force-field[52] Bond Stretching Potential Parameters.

atom i	atom j	k_s [kcal/mol Å^2]	r_0 [Å]
o*	h*	554.1349	1.0000
oh	ho	554.1349	1.0000
ohs	ho	554.1349	1.0000

Table 3: Clayff Force-field[52] Angle Bend Potential Parameters.

atom i	atom j	atom k	k_b [kcal/mol rad^2]	θ_0 [deg]
h*	o*	h*	45.7696	109.47
Metal	oh	ho	30.0	109.47
Metal	ohs	ho	30.0	109.47

3.0 RESPONSE OF DRY AND HYDRATED MONTMORILLONITES TO TURBOSTRATIC DISORDERING

3.1 INTRODUCTION

Carbon capture and storage technologies offer an important option for reducing CO_2 emissions and mitigating global climate change[55]. The technology of geologic CO_2 storage involves injection of supercritical CO_2 ($scCO_2$) into deep geologic formations overlain by sealing rocks that prevent buoyant CO_2 from migrating upward and out of the storage reservoir. The ability of cap rocks to retain injected CO_2 depends on their ability to maintain low permeability[56]. Cap rocks are often composed of shale or mudstone enriched with swelling clay minerals that may expand or contract upon interaction with $scCO_2$ that, in turn, could impact seal permeability, CO_2 mobility, or both[57, 58, 14]. Intercalation of CO_2 into the interlayer of swelling clay can cause geomechanical stress and affect the integrity of cap rocks and the ability of geological formations to contain stored CO_2[14, 59, 60]. The integrity of the cap rock is important because CO_2, being more buoyant than saline water and oil, will tend to migrate above these relatively immiscible fluids. Moreover, swelling clay minerals may also provide sites for sorption of CO_2[14, 61, 62, 63, 15] or environments for its transformation into carbonates[64].

Swelling clay minerals generally fall into the smectite group, which consists of a group of layered aluminosilicate mineral species with a wide range in compositional variability. We have focused our study specifically on montmorillonite (MMT), for which the central dioctahedral sheet is composed of octahedrally coordinated aluminum (Al) atoms and the adjacent sheets contain tetrahedrally coordinated silicon (Si) atoms. These sheets comprise a 2:1 or tetrahedral_octahedral_tetrahedral (TOT) layer. In MMT, the TOT layers are neg-

atively charged due to substitution of divalent metals (*e.g.*, Mg^{2+} for Al^{3+} in the octahedral sites). The negative charge of the TOT layers is counterbalanced by interlayer cations (*e.g.*, Na^{+}, K^{+}, Ca^{2+}, etc.) that can exhibit a variety of hydration states, causing expansion or contraction of the interlayer distance of the clay, depending on the relative humidity[65]

Recent X-ray diffraction (XRD), excess sorption, and neutron diffraction studies showed that the spacing between the mineral layers (basal d-spacing) of Na-rich-MMT expands upon interaction with gaseous CO_2 and $scCO_2$ and that the degree of expansion depends on the initial water content in the interlayers[60, 15, 13]. Those measurements indicated that the largest expansion is accompanied by an increase in the basal d-spacing from 11.3 to 12.3 Å, the number corresponding to a stable monolayer (the 1W hydration state characterized with basal d-spacings in the range of 11.5-12.5 Å; upon incorporation of more water, the d-spacing increases to 14.5-15.5 Å to the stable 2W hydration state where water forms a bilayer structure)[65, 11]. Interaction of anhydrous $scCO_2$ with smectite clay in the 2W and higher hydration states may lead to a collapse of the d-spacing to that of the 1W state[58, 14]. However, interaction of Na-exchanged Wyoming montmorillonite (SWy)and Ca-exchanged Texas montmorillonite (STx) samples with variably wet $scCO_2$ (2-100 % saturation of H_2O) induces swelling even to the values equal to the 3W state with a d-spacing of 18.8 Å[58, 14]. Thus, dry $scCO_2$ injected in a target reservoir has the capacity to dehydrate clay and to promote fracturing of cap rocks. On the other hand, after CO_2 becomes saturated by brine, it can induce further swelling of clay. Loring *et al.*[63] confirmed intercalation of CO_2 by means of NMR spectroscopy and attenuated total reflection infrared spectroscopy. Using diffuse-reflectance infrared spectroscopy, Romanov[61] reported a red shift of the characteristic fundamental frequency of CO_2 trapped in SWy and STx samples. The source of that shift was attributed to interaction of the intercalated CO_2 molecules with dipoles of water molecules[18].

Botan *et al.*[17] carried out Monte Carlo (MC) and molecular dynamics (MD) simulations of CO_2 intercalation into Na-MMT using a force field for clay from Smith[41] and the SPC[54] and EPM2[66] models for water and carbon dioxide, respectively. In line with experimental data[58, 14, 60, 15, 13], their simulations showed that hydrated clay intercalates CO_2 and that the thermodynamically stable structures are characterized with basal

d-spacings corresponding to the 1W and 2W hydration states. Other modeling studies using different force fields also point out that CO_2 molecules can exist in the interlayers of clay minerals[67, 68, 69, 70]. Krishnan *et al.*[70] recently reported information on the molecular-scale structure and dynamics of interlayer species in MMT-CO_2 systems. An excellent review of the recent advances in molecular modeling of CO_2-brine-mineral interactions is given in ref [71].

Another major feature of swelling clay minerals is related to rotational disorder inherently present in natural samples and manifesting itself through turbostratically stacked clay layers[23, 24, 25, 72]. Turbostratic disorder, a disorder in which different layers have different rotations with respect to an axis, is commonly found in naturally occurring samples of montmorillonite[25, 72]. To reconcile apparent discrepancies between high resolution transmission electron microscopy (HRTEM) images and powder X-ray diffraction (XRD)[73, 74], Guthrie and Reynolds[18] offered a model in which adjacent TOT layers of smectite are turbostratically stacked within $\sim 2-10^{\circ}$ rotation of each other[73, 74, 75, 76]. In this model, rotation of adjacent TOT layers results in breaking of coherency between the ditrigonal rings in the silica sheets on either side of the interlayer, thereby changing the framework structure that bounds the interlayer region. Instead of having a coherent alignment of ditrigonal rings on either side of the interlayer region, rotational disorder results in a Moiré pattern with a periodic variation in alignment of ditrigonal rings across the interlayer. In the simulations, smectite models are assumed to be perfectly oriented, and any impacts of rotational disorder are generally ignored. However, understanding interactions between interlayer species and rotationally disordered clay systems is mandatory to properly predict the behavior of geological formations and cap rocks under carbon dioxide invasion.

In the present study, classical MD simulations are used to investigate rotational disordering in MMT at various water and carbon dioxide contents. The simulations were carried out at P-T conditions relevant to geological formations for CO_2 storage. The main focus of the study is placed on comparison of energetic and structural changes associated with deviation of the clay layers from their ideally stacked positions. In addition, one-dimensional density profiles and two-dimensional density maps are engaged to study the distributions of interlayer species as a function of the rotational angle between adjacent TOT layers.

3.2 COMPUTIONAL DETAILS

3.2.1 Classical Force Field Simulations

The force field calculations were carried out using the GROMACS package[77]. For the clay system, the Clayff force field[52] that consists of nonbonded (electrostatic and van der Waals) terms parametrized for use with layered minerals was employed. For atoms i and j separated by a distance r_{ij}, the pairwise energy is given by

$$E_{ij} = \frac{q_i q_j e^2}{4\pi\epsilon_0 r_{ij}} + 4\epsilon_{ij}[(\frac{\sigma_{ij}}{r_{ij}})^{12} - (\frac{\sigma_{ij}}{r_{ij}})^6] \tag{3.1}$$

where q_i is the charge on atom i, ϵ_0 is the vacuum permittivity, and ϵ_{ij} and σ_{ij} are the Lennard-Jones (LJ) energy and distance parameters, respectively. The flexible SPC[54] model was used for the water molecules placed in the interlayer space and for the layer hydroxyl groups. For CO_2, a recently developed flexible potential[53] including intramolecular bond stretch and angle bend was used. The general expression for the total potential energy is

$$E_{total} = E_{Coul} + E_{Vdw} + E_{stretch} + E_{bend} \tag{3.2}$$

where harmonic potentials are used for the bond stretching and angle bending terms.

The LorentzBerthelot mixing rule[3] was used to obtain the LJ parameters for interactions between unlike atoms. It is worth mentioning that in an earlier paper[18] we showed that the description of CO_2 in liquid water using the force fields described above closely reproduces that obtained with simulations using "polarization-corrected" LJ parameters for the unlike pair interactions in water-carbon dioxide mixtures[78]. The authors of ref [78] used the SPC/E and EPM2 force fields to simulate CO_2 in liquid water and to accurately reproduce the experimental solubilities.

In the present study, the simulations were performed under periodic boundary conditions (PBC) and used the particle-particle particle-mesh (PPPM) Ewald method to treat long range electrostatics[3]. The cutoff radii for the nonbonded van der Waals interactions and for the Ewald summation of the electrostatics were chosen to be 11 Å, with switching distances starting from 10 Å. Because of the use of cutoffs for the LJ interactions, long-range

dispersion corrections for energy and pressure were applied[77]. The leap frog algorithm[43] was used to update positions every 0.5 fs.

Simulations of the turbostratically disordered clay layers is not a trivial task. Rotation of one clay layer relative to another destroys the periodicity of the systems which is problematic in simulations using PBC. To preserve periodicity, the clay systems represent a rectangular box with uneven sizes of alternating clay layers (designated as "small" and "large"). Thus, within a chosen angular range, rotation of small layers proceeds within the boundaries of the simulation box defined by large ones. This approach allows us to use PBC and to provide external clay surfaces (clay edges) and the interstitial space between the alternating layers accessible to the interlayer species. The interstitial space is produced because of gaps between adjacent replicas of small layers. In turbostratic clay systems, the clay layers are stacked in the z direction, so the rotation of a small layer relative to a large one occurs in the xy plane around the axis connecting geometrical centers of the layers and perpendicular to the internal clay surfaces. The [100] and [010] edges introduced by the presence of the small layers are determined by the structure of the unit cell. Because the Clayff force field[52] contains no bonding terms except for the hydroxyl groups, there are no broken chemical bonds at the edges.

The general chemical formula used for sodium montmorillonite is $Na_xMg_xAl_{3-x}Si_4O_{10}(OH)_2$-$nH_2O$, where the layer charge resides on the octahedral sheet (tetrahedral substitutions such as Al^{3+} for Si^{4+} can also occur in natural samples but they are not considered here). In addition to sodium ions, calcium and potassium (dry clay systems only) ions were also used as interlayer ions in the simulation models. The MMT structural model was created by replicating a pyrophyllite unit cell with an isomorphic octahedral Al^{3+}/Mg^{2+} substitution to produce a rectangular $22 \times 14 \times 1(18 \times 10 \times 1)$ supercell, in which the first set of numbers designates the size of the large layer and the second one (in parentheses) designates the size of the smaller layer. The initial dimensions of the simulation box in the x and y directions were 114.4 and 128.8 Å, respectively. The dimension in the z direction varies depending on the interlayer composition. The negative charge introduced by the substitutions is compensated by 366 sodium ions (or 183 calcium ions) residing in the interlayers.

The stoichiometry is $Na_{0.75}Mg_{0.75}Al_{3.25}(OH)_4(Si_4O_{10})_2$, with a layer charge of 0.75 per $O_{20}(OH)_4$. This results in a total of 19520 atoms constituting the clay phase. Additional simulations were performed for the dehydrated systems using a simulation box doubled in size in the z direction to ensure that there is no size effect on the results of simulations. In these tests, the systems are described with a $22 \times 14 \times 2(18 \times 10 \times 2)$ supercell. In addition, a $22 \times 12 \times 2(18 \times 10 \times 2)$ supercell was used to confirm independence of reported below results on the size of the interstitial space. MD simulations using a $8 \times 4 \times 4$ supercell were also carried out for dehydrated MMT systems to estimate equilibrium d_{001}-spacing values for clay systems providing exposure of the ions to internal surfaces only (i.e., without edges).

The water-CO_2 composition in the interlayer region is designated as $X - Y$, where X and Y are, respectively, the numbers of water and CO_2 molecules per unit cell. There are four types of interlayer compositions used in the simulations: the first one $(0 - 0)$ contains only interlayer ions without water and represents the dehydrated clay phase; the second $(X - 0)$ contains X water molecules per unit cell; the third $(0 - Y)$ includes Y carbon dioxide molecules per unit cell only, and the fourth $(X - Y)$ contains both X water and Y CO_2 molecules per unit cell. The maximum number of atoms engaged in the simulations was 40214 in the case of the clay system (Na-MMT with a $22 \times 14 \times 2$ $(18 \times 10 \times 2)$ supercell) with the 14-0 composition.

The initial positions of the ions, water, and carbon dioxide molecules were chosen randomly in a plane at the middle of the interlayers. They are placed nearly equidistantly from each other, and the plane dimensions are equal to the x and y dimensions of the large layer. For the dry, CO_2 only, and hydrated clay systems, multiple independent simulations starting from different initial structures were performed to ensure that the computed trends were consistent and were not affected by different initial positions. Because of the gaps between small layers, direct comparison of the energetic and structural parameters with those computed for systems without explicit presence of edges is not straightforward. Particularly, the numbers of water molecules per unit cell corresponding to the d_{001}-spacings at the stable hydration states (1W, 2W, etc.)[70, 53] are not the same for the systems considered in this work because water molecules reside in both the interlayer and the interstitial space. For the $X - Y$ compositions, the concentrations of CO_2 and H_2O in the interlayer and the interstitial

space could vary and depend on the initial positions of the species. However, regardless of that, the relative energetic and d_{001}-spacing trends as a function of the rotational angle (θ) remain the same. For the $X - Y$ compositions, the results are reported using the initial distribution of the species similar to that described above.

MMT with intercalated species was initially relaxed using MD simulations in the NVT ensemble carried out for 50 ps at T = 348.15 K. Subsequent equilibration was conducted for 1 ns using the NPT ensemble with the weak coupling Berendsen thermostat and barostat[45] at T = 348.15 K and P = 130 bar, conditions close to those existing in subsurface geological reservoirs and cap rocks and also close to those used in CO_2 intercalation experiments in clays carried out at National Energy Technology Laboratory (NETL)[61]. That step was followed by 20 ns production runs in the NPT ensemble at the same P-T conditions with semi-isotropic pressure coupling permitting the z-dimension to fluctuate independently from the x and y directions. Pressure was controlled by a Parrinello-Rahman barostat[47, 79] with a relaxation time of 4 ps, and the temperature was controlled by a Nose-Hoover thermostat[80, 46] with a relaxation time of 2 ps. The analysis of different terms contributing to the net potential energy was performed using the equilibrated clay structures. For that purpose, MD simulations were performed over 300 ps in the NVT ensemble using a Nose-Hoover thermostat[80, 46] with a relaxation time of 2 ps.

3.2.2 Rotational Pattern Model

Figure 10 shows a schematic diagram of two adjacent tetrahedral sheets formed by basal oxygens and silicon atoms starting from perfectly juxtaposed sheets and with rotation angles of 3, 6, 9, and 12° together with the 3D smectite structure (pyrophyllite was taken for simplicity with the expanded size of the sheets to fully capture the pattern at $\theta = 3°$). For perfectly aligned sheets, two ditrigonal rings of silicon tetrahedra linked by shared basal oxygens locate above each other and create a cavity shown in Figure 11a. Rotational mismatch results in complex cavities reflecting a variation in alignment of the ditrigonal rings across adjacent clay sheets. The variation in cavity structure is periodic, forming a Moiré

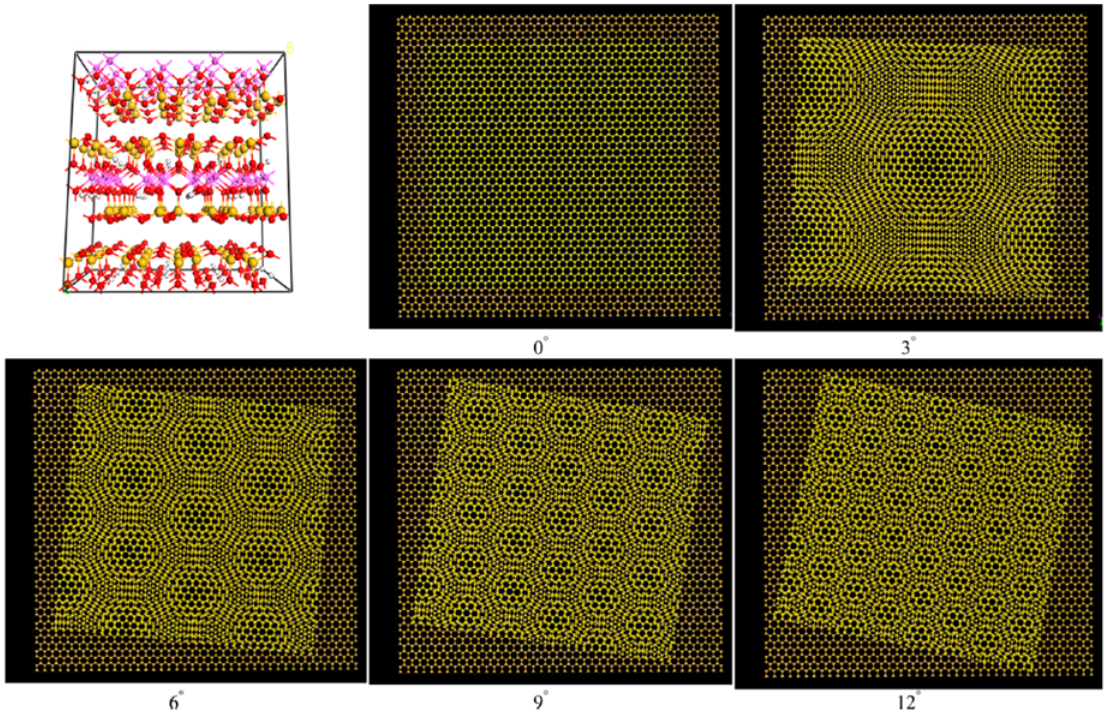

Figure 10: The [100] edge face of the 2:1 smectite clay structure (pyrophyllite) and Moiré patterns formed by two adjacent basal surfaces at 0-12° (from the [001] view). Color designation: red balls, oxygen; yellow, silicon; white, hydrogen; cyan, aluminum.

pattern with concentric circles of partially aligned ditrigonal rings separated by regions of no alignment (Figures 10 and 11b).

For small rotational shifts, the distances between the centers of the circles along a layer are given by

$$d_{MP} = \frac{d_a}{2sin(\frac{\theta}{2})} \tag{3.3}$$

where d_{MP} is the distance between centers of two circles in the Moiré pattern, d_a is the distance between centers of ditrigonal rings of the same layer and equal to the a lattice, and θ is the angle by which one layer is rotated relative to another. Assuming a d_a value equal to 5.20 /AA (a typical distance for the a lattice constant of MMT[81]) the calculated d_{MP} values are 99, 50, 33, and 25 Å for $\theta = 3°$, 6°, 9°, and 12°, respectively. Those numbers dictate that to capture the patterns, a sufficiently large model is required. To fulfill this requirement, the

size of the simulation box was chosen as described in section 2.1. The area of one unit cell (Figure 11b; inside the blue arrows) formed by the rotational pattern is further determined as

$$S_{MP} = d_{MP}^2 sin(\pi/3) = \frac{\sqrt{3}}{2} \frac{d_a^2}{(2sin(\frac{\theta}{2}))^2} \tag{3.4}$$

The area of the concentric circle itself is computed as

$$S_{IS} = \pi d_{IS}^2 = \frac{\pi d_a^2}{(2Fsin(\frac{\theta}{2}))^2} \tag{3.5}$$

where d_{IS} is the radius within which the shifted ditrigonal rings are still viewed as forming concentric circles, θ has the same meaning as in eq 3, and F is a factor determining the fraction of the unit cell that belongs to the circles. This formula is valid until d_{IS} is larger than the lattice parameter a. Assuming that the concentric circles occupy 1/3 of the unit cell area, the limiting value of the θ angle is 17.4°, after which the rotational pattern disappears. Thus, the chosen range of the rotational angles, [0-12°], passes through the various Moiré patterns and reflects the interval of angles consistent with TEM observations[72, 73, 74, 75] Another implication of this model is that the ratio of the unit cell area to the concentric circle area does not depend on θ. This means that the fraction of the concentric circles remains fixed during the limited range of rotation considered. From the mathematical model presented above, it follows that the number of cavities formed by basal oxygens of the adjacent layers (Figure 11a) is constant within the rotation range, although their distribution is varied. By definition, that number is smaller than the number of (undistorted) cavities for the 0° case, in which clay layers are perfectly aligned.

3.2.3 Methods To Study Rotational Disordering

The question of the time scales of rotational motion of clay layers is most intriguing. On one hand, the clay minerals in a geological formation could be exposed to geomechanical stress for decades, which essentially implies nearly equilibrium conditions for interlayer species during rotation. On the other hand, local perturbations of a subsurface geological reservoir due

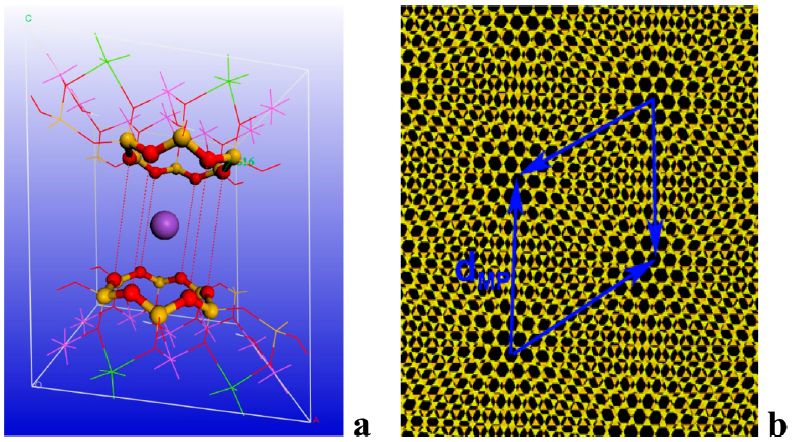

Figure 11: (a) A "cavity" formed by basal atoms of adjacent clay layers and (b) the unit cell of the Moiré pattern.

to CO_2 injection could create mechanical forces acting on clay-rich deposits to impose rotational motion of the layers at non-equilibrium conditions. Hence, our simulation approaches stem from the intention to simulate both rotational disordering occurring on geological time scales and during injection of a mobile phase into porous media of target formations. The method mimicking geological conditions deals with rotated clay systems with predetermined θ angles, at which interlayer species are equilibrated. The second method rotates alternating clay layers around a fixed axis with a constant angular velocity. Details of the two methods are given below.

I) Position Restraining:

In this approach, the rotationally disordered and 0° systems were initially prepared as described in section 2.1. The clay systems were equilibrated at θ = 0°, 3°, 6°, 9°, and 12°. The production runs with various compositions of the interlayer species were carried out using the procedure described above. To keep the atomic positions of the clay phase at the predetermined angles, the atoms were harmonically restrained in the xy plane at their reference positions using a force constant of 5000 kJ/mol.nm2. This approach provides no translational motion of the clay layers relative to each other. Those degrees of freedom

might be important for equilibration[82]. The z coordinates remained unconstrained, allowing the simulation box to adjust its dimension in that direction during the simulations. This approach provides equilibration of interlayer species in the turbostratic clay systems (monitored using constancy of potential energies and d_{001}-spacings over simulation time) at the rotational angles of interest.

II) Enforced Rotation:

Various methods for enforcing the rotation of subsets of atoms have been reported by Kutzner *et al.*[32] In the approach engaged in this work, a force is imposed on the group of atoms constituting the small clay layer by means of rotating a reference set of atomic positions, y_i^0 (coinciding with initial atomic positions of the small clay layer), at a constant angular velocity, ω, around a fixed axis defined through a geometrical center of the clay layer and that is perpendicular to the clay surfaces. The rotation is performed in such a manner that each atom with position x_i is connected by a "virtual spring" represented by a harmonic potential to its moving reference position: $y_i = \Omega(t)(y_i^0 - y_c^0)$, where $\Omega(t)$ given below is a dimensionless matrix describing the rotation around the axis, t is time, and y_c^0 is the geometrical center of the initial reference positions (in this case, it corresponds to the geometrical center of the small clay layer).

$$\Omega(t) = \begin{pmatrix} cos\omega t + \nu_x^2\xi & \nu_x\nu_y\xi - \nu_z sin\omega t & \nu_x\nu_z\xi + \nu_y sin\omega t \\ \nu_x\nu_y\xi + \nu_z sin\omega t & cos\omega t + \nu_y^2\xi & \nu_x\nu_z\xi - \nu_x sin\omega t \\ \nu_x\nu_z\xi - \nu_y sin\omega t & \nu_x\nu_z\xi + \nu_x sin\omega t & cos\omega t + \nu_z^2\xi \end{pmatrix} \tag{3.6}$$

where ν_x, ν_y, and ν_z are the components of the normalized rotation vector, ν and $\xi = 1 - cos\omega t$. To achieve unrestrained motion along the rotational axis and to allow adjustment of the d_{001}-spacing during rotation, the components of the potential parallel to the axis are removed. This is done by projecting the distance vectors between the reference and actual atomic positions onto the plane perpendicular to the rotation axis. Thus, the final form of the potential is

$$V^{rot} = \frac{k}{2}\sum_{i=1}^{N}\{\Omega(t)(y_i^0 - y_c^0) - (x_i - x_c) - \{\{\Omega(t)(y_i^0 - y_i^0) - (x_i - x_c)\}\nu\}\nu\}^2 \tag{3.7}$$

where k is a spring constant and x_c is the geometrical center of the group (the small clay layer), and x_i, y_i^0, y_c^0, ν, ω, and t are defined above. The details of the implementation can be found elsewhere[82]. The k value was chosen to be 100 kJ/mol.nm^2, which is low enough to ensure smooth transitions between atomic positions. To perform the enforced rotation, the clay systems were first equilibrated at various compositions of the interlayer species at $\theta = 0°$. Rotation was induced around the axis at an angular rate of $\omega = 0.01°$/ps over 1.2 ns with a step size of 0.5 fs. This produces a 12° rotation of the clay layers passing various Moiré patterns. Additional simulations were conducted using $\omega = 0.001°$ /ps to study the dependence of potential energy on the angular rate.

3.3 RESULTS AND DISCUSSION

Table 4 compares the d_{001}-spacings of dry M-MMT (M = metal ion) computed in this work with those from DFT calculations with dispersion corrections[32] and from experiment as inferred from the relative proportions of the different layer types as a function of relative humidity[83, 84, 85]. There is an overall good agreement between the computed and measured data, although the experimental d_{001}-spacing values are prone to large uncertainties because the experimental samples were prepared by dehydrating humidity-exposed clays, which may have caused the original structure not to be preserved[86, 87].

Table 4: d_{001}-Spacing Parameters for Dry M-MMT Systems.

ion	this work	DFT(vdW-TS)	exptl
Na^+	9.52 ± 0.02;(9.43 ± 0.01)	9.47^b	9.6^c; 9.6^d
Ca^{2+}	9.56 ± 0.02;(9.42 ± 0.01)	9.33^b	10.0^c; 9.6^d
K^+	10.24 ± 0.03;(9.83 ± 0.02)	9.88^b	10.0^c; 10.0^d; 10.2^e

[a] The values in parentheses are computed using a $8 \times 4 \times 4$ supercell. [b]Ref [32]. [c]Ref[83]. [d]Ref[84]. [e]Ref[85].

Figure 12 depicts equilibrated structures of dry Na-MMT at $\theta = 6^{\circ}$ (as an example). The disordering is represented as alternating clay layers rotated around an axis perpendicular to the internal clay surfaces. In a previous paper[18] using the same force fields[52, 53], we demonstrated that the expansion of the d_{001}-spacing of Na-MMT upon intercalation of water closely reproduces the experimental dependence of the d_{001}-spacing as a function of interlayer water content[65].

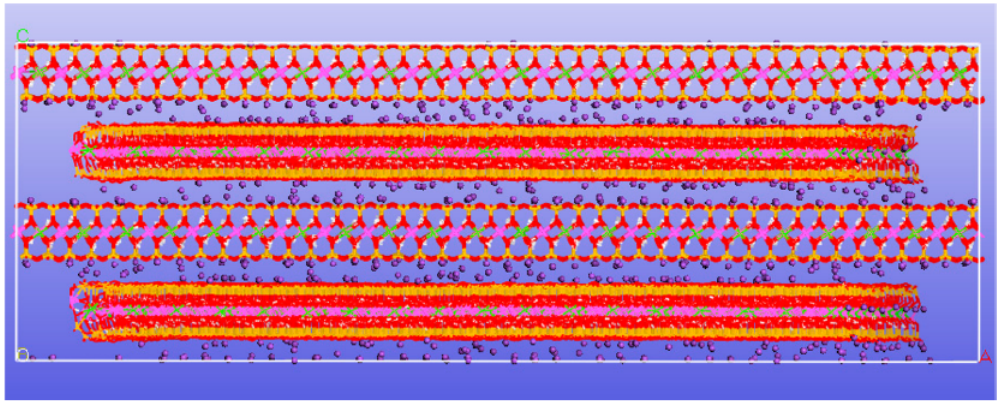

Figure 12: Equilibrium structure of the dehydrated Na-MMT system at $\theta = 6^{\circ}$. Color designation: red balls, oxygen; yellow, silicon; cyan, aluminum; green, magnesium; purple, sodium ion; white, hydrogen.

The d_{001}-spacing displays plateaux corresponding to a stable hydration states[65]. The predicted d_{001}-spacings are also consistent with recently reported data on Na-montmorillonite and Na-hectorite[70, 53, 88].

Figures 13 and 14 display, respectively, the relative changes in the potential energy and the d_{001}-spacing as a function of $X - Y$ interlayer compositions and the θ angle. These data were obtained using atomic positions constrained to predetermined θ angles. The upper part of each figure shows data without carbon dioxide, and the lower part reports results with intercalated CO_2. The interlayer spacing changes within a narrow 0.2 Å range (except the Ca-MMT system at the 5-2 composition, which displays a variation of up to 0.35 Å) upon rotation. The differences between the calculated enthalpy and potential energy changes are

negligible, so in the subsequent analysis, we use the potential energy as the quantity to analyze energy dependencies.

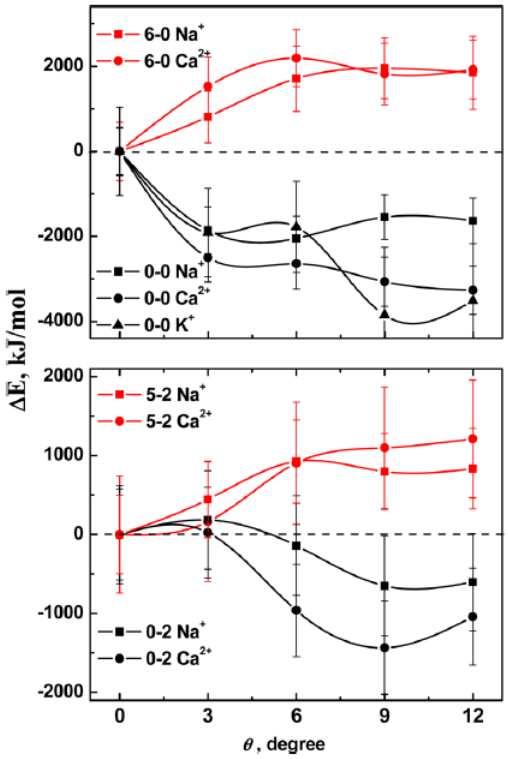

Figure 13: Relative potential energy change in M-MMT systems as a function of interlayer compositions and θ.

In general, the largest changes in the energy and structural parameters occur during rotation from 0° to 3°, and a further increase in θ perturbs the systems to a lesser extent(except for the 0.2 composition). This might be related to the fact that the ratio of the unit cell area to the concentric circle area does not depend on θ (see Computational Details). Consequently, the numbers of distorted and undistorted cavities remain fixed. Introduction of Ca^{2+} and K^{+} counterions produce more noticeable changes in the energy and interlayer distance than found for the Na^{+} ion. Thus, cations having larger ionic radii and charge affect the energy and the interlayer distance more. Below, we consider the dehydrated, hydrated,

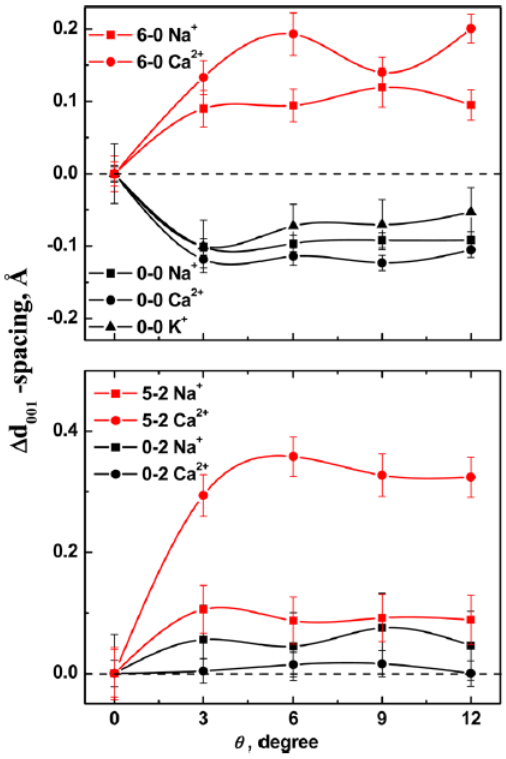

Figure 14: Relative d_{001}-spacing change in M-MMT systems as a function of interlayer compositions and θ.

and clay systems with intercalated carbon dioxide, paying attention to the energetic and structural changes and the density distributions of the interlayer species as a function of θ.

3.3.1 Rotation of Dry Clay Systems

For the dehydrated clay systems, the potential energies for the twisted structures are lower than for the structure at $\theta = 0$ ° (Figure 13). The corresponding d_{001}-spacings also demonstrate decreased values compared with the $\theta = 0$ ° case (Figure 14). The figures depict the intriguing result that the energy and the d_{001}-spacing are lower for the rotated dehydrated Na- and Ca-MMT systems than for the clay structures at $\theta = 0°$. The ions can be coordinated equidistantly to negatively charged basal oxygens of ditrigonal rings in perfectly

juxtaposed clay sheets (Figure 11a). Such coordination provides optimal interaction, resulting in lowering of total energy. Because rotation causes reduction in a number of those cavities, as evidenced by the formation of the Moiré patterns (Figure 10), the total energy of the system would have been expected to increase. Before addressing this issue, it is important to mention that the dry clay systems considered in this study are idealized structures. In reality, a smectite sample in the 0W hydration state is expected to have residual water bound to interlayer ions[83]. To check the effect of trace amounts of water on the potential energy and interlayer distance, a set of simulations using 0.25 water molecule per unit cell of Na-MMT was conducted. These simulations gave energies and d_{001}-spacings of rotated structures at $\theta > 0^{\circ}$ lower than the corresponding values at $\theta = 0^{\circ}$. Thus, even with a small amount of water present, the distribution of interlayer ions still controls the trends in relative energy and d_{001}-spacing depicted in Figures 13 and 14. We now turn to the results for the fully dehydrated Na- and Ca-MMT systems.

The atomic density profiles for the 0.0 composition depicted in Figure 15a indicate that Na^{+} ions (and Ca^{2+}, not shown) display two asymmetric peaks located near the basal planes designated by the dashed lines. The asymmetry is caused by different sizes of the alternating clay layers, as described in Computational Details. This trend does not depend on the initial positions of the ions. The analysis of the distances between the ions and the basal oxygens shows that ions associated with the density peaks are preferentially coordinated at the middle of the ditrigonal rings within 2.9 Å (estimated for sodium ions) from three and more basal oxygen atoms, thus meeting the criterion used to assign an ion as adsorbed[18].

This coordination does not depend on initial positions and is reproduced with independent simulations. Morrow *et al.*[88] also found that in dehydrated samples of Na-hectorite, the Na^{+} ions lie at the center of the hexagonal rings on the sheet to which they are closest. Similar observation was made in the MD simulations of Na-rectorate[89]. The number of ions is 0.75 (two times smaller in the case of Ca-MMT) per four ditrigonal rings (two on each surface) in a unit cell so that there is no competition for a coordination place that would otherwise force them to stay close to the interlayer center plane. At the middle of the ditrigonal rings, the counterbalancing ions are strongly electrostatically bound to surrounding basal oxygens. The equilibration step allows the interlayer ions to find their energetically favor-

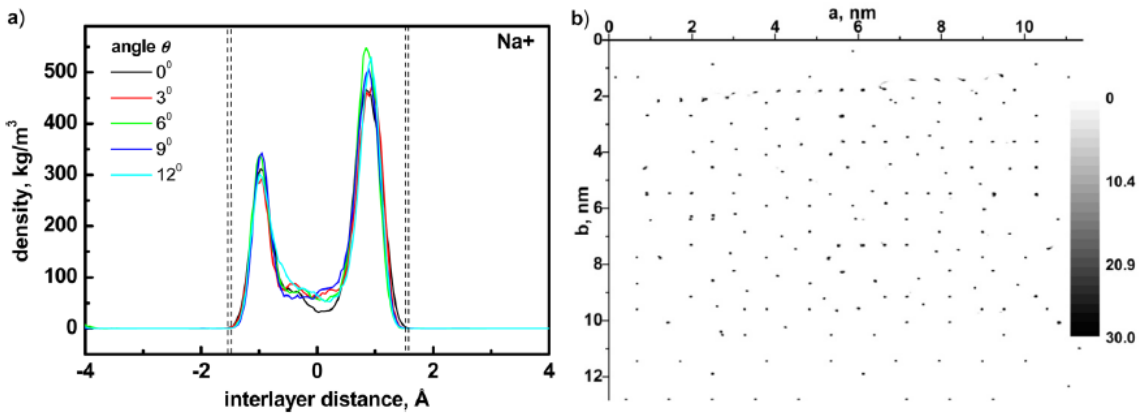

Figure 15: (a) Density profiles showing sodium ion distribution along the distance perpendicular to the internal surfaces of Na-MMT with the 0-0 composition at various θ values. Double dashed lines designate the range of positions of basal planes as a result of rotation. Profiles obtained by averaging over 5 ns of simulation time. (b) Density map (density in number/nm^3) showing the sodium ion distribution in the interlayer projected on a plane parallel to the internal surfaces of Na-MMT with the 0-0 composition at $\theta = 6°$. Results obtained by averaging over 5 ns of simulation time.

able configurations at each θ value considered. Such a process might mimic the situation occurring during dehydration of clay samples upon heating. Thus, under (geo)mechanical stress, the interlayer ions in smectite clay minerals slowly losing water would have sufficient time to adjust their positions and promote rotational disordering at least within the range of θ values considered in this work. Figure 15b depicts the two-dimensional density map for the sodium ions in the interlayer. The map was obtained by scanning the interlayer space to obtain density distributions in planes parallel to the clay surfaces with a step size of 0.1 Å. Then the distributions were projected on a plane and averaged for 5 ns of simulation time. The map shows that the sodium ions are localized with respect to their xy coordinates (similar distributions were obtained for the other θ angles). This, together with the density profile data, also confirms ion localization near the surfaces.

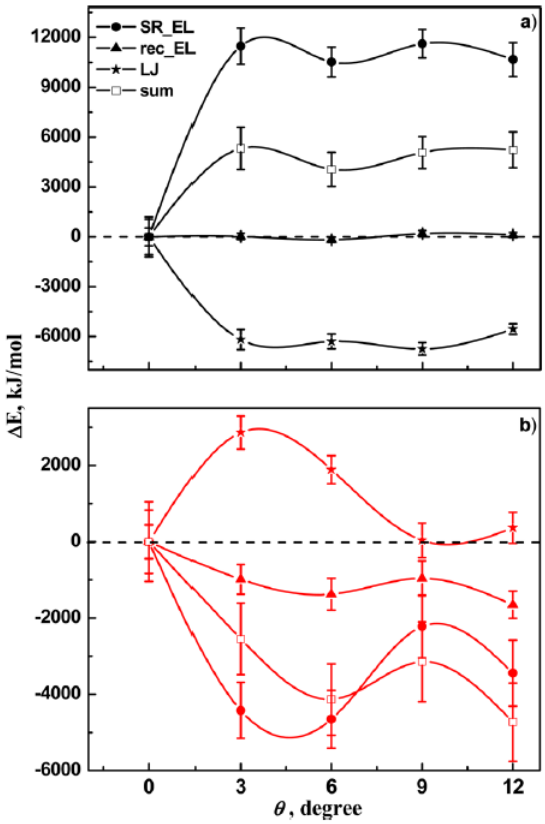

Figure 16: Comparison of real-space electrostatic (SR_EL), reciprocal electrostatic (rec_EL), Lennard-Jones (LJ) contributions and their total sum (sum) as a function of θ for the (a) 6-0 and (b) 0-0 compositions of Ca-MMT.

To gain insight into the interactions responsible for the computed energy trend, contributions from the various terms in the force field were extracted and analyzed. Figure 16 reports short-range (real-space sum accounting for pairwise interactions within a sphere of 11 Å, the cutoff radius), reciprocal space electrostatics and LJ contributions into the relative potential energies as a function of θ for the 6-0 (upper part) and 0-0 (lower part) compositions. The "position-restraining" and "long-range dispersion correction" (a minor modification to the Lennard-Jones terms to remove the noise caused by cutoff effects) terms provide insignificant contributions to the relative potential energies at different θ values (it should be mentioned

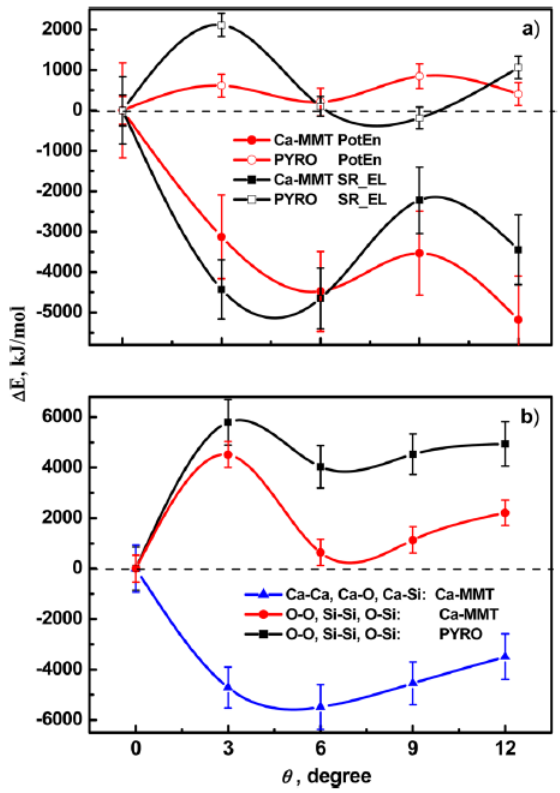

Figure 17: Comparison of (a) relative potential energies (PotEn) and real-space electrostatic contributions (SR_EL) and (b) atomic pairwise electrostatic contributions to relative potential energies in dry Ca-MMT and pyrophyllite with the 0-0 composition at various θ's.

that the weighted histogram analysis method[77] would be valuable for removing the bias due to the restraint and for estimating free energies as a function of θ, but it requires a special effort to be applied for these systems and was not considered in this work). For the hydrated system, rotation of the small layer relative to the large one leads to a large electrostatic destabilization, whereas the LJ contribution is energetically favorable. On the other hand, for the dehydrated system, the electrostatics favors the rotated structures with the LJ contribution being positive. Comparing the relative influence of the different terms in the force field, it is seen that short range electrostatic contributions are the most important for the overall energy change as a function of θ for both hydrated and dry MMT systems.

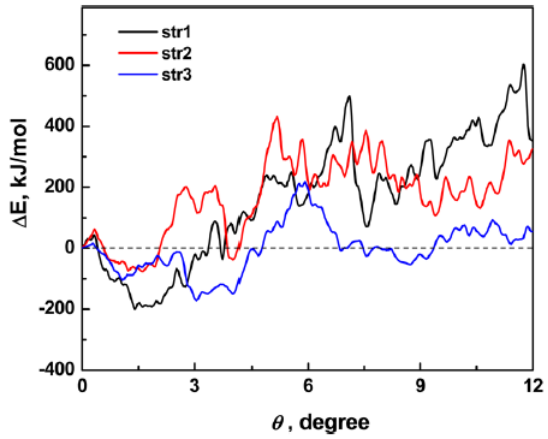

Figure 18: Potential energy changes during enforced rotation for three independently equilibrated Na-MMT systems (strs 1-3) with the 0-0 composition.

To estimate the role of electrostatic contributions involving interlayer ions, simulations were also carried out for pyrophyllite, which does not have octahedral and tetrahedral substitutions in TOT clay layers and, thus, bears neutral layers without interlayer ions. Figure 17 (upper part) depicts the relative potential energies and the relative real-space electrostatic contributions for pyrophyllite and Ca-MMT. The key atomic pairwise electrostatic contributions involving the ions and atoms of basal surfaces are depicted in the lower part of Figure 17. In contrast to Ca-MMT, the rotation of dry pyrophyllite is an energetically demanding process, and for both minerals, the electrostatic contribution to the relative potential energies determines the overall decrease/increase in the potential energies with rotation. The atomic pairwise contributions from the basal oxygen and silicon atoms provide a similar destabilizing impact for the rotated pyrophyllite and Ca-MMT systems. However, in the case of Ca-MMT, the electrostatic contribution involving interlayer ions induces a large stabilization upon rotation. Therefore, the overall decrease of the potential energy of nonhydrated MMT systems with rotation is primarily caused by interactions of interlayer ions with atoms of the clay surfaces.

We now turn our attention to exploring the energetic and structural changes during rotational motion of the small clay layer at a constant angular velocity using the enforced rotation approach. Figure 18 depicts the evolution of the potential energy as a function of θ. Three independently equilibrated Na-MMT systems with the 0-0 composition at $\theta = 0^\circ$ were used as starting points to initiate simulations, allowing for rotational movement of the small layer relative to the large one. The initial motion from $\theta = 0^\circ$ to $\theta = 0.1\text{-}0.2^\circ$ requires overcoming a potential barrier of around 25.50 kJ/mol. The barrier is associated with a deviation of the system from its equilibrium while the Moiré pattern is not yet developed (for the size of the clay system employed). After that, as soon as the Moiré pattern begins to form, further rotation leads to a decrease in the energy (and in the d_{001}-spacing, not shown) up to $\theta = 1.5\text{-}2^\circ$. The energy (and d_{001}-spacing) then increases upon further increase in θ (Figure 18). Analysis of the distribution of the interlayer ions during the enforced rotation shows that the rotational motion does not induce rearrangement of the ions adsorbed at the centers of ditrigonal rings. The energy decreases for $\theta = 0.2$ - 2 $^\circ$ because the ions remain close to equilibrated positions at $\theta = 0^\circ$. However, rotation to larger angles ($> 3^\circ$) causes more unfavorable ion-ion interactions between ions adsorbed at the opposite internal clay surfaces. Those interactions counterbalance the energy decrease that would otherwise result because of rotation. As a result, further disordering beyond 2-3° would be significantly retarded.

The simulated rotational motion models the disordering occurring in dehydrated or nearly dehydrated smectite minerals. The energy trends obtained using the enforced rotation are different from those found with the position constraints. The differences originate from the fact that the latter approach allows relaxation of the ion positions at fixed rotational angles, whereas in the former, the ions remain adsorbed at positions corresponding to $\theta = 0^\circ$. The rate of the motion, which is limited by computational cost, is apparently much greater than that occurring in nature and proceeds under nonequilibrium conditions. To explore rotational motion at a reduced angular speed, simulations were performed using a rotational velocity of 0.001°/ps. The predicted trends in energy and d_{001}-spacing remain similar to those discussed above. This implies that under mechanical stress, nearly dry smectite clay minerals would be susceptible to rotational disordering within the narrow θ range.

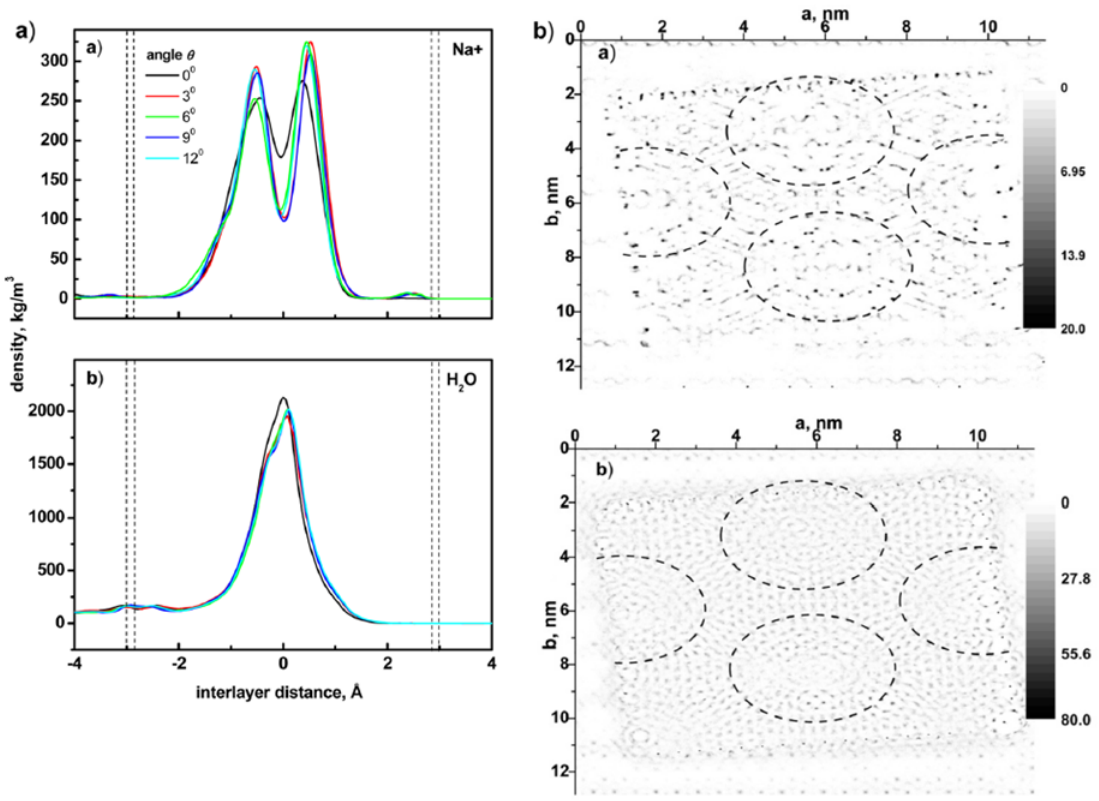

Figure 19: (a; left) Density profiles showing (a) sodium ion and (b) water molecule distributions along the distance perpendicular to the internal surfaces of Na-MMT with the 6-0 composition at various θ. Double dashed lines designate the range of positions of basal planes as a result of rotation. Profiles obtained by averaging over 5 ns of simulation time. (b; right) Density maps (density in number/nm^3) showing (a) sodium ion and (b) water molecule distributions in the interlayer projected on a plane parallel to the internal surfaces of Na-MMT with the 6-0 composition at $\theta = 6°$. Results obtained by averaging over 5 ns of simulation time. The Moiré pattern is highlighted with dotted circles.

To explore an effect of the Moiré patterns on the potential energy of dry smectites, simulations with backward enforced rotation of MMT systems were carried out for clay structures at nonzero θ values. Figure 35 (Appendix) collects potential energy curves computed during backward rotation for Na-MMT structures with interlayer ions equilibrated using the

position restraining method at $\theta = 3°$, $6°$, and $9°$. The curves develop distinct peaks when rotation of the small layers passes the position of perfectly juxtaposed clay layers at $\theta = 0°$. The deviation from that position in both clockwise and counterclockwise directions leads to a decrease in energy. Thus, formation of the rotational patterns of adjacent clay surfaces induces a decrease in the potential energy (and d_{001}-spacing) of the dehydrated smectites.

3.3.2 Rotation of Hydrated Clay Systems

According to Figures 13 and 14, rotation of the clay layers of hydrated Na- and Ca-MMT requires energy and is accompanied by expansion of the interlayer distance. The overall trends in energies, d_{001}-spacings, atomic density distributions, and radial distribution functions are similar for the 2-0, 4-0, 6-0, and 8-0 compositions. We now examine in more detail the results of the simulations for the 6-0 composition, which provides a water monolayer and a d_{001}-spacing equal to 12.10 ± 0.03 Å ($\theta = 0°$). That equilibrated spacing falls within the experimentally determined range of the 1W hydration state (11.5-12.5 Å)[65] and corresponds to the calculated stable hydration state[11, 52, 90, 91]. As a function of θ, Figure 16 (upper part) displays the various contributions to the relative potential energy. The figure shows that electrostatics plays the primary role in the overall increase of the relative potential energy upon rotation. Detailed analysis of the pairwise contributions relative to the zero-degree system shows that the electrostatic contributions from the basal oxygen-basal silicon, ion-basal oxygen, and water-water interactions contribute to the overall increase in the relative potential energy. Hence, the electrostatic contribution due to the water network is less stabilizing for rotated than nonrotated clay layers (Appendix Figure 36).

As a function of θ, Figure 19a displays the density profiles of the sodium ions and water molecules (the profile does not distinguish individual atoms in the molecules) in the interlayer for the 6-0 composition. The density profile of water develops a maximum at the interlayer center with a low shoulder caused by coordination of water molecules to the clay layer edges. The density profile of the sodium ions is characterized by two peaks that occur close to the interlayer center. Interestingly, beginning with the $\theta = 3°$ system, the profiles develop more

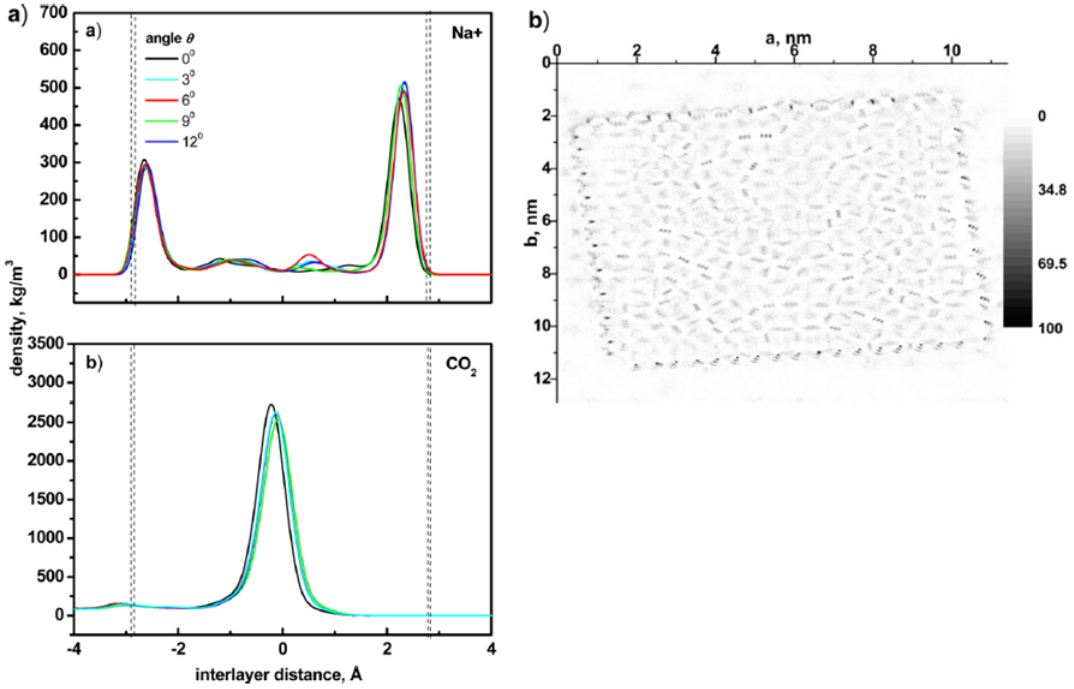

Figure 20: (a; left) Density profiles showing (a) sodium ion and (b) carbon dioxide molecule distributions along the distance perpendicular to the internal surfaces of Na-MMT with the 0-2 composition at various θ values. Double dashed lines designate the range of positions of basal planes as a result of rotation. Profiles obtained by averaging over 5 ns of simulation time. (b; right) Density maps (density in number/nm^3) showing carbon dioxide molecule distributions in the interlayer projected on a plane parallel to the internal surfaces of Na-MMT with the 0-2 composition at $\theta = 6°$. Results obtained by averaging over 5 ns of simulation time.

pronounced peaks relative to $\theta = 0°$. This indicates that upon rotation, ions are driven away from the interlayer center toward the basal planes.

The process might be related to the less stabilizing impact of water-water electrostatics to the potential energy of the rotated systems.

Figure 19b shows the 2D density maps of the ions and water molecules for the 6-0 composition. Examination of Figures 10, 19b, and Supporting Information 37 (given for $\theta = 0°$) shows that the H_2O molecules and sodium ions create patterns reminiscent of the Moiré patterns for nonzero θ values. This striking feature indicates that rotational disordering affects the structural arrangement of the interlayer species for hydrated montmorillonite. Similar results are obtained from analysis of the simulation data for Ca-MMT. The density distribution map also demonstrates that the ions actively explore the interlayer space in the xy planes parallel to the clay surfaces. This is distinctly different from the distribution of the ions at the 0-0 composition that revealed sharp localization in the xy plane (Figure 15b). This is a consequence of the fact that solvation by water molecules provides greater ion mobility in the interior.

In the simulations of Na-MMT with the 6-0 composition using enforced rotation, the energy and d_{001} spacing are higher for rotated structures than for the system with $\theta = 0°$ (not shown). The energy curve reaches a plateau and stays relatively constant during the rotation starting from $\theta > 2 - 3°$.

So far, we have considered the hydrated clay systems with water monolayer exposed to the Moiré. patterns of clay sheets. Supporting Information Figure 38 shows the potential energy changes as a function of θ computed using both the position constraining and enforced rotation methods for the Na-MMT with the 14-0 composition. This composition produces a bilayer configuration of water molecules (as confirmed by the density profile) in the interlayer with the equilibrated $d_{001} - spacing$ equal to 14.67 $\pm$ 0.03 Å, the value that falls into the experimentally determined 2W hydration state range (14.5-15.5 Å)[65] and close to the calculated stable hydration state[11, 52, 90]. In this case, both methods predict that rotation from $\theta = 0°$ is an endothermic process accompanied by the increase in the d_{001}-spacing. The density profiles (not shown) support the preferential location of the sodium ions near the center of the interlayer space and their solvation by water molecules. This is in line with the recent DFT-based molecular dynamics and Monte Carlo simulations of optimal ion positions in the interlayer space of hydrated montmorillonite[92]. In contrast to the system with

the 6-0 composition, the calculated density maps indicate that ion distribution is relatively unaffected by the Moiré pattern; the same is true for the water molecules, although they develop a cage-like pattern owing to the presence of an adjacent basal surface (Supporting Information Figures 39-41). The pictures provide the distribution maps computed for the ions and separately for water layers in a bilayer configuration at $\theta = 6^{\circ}$ as an example (the distributions for the other angles are similar). Thus, the Moiré pattern exerts little influence on the distribution of the interlayer species for clay expanded into the 2W (and presumably also higher) hydration state.

3.3.3 Rotation of Clay Systems with Intercalated CO_2

As seen from Figures 13 and 14 the potential energy of the clay systems with 0-2 composition undergoes a slight increase as θ increases from 0° to 3°, then decreases for higher rotational angles relative to the 0° case. The corresponding d_{001}-spacing experiences a marginal expansion upon rotation. Under experimental conditions, intercalation of carbon dioxide requires a residual amount of water present in the interlayer space[14, 63, 15]. The 0-2 composition considered here is an idealized system not likely observable experimentally. In contrast to this, rotation of the clay system with the 5-2 composition is accompanied by an increase in both the potential energy and the d_{001}-spacing (Figures 13 and 14).

Figure 20a and b depicts the density profiles for Na^{+} ions and carbon dioxide molecules and density distribution maps for carbon dioxide molecules in Na-MMT with the 0-2 composition. The resulting profiles of the sodium ions are reminiscent of those found for the 0-0 composition (Figure 15a). The density map of the Na^{+} ions (not shown) is also similar to that depicted in Figure 15b. Krishnan et al[70]. reported a detailed analysis of the dynamics of sodium ions and carbon dioxide molecules in the interlayer space of Na-MMT. They found that the ions primarily adsorbed at the surfaces, with some ions being located in the interior. Similar results are obtained in this work and depicted in Figure 20a, showing two minor peaks near the interlayer center.

The density profile of carbon dioxide displays a maximum at the middle of the interlayer (Figure 20a). Thus, carbon dioxide and the sodium ions avoid each other, consistent with previous data[18, 70].

Comparison of the density maps for the nonzero θ value (Figure 20b) and for $\theta = 0°$ (Appendix Figure 42) has revealed that the CO_2 distribution is affected by the Moiré patterns formed by the basal surfaces. However, the distribution is less structured, to be recognized as the Moiré pattern like that depicted in Figure 19b for water molecules. Similar trends were found for the Ca-MMT system.

Figure 21 reports the density profiles at various θ values and density distribution maps of the interlayer species for the 5-2 composition of Na-MMT. The sodium ion profile displays two peaks located in the interior of the interlayer space similar to the profile for the 6-0 composition (Figure 19a), suggesting that the ions become preferentially solvated by water molecules. Moreover, in line with Figure 19a, rotation of the clay sheets causes a slight increase in the separation of the peaks in the Na^+ distribution. For the 5-2 composition, the CO_2-H_2O mixture forms a monolayer correlating with the maxima of the density profiles. At the positions of the layer edges, the carbon dioxide profile develops a distinct broad shoulder and the density profile of water demonstrates a small peak (Figure 21a). The density distribution map of carbon dioxide shows elevated density in the interstitial space and at the edges of the small layer that gives rise to the shoulder seen in the density profile.

Similarly, the density distribution map of water displays an increase in density around the layer edges, although to a much lesser extent (Figure 21b). Apparently, the 5-2 composition (and 5-1, not shown) creates a mixture with a supersaturated concentration of carbon dioxide, and during equilibration, the excess of CO_2 moves from the interlayer to the interstitial space. In our earlier work, the 5-2 composition resulted in the equilibrium d_{001}-spacing equal to 14.49 ± 0.02 Å, which falls within the range of the 2W hydration state[18]. The Na-MMT model employed in that work provides exposure of the interlayer species only to the internal clay surfaces (no edge effects). In this study, because the interlayer species have access to the interstitial space and edges, the equilibrium d_{001}-spacing decreased to 12.17 ± 0.02 A ($\theta = 0°$), close to the value for the 6-0 composition (see section 3-2). Interestingly, the carbon dioxide remaining in the interlayer region tends to agglomerate and form

elongated clusters (conglomerates) separated by water molecules with a residual amount of solvated CO_2 (Figure 21b). To explore the stability of such clusters, production simulations of Na- and Ca-MMT at $\theta = 6^\circ$ were conducted up to 200 ns to monitor potential energy, d_{001}-spacing changes, and density distribution maps. At the end of the simulations, the density distributions remain unchanged, as reported in Figure 21. Density maps of water molecules display nonuniform distributions reflecting the presence of agglomerated carbon dioxide molecules in the interlayer. There are no noticeable patterns formed by water that might be connected to the Moiré patterns of basal surfaces, as found for the 6-0 composition (Figure 21b). The hydrogen bonding between the interlayer species and the basal oxygens affects the energetic properties of clay systems. In this regard, it is instructive to explore hydrogen bond lifetimes as a function of interlayer composition and θ. To accomplish this, the approach described in ref [93] was engaged.

The analysis of the calculated hydrogen-bond lifetimes for water-clay, water-water, and water-carbon dioxide pairs in Na- and Ca-MMT at different θ values shows that the rotational disordering does not significantly impact the H-bond lifetimes. The water-water and water-basal oxygen hydrogen lifetimes computed for the 6-0 and 5-2 compositions have comparable values (the water-carbon dioxide values are an order of magnitude smaller, consistent with our previous results)[18]. This means that in the interlayer, the water molecules are strongly engaged in interactions with the basal surfaces. On the other hand, in the open environment, the H-bonding of water to a single smectite surface is weaker than H-bonds between water molecules[94, 95, 96].

The simulations of Na-MMT systems for the 0-2 and 5-2 compositions using the enforced rotation approach demonstrate a rise in the relative potential energy (and d_{001}-spacing) upon rotation (not shown). The energy increases even for the 0-2 composition that is found to demonstrate the opposite trend using the position restraint approach. This is attributed to nonequilibrium configurations of the interlayer species during enforced rotation. Specifically, deviation of the clay layers from $\theta = 0^\circ$ induces an increase in the potential energy of the system.

To provide smoother rotation motion, the angular speed was decreased by an order of magnitude to 0.001°/ps. However, it did not reverse the trend, meaning that the 0-2 system

is more sensitive to equilibration of the interlayer species than the 0-0 system, which displays a decrease in the energy and the interlayer distance at the small θ values (0-2°) (Figure 18).

In the discussion above, it was assumed that interlayer species possess the ability to leave the interlayer and enter the interstitial space between clay particles. This is possible if clay generally exists as particles of a limited size and thickness. In the series of works by Nadeau *et al.*[97, 98] it was found using XRD and TEM measurements that naturally occurring interstratified illite-smectite and chlorite-smectite and pure smectite are mixtures of thin particles of finite sizes rather than a continuous crystal phase. Interestingly, the samples of illite-smectite and chlorite-smectite display rotational turbostratic electron diffraction patterns, presumably as a consequence of clay particle agglomerates[97, 98]. For Wyoming montmorillonite, the samples show a predominance of clay particles a few thousand angstroms in size but only 10-20 Å thick. A mobile phase migrating through a geological formation enriched with swelling clays can fill the interstitial space between the clay particles and, thus, be exposed to external mineral interfaces.

Carbon dioxide molecules can become trapped in the interlayer in amounts exceeding an expected CO_2 solubility at the prevailing P-T conditions. It has been shown experimentally that exposure of dry $scCO_2$ to montmorillonite in the $>$ 2W hydration state may result in a collapse of the d-spacing to that of the 1W state[58, 14]. During that process, a portion of the water molecules leaving the interlayer can be substituted with carbon dioxide molecules. A significant portion of (wet) $scCO_2$ might remain in the interstitial region between clay particles. Recently, MD simulations were used to study the exchange of water and counter-balancing ions between the micropores and clay interlayers in Na-montmorillonite with open [010] edges[99]. It was found that for water content at the 2W hydration state, the exchange proceeds practically without a barrier for water and the ions. Energy barriers for exchange of carbon dioxide, water, and ions between the interlayer and (wet) $scCO_2$ in the interstitial space and pores are unknown. A study aiming at an estimation of those barriers would be a valuable addition to our understanding of the mechanism of carbon dioxide interaction with swelling clay minerals.

Another scenario involves intercalation of CO_2 during expansion of swelling clay minerals that might be at fractional hydration states[88, 100, 101] (although it is generally believed

that smectite samples exist as a set of "quantized" hydration states, i.e., (0W, 1W, 2W, 3W))[83, 102, 103] Experimentally, it was found that a residual amount of water is required for successful intercalation of CO_2 in the interlayer space that expands until the d_{001}-spacing corresponds to that of the 1W hydration state[15, 13]. Interaction of Na- and Ca-exchanged-MMT samples at the 2W hydration state with variably wet $scCO_2$ can lead to swelling to the d_{001}-spacing equal to the 3W state[58, 14]. As mentioned in the Introduction, the largest expansion occurs for MMT samples at a sub-1W hydration state and is accompanied by an increase in the d_{001}-spacing from 11.3 to 12.3 Å after exposure to gaseous CO_2[15] or to 12.1 Å after interaction with anhydrous $scCO_2$[58, 14].

The formation of CO_2 conglomerates trapped in the interlayer is supported by Schaef *et al.*[14] and Rother *et al.*[60], who indicated that CO_2 does not displace H_2O when entering the sub-1W interlayer but "rather makes room by pushing the structural units apart", and by simulation data of Yong and Smith[20], who reported the interlayer of Sr-MMT showing water molecules clustering around the ions and away from substitutions in the octahedral layer and formation of unoccupied regions. That unoccupied space might be filled in by another species such as carbon dioxide in a two-step mechanism ("prop and fill") implying the existence of (meta)stable partially filled hydration states. In our work, we found conglomerate formations for both Na- and Ca-MMT clay systems, suggesting that CO_2 can be a filler to stabilize swelling clays during expansion. It is also important to realize that hydration energies of interlayer ions, isomorphic substitutions in octahedral, and especially tetrahedral layers would be leading factors determining trapping of CO_2 as conglomerates in smectites minerals. In the models employed in this work, only substitutions in the octahedral layer were made, so the interlayer species exposed to the basal surface were indirectly affected by charge imbalance brought by the magnesium for aluminum substitutions.

3.4 SUMMARY

This study has shown that rotational disordering, a common naturally occurring process, affects the distribution of ions, water, and carbon dioxide molecules in the interlayer of

swelling clays. The computed density maps reveal that the interlayer species in a monolayer configuration follow the rotational Moiré patterns formed by the basal surfaces of adjacent clay layers. The simulations indicate that rotational disordering of hydrated montmorillonite and montmorillonite with intercalated water and carbon dioxide is an energetically demanding process, as found using the position constraining and enforced rotation approaches for θ = 0-12°. For all compositions considered, the potential energy demonstrates a tendency to reach a plateau for θ = 6-12° that is attributed to a fixed number of undistorted/distorted cavities for Moiré patterns. Turbostratically stacked clay layers with intercalated water and water-CO_2 also experienced expansion of interlayer space by 0.1-0.2 Å, depending on the nature of interlayer ions.

Turbostratic dry and nearly dry montmorillonite systems are predicted to be more stable than the nonrotated system. Rotation is accompanied by a decrease in the d_{001}-spacing by ∼0.1 Å. This process is explained in terms of favorable interactions of interlayer ions adsorbed at the clay surfaces. During equilibration, the ions find optimal positions in the interlayer, causing a decrease in the potential energy and the d_{001}-spacing. In a geological formation, this process may be anticipated during slow dehydration of expandable clays under geomechanical stress. Under such conditions, the clay layers would be prone to rotational disorder and to become turbostatically stacked in the presence of external forces shifting the clay particles. The calculation using enforced rotation of clay layers shows that perfectly oriented dehydrated montmorillonite has only a limited range (θ = 0-2°) for rotational disordering, and further rotation would be energetically restricted.

The results of the simulations have also shown that CO_2 might be trapped in the interlayer of hydrated montmorillonite in an amount exceeding its solubility in water at prevailing P-T conditions in subsurface geological formations. This is possible because carbon dioxide conglomerates become trapped in the interlayer and are surrounded by water molecules with solvated CO_2. Thus, the expandable clay layers provide a confining environment for such carbon dioxide retention. This trapping mechanism could be important in estimations of a storage capacity for selected geological sites.

3.5 SUPPORTING INFORMATION

Eight figures, describing potential energy change, electrostatic contributions of various atom pairs, 2D density maps, relative potential energy and d_{001} spacing change in Na-MMT systems, are included in the Appendix section. This material is also available free of charge via the Internet at http://pubs.acs.org.

3.6 ACKNOWLEDGMENTS

This technical effort was performed in support of the National Energy Technology Laboratory's ongoing research in Subtask 4000.4.641.061.002.254 under the RES Contract $DEFE0004000$. The simulations were carried out on the NETL High-Performance Computer for Energy and the Environment (HPCEE) and on the computer clusters in the University of Pittsburgh's Center for Simulation and Modeling. This project was funded by the Department of Energy, National Energy Technology Laboratory, an agency of the United States Government, through a support contract with URS Energy and Construction, Inc. Neither the United States Government nor any agency thereof, nor any of their employees, nor URS Energy & Construction, Inc., nor any of their employees, makes any warranty, expressed or implied, or assumes any legal liability or responsibility for the accuracy, completeness, or usefulness of any information, apparatus, product, or process disclosed, or represents that its use would not infringe privately owned rights. Reference herein to any specific commercial product, process, or service by trade name, trademark, manufacturer, or otherwise, does not necessarily constitute or imply its endorsement, recommendation, or favoring by the United States Government or any agency thereof. The views and opinions of authors expressed herein do not necessarily state or reflect those of the United States Government or any agency thereof.

I extracted this chapter from a published paper: *"Molecular Dynamics Simulations of Turbostratic Dry and Hydrated Montmorillonite with Intercalated Carbon Dioxide"*, and my collaborators for this paper were E. Myshakin, V. Romanov, K. Jordan and G. Guthrie.

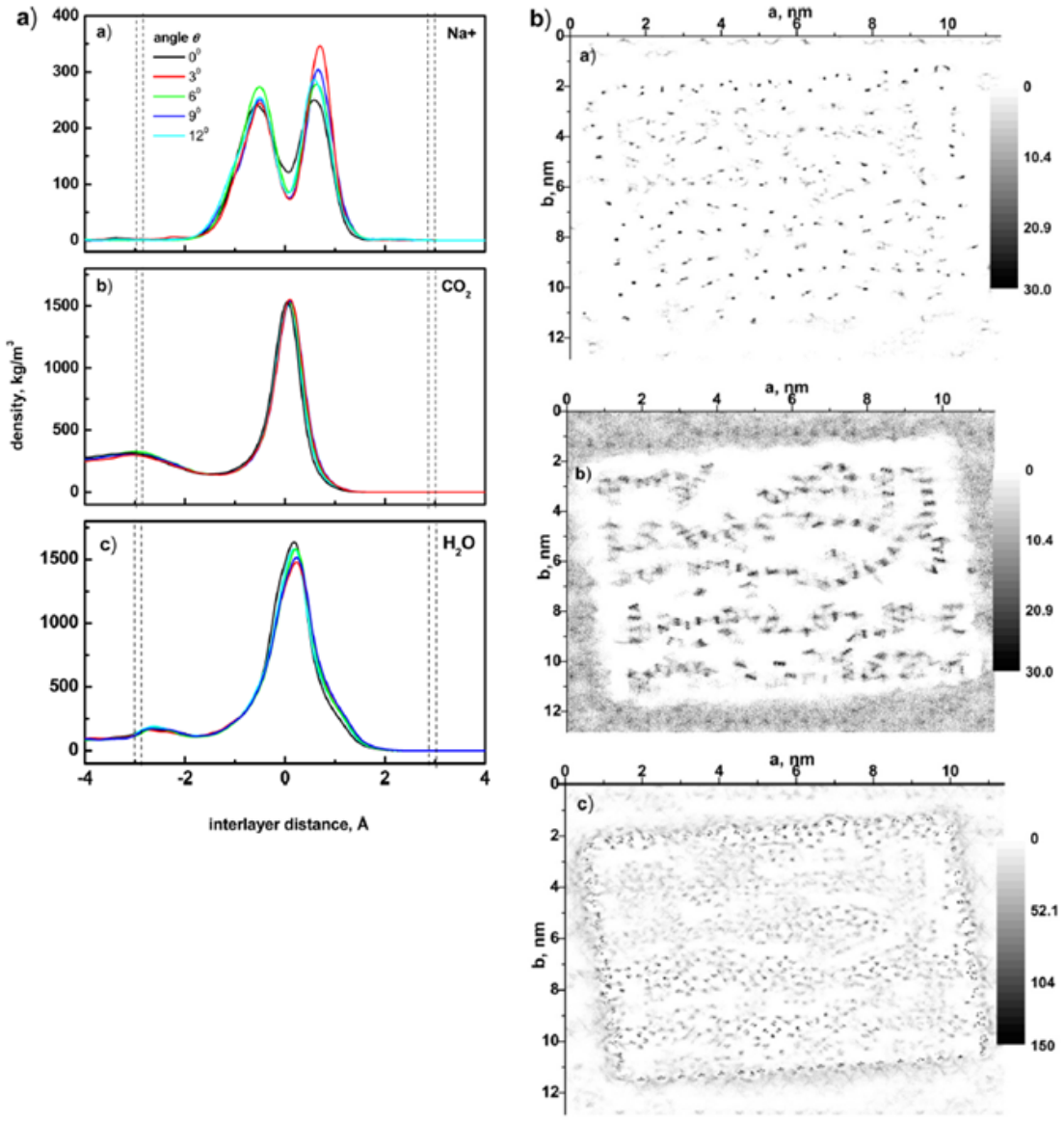

Figure 21: (a; left) Density profiles showing (a) sodium ion, (b) carbon dioxide, and (c) water molecule distributions along the distance perpendicular to the internal surfaces of Na-MMT for the 5-2 composition at various θ. Double dashed lines designate the range of positions of basal planes as a result of rotation. Profiles obtained by averaging over 20 ns of simulation time. (b; right) Density maps (density in number/nm^3) showing (a) sodium ion, (b) carbon dioxide, and (c) water molecule distributions in the interlayer projected on a plane parallel to the internal surfaces of Na-MMT with the 5-2 composition at $\theta = 6°$. Results obtained by averaging over 20 ns of simulation time.

4.0 FREE ENERGY CALCULATIONS TO PREDICT CLAY SWELLING BEHAVIOR

4.1 INTRODUCTION

Burning of fossil fuels releases large quantities of CO_2, a greenhouse gas, into the atmosphere, and there is compelling evidence that this is having a significant impact on the global temperature[104]. Sequestration of CO_2 in deep underground sedimentary layers is an approach widely suggested to reduce greenhouse gas emission[4]. In this approach, supercritical CO_2 ($scCO_2$) would be injected into deep rock formations. Successful sequestration depends on cap rocks being impermeable to CO_2. Cap rocks and host rock matrix can be enriched with swelling clays (smectites) such as montmorillonite and beidellite. The interaction of $scCO_2$ with hydrated smectites results in intercalation of CO_2 into interlayer regions[15, 13, 60, 58].

Montmorillonite (MMT) and beidellite (BEI), which is a less common smectite clay mineral, are layered 2:1 dioctahedral phyllosilicates comprised of octahedral (O) sheets sandwiched between tetrahedral (T) sheets giving a TOT structure as show in Figure 22. In the absence of substitutions, the T sites are comprised of SiO4 units and the O sites of AlO6 units. Structural hydroxyl groups are also present in the coordination sphere of the octahedral metal. In 2:1 phyllosilicates one of three symmetrically unique octahedral sites is not occupied by a cation. MMT has predominant isomorphic substitutions of Al^{3+} ions by Mg^{2+} ions in the O sheet, while BEI samples tend to be dominated by isomorphic substitutions of Si^{4+} ions by Al^{3+} in the T sheets. Both types of substitution result in a net negative charge for the clay layer, which is balanced by interlayer cations such as Na^{+}, Li^{+}, and Ca^{2+}. Hydration of the cations causes swelling of smectites and an increase of the d_{001}-

spacing[105, 22]. In natural samples of MMT, some substitutions can also occur in the T and O sheets. Similarly, in natural samples of BEI, some substitutions occur in O sites. However, for simplicity we consider the ideal substitutions described above. This allows us to study the effect of location of the negative charges, exposed directly to interlayer species or screened by the silicon-oxygen polyhedra, on swelling behavior. Other factors affecting swelling behavior include the size and charge of the interlayer cations[19, 20], the positions of the hydroxyl groups in the octahedral layer with respect to the vacancies in octahedral sites, resulting in cis-vacant or trans-vacant smectites[21], and the magnitude of negative charges on the clay sheets[22]. The expansion of smectites due to exposure to water and CO_2 improves the sealing properties of cap rocks, whereas shrinkage could lead to fracturing and undesirable release of injected CO_2 into the atmosphere[13].

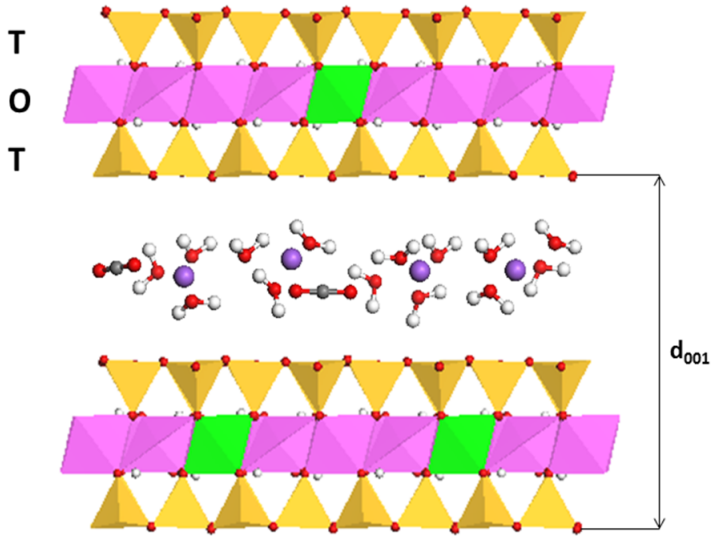

Figure 22: Smectite structure containing TOT sheets, counterions, and intercalated water and CO_2 molecules. The color coding of atoms is: purple, red, white, grey, yellow, pink and green for Na, O, H, C, Si, Al and Mg, respectively.

The swelling of smectite clays due to water intercalation is well understood from previous studies with emphasis on montmorillonite as one of the most abundant smectite minerals[106, 6, 7, 107, 108, 8, 9, 10, 11], while beidellite has received less attention[92, 109, 110]. Previous calculations on MMT indicate that at equilibrium water can form a monolayer with basal

d_{001}-spacings ranging from 11.5 to 12.5 Å (the 1W hydration state) or a bilayer with basal d_{001}-spacings ranging from 14.5 to 15.5 Å (the 2W hydration state)[11, 92, 65, 52]. The relative stability of the 1W and 2W hydration states depends on the type of interlayer ions[41]. In this work 1W and 2W are used, respectively, to refer to the monolayer and bilayer configurations of interlayer molecules for both the pure water and for CO_2-H_2O mixtures.

Smith used Monte Carlo simulations to investigate the swelling of hydrated Cs-MMT and to calculate the immersion energy to establish the hydration state corresponding to the global free energy minimum[41]. The minimum was found to be consistent with the experimental result[34, 111]. In subsequent work, Young and Smith[20] calculated the structural parameters for three different MMTs and found that for Cs-MMT-H_2O formation of a single water layer in the interlayer region leads to the most stable structure, while for Na-MMT-H_2O and Sr-MMT-H_2O the 2W hydration state was predicted to be more stable than 1W. The energetic contributions to the swelling free energy were calculated by Whitley and Smith[90], who reported that hydration of the counter-ions plays a dominant role in the swelling behavior of MMTs.

Interaction of carbon dioxide with hydrated smectites is a complex phenomenon[58, 14]. For example, exposure of dry $scCO_2$ to MMT samples in the 2W and higher hydration states can induce a collapse of the d_{001}-spacing to that of the 1W state[58, 14]. On the other hand, interaction of MMT samples with wet $scCO_2$ promotes swelling of clays to either 1W or 2W hydration states[15, 13, 58, 14].

The interaction of carbon dioxide and simple hydrocarbons with hydrated swelling clays has been studied using computer simulation methods[92, 109, 110, 112, 113, 114, 94, 53, 18, 115, 116, 26, 27, 28, 29]. Molecular dynamics (MD) simulations have been engaged to characterize the swelling process as well as the structure and transport of interlayer species[18, 26, 27, 28, 29]. Botan *et al.*[17] applied grand canonical Monte Carlo (VT-MC) simulations to study the effect of water and CO_2 intercalation on Na-MMT swelling at prevailing (P, T) conditions of an underground formation. They considered basal d_{001}-spacings over the range of 12 to 17 Å that excluded important d_{001}-spacings corresponding to sub-1W hydration levels. In addition, we note that the VT-MC method needs precise calculation of chemical potentials for the binary CO_2-H_2O mixture which is quite challenging.

The goal of the present study is to characterize intercalation of pure carbon dioxide, pure water, and CO_2-H_2O mixtures into Na-MMT and Na-BEI at two (P, T) conditions, one relevant to the geological carbon storage via injection of scCO_2 and the other corresponding to exposure of clay to CO_2 in the gas phase. Na-MMT and Na-BEI have different localization of the negative charges in their mineral layers allowing us to study whether this is an important factor in CO_2 uptake. The simulations employed the Gibbs ensemble Monte Carlo (GEMC) method[50, 51] in which knowledge of chemical potentials is not required to equilibrate non-interacting systems representing different phases of interest. In addition, molecular dynamics simulations in the canonical ensemble were used to analyze the properties of equilibrium water-CO_2 mixtures in the interlayer region of clays.

4.2 COMPUTATIONAL DETAILS

4.2.1 Swelling thermodynamics

The thermodynamics of swelling of layered materials was outlined by Diestler *et al.*[40] and Bordarier *et al.*[10] As shown in those publications, the internal energy of a slit micropore can be expressed as:

$$\begin{aligned} dU =& TdS + \mu dN + \sigma_{xx} s_y s_z ds_x + \sigma_{yy} s_z s_x ds_y \\ &+ \sigma_{zz} s_x s_y ds_z + \tau_{zx} s_x s_y dl_x + \tau_{zy} s_x s_y dl_y. \end{aligned} \tag{4.1}$$

Where T, S, μ, N, σ_{ii}, τ_{ij} (i and j represent index notations) are, respectively, the temperature, entropy, chemical potential, number of molecules, and normal and shear stress terms. s_i and l_i are Cartesian components of the micropore defined in Figure 23.

Taking into account only the normal stress term in the z direction, the free energy, F, and isostress free energy , Φ, are defined as

$$F = U - TS - \mu N, \tag{4.2}$$

$$\Phi = F - \sigma_{zz} A\, s_z, \tag{4.3}$$

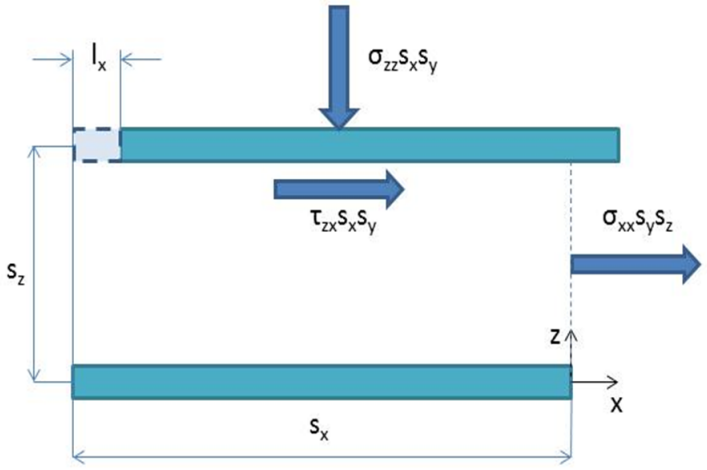

Figure 23: Slit micropore structure including position and force components.

where A is the surface area of the clay. Thus the difference in the swelling free energy for the wall separation Δs_z can be written as

$$\Delta\Phi = \Delta F - \sigma_{zz} A \, \Delta s_z, \tag{4.4}$$

By using equations 1 and 4, eliminating the x and y directions, and also considering the fact that μ and T are fixed at phase equilibrium, gives

$$\Delta\Phi = A \int_{s_z^0}^{s_z} (\sigma_{zz}(s'_z) - \sigma'_{zz}) ds'_z, \tag{4.5}$$

σ'_{zz} is the applied constant stress. By eliminating the isotropic part of stress (bulk pressure) from the stress terms, the equation can be converted into a pressure based equation

$$\Delta\Phi = -A \int_{s_z^0}^{s_z} (P_{zz}(s'_z) - P'_{zz}) ds'_z. \tag{4.6}$$

Where $P_{zz}(s'_z)$ and P'_{zz} are the slit normal (disjoining) and applied pressure, respectively. Equation 6 has been used by Smith[41] and by Botan *et al.*[17] to calculate the free energy of swelling as a function of the distance between layers.

4.2.2 Gibbs Monte Carlo Method

The use of the multiphase Gibbs approach to study equilibrium of multi-component systems is well-documented in literature[117, 118, 119, 120, 121, 122]. Lopes and Tildesley[117] evaluated the multicomponent GEMC approach to calculate two-phase, three-phase and four-phase equilibria. Kristof *et al.*[120] applied the approach to the three-component, CO_2-water-methanol system at high pressure conditions, obtaining good agreement between the results of their simulations and the experimental data.

The Gibbs ensemble Monte Carlo (GEMC) method[50, 51]uses separate boxes for each phase to calculate the phase equilibrium for a target (P,T) condition and to achieve equivalence of chemical potentials of interacting species. The algorithm employs three basic trial moves: particle displacement, particle exchange, and volume change. The displacement moves include a transitional or moves in a single box to satisfy temperature equilibrium. The exchange moves involve deletion of a particle in one box and its insertion into another box, to assure chemical potential equilibration. The volume moves expand or contract boxes to fulfill the pressure equilibration. Figure 24 shows the simulation setup with three boxes representing water, carbon dioxide, and clay phases.

4.2.3 Models and Force Fields

In this work, we used Na-MMT and Na-BEI clay structures with the stoichiometric chemical formulas $Na_{0.75}Mg_{0.75}Al_{3.25}(OH)_4(Si_4O_{10})_2$ and $Na_{0.75}Al_4(OH)_4(Al_{0.375}Si_{3.625}O_{10})_2$, respectively, where each clay TOT layer bears a negative charge -0.75 $|e|$ per unit cell that it is counterbalanced by interlayer Na^+ cations. The isomorphic substitutions in the TOT sheets were placed in such a way that they show a repeated pattern in the directions of a and b lattice vectors. The Al-O-Al linkage in the T sheets was avoided according to Loewenstains rule[123]. The clay structure is described by the Clayff force field[52], while the rigid SPC[54] and the rigid EPM2-based model of Cygan *et al.*[53] are employed for water and CO_2, respectively. The total potential energy can be written as:

$$E_{\text{Non-bond}} = E_{\text{VDW}} + E_{\text{Coul}} + E_{\text{Stretch}} + E_{\text{Bend}}, \tag{4.7}$$

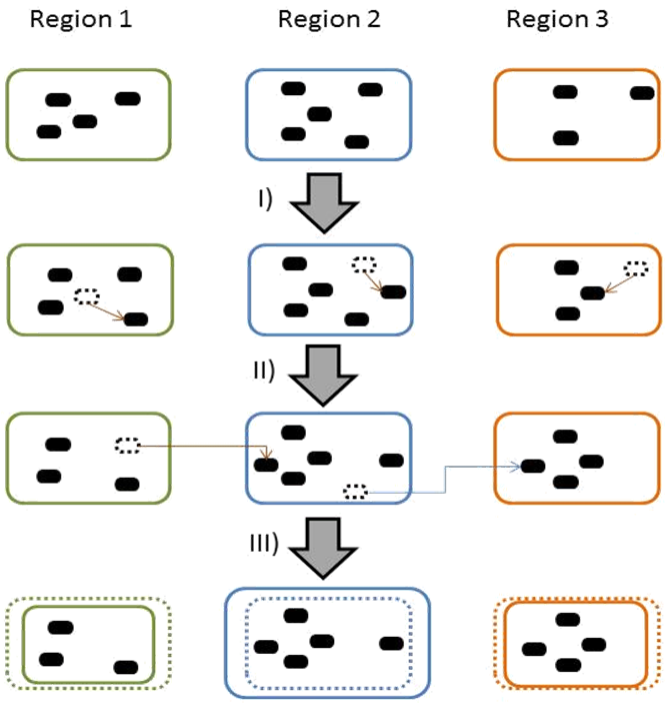

Figure 24: Illustration of Gibbs Monte Carlo method including three phases and three types of trial moves: i) displacement move, ii) exchange move, and iii) volume move.

with

$$E_{\text{VDW}} = 4\epsilon_{ij}[(\frac{\sigma_{ij}}{r_{ij}})^{12} - (\frac{\sigma_{ij}}{r_{ij}})^{6}], \quad E_{\text{Coul}} = \frac{q_i q_j e^2}{4\pi\epsilon_0 r_{ij}},$$

where atoms i and j are separated by a distance r_{ij}, and q_i is the charge on the atom i, e is the elementary charge of an electron, ϵ_0 is the vacuum permittivity, and ϵ_{ij} and σ_{ij} are the Lennard-Jones energy and distance parameters, respectively. The parameters for unlike atoms were calculated by using the Lorentz-Berthelot classical combining rules[3].

$$\sigma_{ij} = \frac{1}{2}(\sigma_i + \sigma_j), \quad \epsilon_{ij} = \sqrt{\epsilon_i \epsilon_j}. \tag{4.8}$$

The bond stretch ($E_{Stretch}$) potential term is employed only for the hydroxyl groups of the clay layer and is taken to be harmonic.

4.2.4 Simulation methodology

The NPT-GEMC method was applied to the ternary clay-H_2O-CO_2 and binary H_2O-CO_2 systems at two (P, T) conditions, (25 bar, 348.15 K and 125 bar, 348.15 K). The binary system was included to allow comparison of the results of our calculations with previous experimental[124, 125]and computational[17, 126] data, and also to provide a reference for the subsequent simulations of the ternary system.

In the MC simulations of the Na-MMT and Na-BEI phases, 4 × 3 × 2 (20.8 × 27.6 × 2h Å) supercells, requiring 18 counterions for neutrality, were employed. Calculations were carried out for d_{001}-spacings, h, ranging from 9.5 to 18 Å in steps of 0.5 Å to cover separations ranging from nearly dry clays to the interlayer distances corresponding to the 3W hydration state. For spacings ¿3W, the behavior of interlayer species becomes similar to that in the bulk[106, 6, 7, 107, 108, 8, 9, 10, 11]. The MC simulations were carried out for 2 × 10^5 equilibration cycles, followed by 1.5 × 10^5 production cycles. Each cycle consisted of 818 attempted moves, including volume exchange, configurational-bias interbox and intra-box molecule transfer, molecule regrowth, translational, and rotational moves[127, 128, 129]. Exploratory calculations were carried out to determine optimal probabilities of the various types of moves with the initial values being 0.5% volume exchange, 39.5% configurational-bias consisting of both inter- and intra-box moves, 10% regrowth, and 50% displacement, including translational and rotational moves. During the exploratory simulations, the probabilities of different moves and the components in the boxes were adjusted to ensure that the calculated chemical potentials of water and CO_2 in the various phases agreed to within the standard deviations. The positions of the atoms in the clay layers were held fixed, while the Na^+ ions were allowed to move within the interlayer space. The H_2O and CO_2 molecules were allowed to migrate between the "H_2O-rich", "CO_2-rich," and clay boxes. The cut-off radii for the non-bonded van der Waals interactions and for the real-space part of the Ewald summation of the electrostatics were chosen to be 9.5 Å, with switching distances starting from 6.5 Å in the Ewald summation. Standard deviations of all ensemble averages were determined by the standard block average technique[49]. The NPT-GEMC simulations were carried out using the Towhee simulation package[130].

In addition to the GEMC simulations described above, molecular dynamics simulations in the canonical ensemble (NVT-MD) were carried out to analyze various dynamical properties of the molecules in the clay phase. These simulations used a triclinic $8 \times 4 \times 4$ supercell with 5120 atoms constituting the mineral portion of the clay phase. The negative charge introduced by the isomorphic substitutions is compensated by 96 sodium ions residing in all interlayers. The carbon dioxide and water content (mole fractions) were taken to correspond to those obtained for the minimum free-energy structures from the Monte Carlo simulations. Equilibration runs of 1 ns were carried out, followed by 5 ns production runs with temperature controlled by a Nse-Hoover thermostat[80, 46] with a relaxation time of 2 ps. The cut-off radii for the non-bonded van der Waals interactions and for the Ewald summation of the electrostatics were chosen to be 9.5 Å, with the switching distance for the latter starting from 8.5 Å. Due to the use of cut-offs for the LJ interactions, long-range dispersion corrections for energy and pressure were applied. The leap-frog algorithm[43] was used to update positions every 1 fs. The MD simulations were carried out using the GROMACS package[77].

The radial distribution function (RDF) for species B around species A was calculated using:

$$G_{A-B}(r) = \frac{1}{4\pi\rho_B r^2}\frac{\Delta N_{A-B}}{\Delta r} \tag{4.9}$$

where ρ_B is the number density of species B, and ΔN_{A-B} is the average number of type B particles lying in the region r to $r + \Delta r$ from a type A particle. N_{A-B} is the coordination number $n(r)$ for B around A.

The diffusion coefficients of the interlayer species were calculated using the Einstein relation and equilibrated atomic trajectories from the NVT ensemble simulations with 1 ps sampling to evaluate the mean square displacement of the species of interest:

$$D = \frac{1}{6N_m t}\Big\langle \sum_{j=1}^{N_m}[r_j(t) - r_j(0)]^2 \Big\rangle, \tag{4.10}$$

where N_m is a number of a selected species and $r_j(t)$ is the center-of-mass position of the jth species at time t. The averages were over 5 ns trajectories. The diffusion coefficients were derived from the linear slope of the mean square displacement as a function of the simulation time. Different restart points in the analysis were taken to monitor convergence.

4.3 RESULTS AND DISCUSSION

4.3.1 Monte Carlo simulations

Table 5 compares the CO_2 mole fractions and the densities of the CO_2-rich and water-rich phases of the two-phase water-CO_2 and three-phase water-CO_2-clay systems. In the latter case, calculated results are reported for both Na-MMT and Na-BEI at d_{001} = 12.5 Å.

Table 5: Mole fractions of CO_2 (X) and densities (ρ) of H_2O and CO_2 in multiphase systems from previous studies and current work (T=348.15 K).

system	P [bar]	ρ_{H_2O} [g/cm^3]	ρ_{CO_2} [g/cm^3]	X_{H_2O}	X_{CO_2}	X^a_{clay}
H_2O-CO_2	25.3			0.0054	0.9818	
(Experiment)[125]	126.7				0.9915	
H_2O-CO_2	24.2	0.934(3)	0.039(1)	0.004(1)	0.982(1)	
(μVT-MC)[17]	122.4	0.940(5)	0.298(3)	0.014(1)	0.994(1)	
H_2O-CO_2	25	0.939(4)	0.040(1)	0.004(1)	0.980(4)	
(GEMC)	125	0.947(4)	0.314(7)	0.016(3)	0.994(2)	
MMT-H_2O-CO_2	25	0.937(5)	0.040(1)	0.004(1)	0.980(2)	0.014(2)
(GEMC)	125	0.947(5)	0.317(5)	0.016(3)	0.994(1)	0.056(2)
BEI-H_2O-CO_2	25	0.933(4)	0.040(1)	0.005(2)	0.983(2)	0.022(2)
(GEMC)	125	0.945(4)	0.321(5)	0.017(3)	0.993(1)	0.036(3)

[a]Clay is in the monolayer hydration state (d_{001}=12.5 Å).

For the CO_2-water system, the calculated mole fractions are in excellent agreement with the results of experimental measurements and with the results of grand canonical Monte Carlo simulations by Botan *et al.*[17]Similar mole fractions of CO_2 are found in the CO_2 and water phases of the three-phase systems as for the water-CO_2 two-phase system. Also, the densities calculated for the water-rich and CO_2-rich phases are nearly identical for the two-phase and three-phase systems. Most significantly, the concentration of carbon dioxide

in the clay phase coexisting at equilibrium with the CO_2-H_2O binary system greatly exceeds that in the bulk water-rich phase.

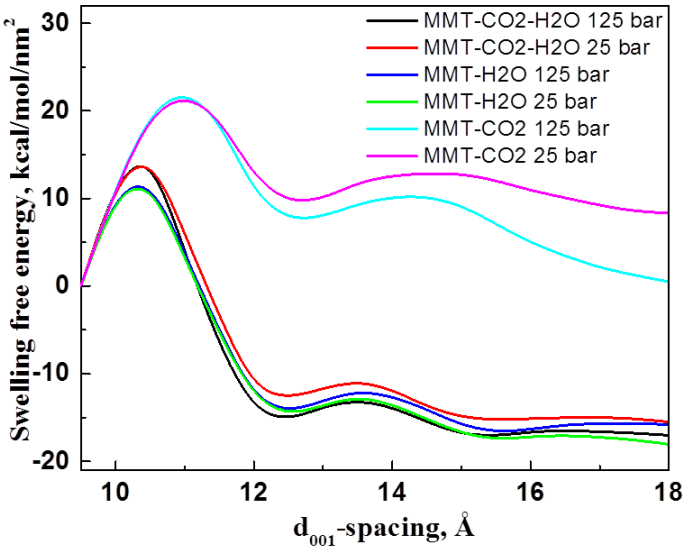

Figure 25: Calculated swelling free energy of Na-MMT as a function of the basal d_{001}-spacing for intercalation of pure CO_2, pure H_2O, and the H_2O-CO_2 mixture at P = 25 and 125 bar, T = 348.15 K.

The calculated swelling free energies as a function of the d_{001}-spacing for pure CO_2, pure H_2O and mixed H_2O-CO_2 intercalation into Na-MMT are depicted in Figure 25. Similar profiles for Na-BEI-H_2O and Na-BEI-CO_2-H_2O are given in Figure 26. The smallest (9.5 Å) d_{001}-spacing in the figures corresponds to dry clays in their 0W hydration state, characterized by the absence of intercalated molecules and provides a common origin for the swelling free energy curves. From the profiles, it is seen that in the absence of water, intercalation of CO_2 is highly unfavorable thermodynamically. For Na-MMT-CO_2 the minimum at 12.5 Å is about 10 kcal/mol/nm^2 less stable than that at 9.5 Å, i.e. the 0W hydration state. This result is consistent with experimental studies that show that carbon dioxide does not intercalate into MMTs in the absence of water[15, 14, 63]. Our calculations also show that, in the absence of water, intercalation of CO_2 into Na-BEI is even more unfavorable than into Na-MMT.

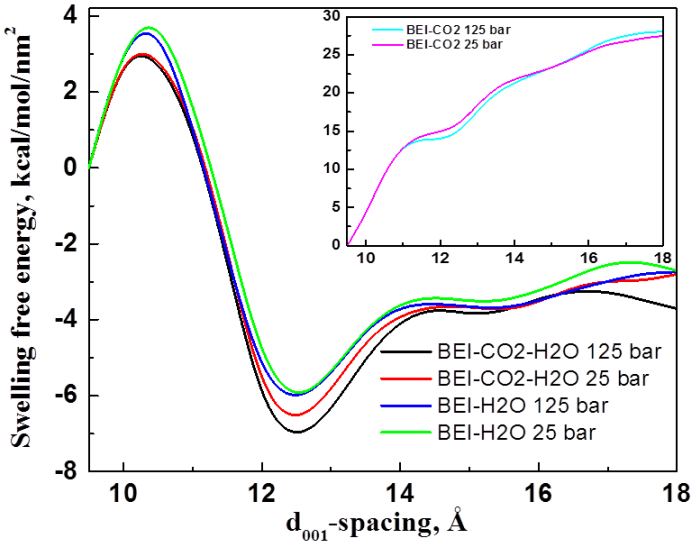

Figure 26: Calculated swelling free energy of Na-BEI as a function of the basal d_{001}-spacing for intercalation of pure CO_2 (insert), pure H_2O, and the H_2O-CO_2 mixture at P = 25 and 125 bar, T = 348.15 K.

For the intercalation of pure water into montmorillonite, two minima corresponding to 1W and 2W are identified with energies below that of 0W. The stability of the 1W and 2W states is a consequence of ion hydration and hydrogen bonding between the intercalated water molecules and the basal oxygen atoms[22]. The existence of two stable hydration states of Na-MMT is supported by previous studies[34, 35, 36, 37, 38]. The present calculations predict the 2W hydration state to be more stable than the 1W hydration state as found in earlier MC simulations[90, 91] For pure water in Na-MMT, the barrier for going from the 0W to the 1W state is calculated to be about 10 kcal/mol/nm^2 and is relatively insensitive to pressure. In contrast to Na-MMT-H_2O, Na-BEI-H_2O does not have a stable 2W state (Figure 26). The inability of Na-BEI-H_2O to swell beyond 1W has been documented in the literature[131], and factors responsible for this behavior will be discussed later in Section 3.2.

The swelling free energy curves for the clay systems with intercalated binary H_2O-CO_2 mixtures display trends similar to those for pure water (Figures 25 and 26). For both Na-MMT-CO_2-H_2O and Na-BEI-CO_2-H_2O, the free energy minima at d_{001}-spacings corresponding to the 1W hydration states are deeper and the barriers separating 0W and 1W are several kcal/mol/nm^2 lower than those for swelling induced by pure water. For Na-MMT-CO_2-H_2O the free energy barriers between the minima at 12.5 and 15 Å spacing is calculated to be only about 3 kcal/mol/nm^2 with the minimum at 15.5 Å being more stable. This indicates that in geological aquifers, both mono- and bilayer arrangements of CO_2-H_2O may occur in clays rich with MMT. Increasing the pressure is found to stabilize the free-energy minima near d_{001} = 12.5 Å (1W) of both clay systems.

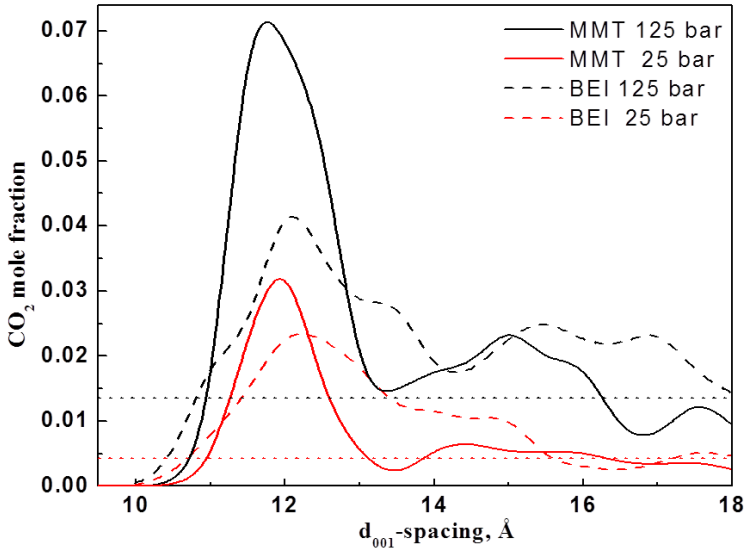

Figure 27: Equilibrium CO_2 mole fraction as a function of basal d_{001}-spacing for Na-MMT-CO_2-H_2O and Na-BEI-CO_2-H_2O at T= 348.15 K and P = 25 or 125 bar. The horizontal dotted lines represent the CO_2 mole fractions in the bulk H_2O-rich phase at P = 125 bar (black) and P = 25 bar (red), both at T=348.15 K.

The calculated mole fraction of CO_2 as a function of the basal d_{001}-spacing of Na-MMT and Na-BEI is reported in Figure 27. In both systems, there is a pronounced peak in the CO_2 mole fraction at a d_{001}-spacing corresponding to the 1W state and a second weaker

peak (or shoulder) at a distance corresponding to 2W. Experimental studies of Na- and Ca-MMT[15, 63, 16] have shown that the maximum expansion of the interlayer due to CO_2 exposure occurs at the sub 1W hydration state. Increasing the pressure causes an elevation of the CO_2 concentration in the interlayer region, with the increase being greater for Na-MMT than for Na-BEI. For both Na-MMT-CO_2-H_2O and Na-BEI-CO_2-H_2O the concentration of CO_2 in the interlayer region greatly exceeds that in the bulk water-rich phase. For Na-MMT-CO_2-H_2O, the calculated mole fractions of CO_2 in the interlayer region obtained in the present study in fairly good agreement with those reported by Botan *et al.*[17], although the CO_2 concentrations predicted in this work are lower. The different concentrations may be the result of the different force fields used in the two theoretical studies.

4.3.2 Molecular dynamics simulations

The Na-MMT-CO_2-H_2O and Na-BEI-CO_2-H_2O systems at d_{001}-spacing of 12.5 Å (1W) and 15.5 Å (2W) equilibrated in the GEMC simulations were further characterized by molecular dynamics using the NVT ensemble. In particular, the MD simulations were used to calculate the structural and transport properties of the interlayer species. The Na-BEI-CO_2-H_2O system at d_{001} = 15.5 Å does not correspond to a free energy minimum and is considered primarily for comparison with Na-MMT-CO_2-H_2O at the same d_{001}-spacing.

I) Structural details of the interlayer species

Figure 28 reports for Na-MMT and Na-BEI the calculated atomic density profiles for water oxygen (Ow), carbon (C_{CO_2}), and sodium ions (Na^+) at d_{001}-spacings equal to 12.5 and 15.5 Å. The profiles were computed along the z axis (perpendicular to the clay surface) and averaged over the interlayer region of the simulation box using a 3 ns production time frame. For each species of interest, the density profiles computed for P = 25 and 125 bars are close agreement, and only the P = 125 bar data are shown in the figure. The O_w and Na^+ density profiles for pure water are qualitatively similar to those for the H_2O-CO_2 mixtures and, therefore, are not reported. For both Na-MMT and Na-BEI, the density profiles for O_w and C_{CO_2} display a single peak in the case of d_{001} = 12.5 Å and two peaks in the case of

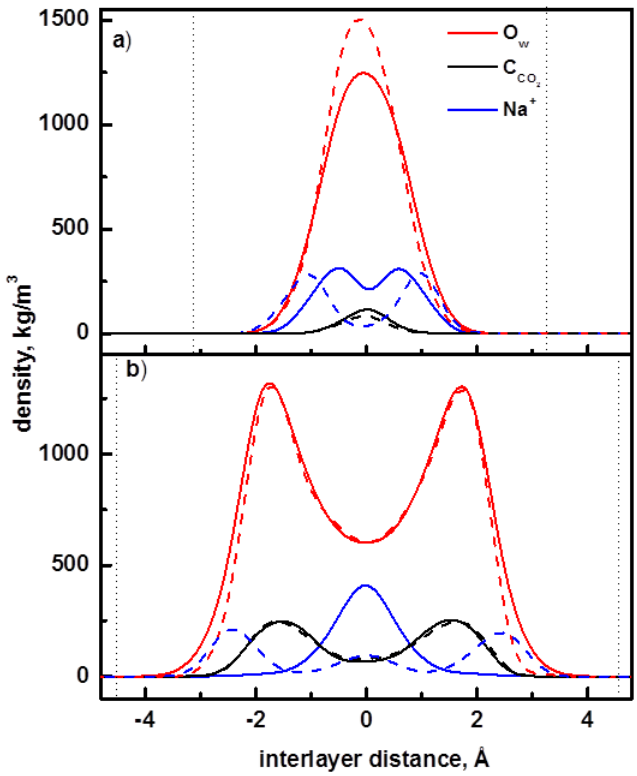

Figure 28: Density profiles of O_w, C_{CO_2}, and Na^+ along the interlayer distance perpendicular to the internal surfaces of Na-MMT-CO_2-H_2O (solid lines) and Na-BEI-CO_2-H_2O (dashed lines). The distributions of the intercalated species are reported for d_{001}-spacings of a) 12.5 Å and b) 15.5 Å For b) the densities of C_{CO_2} are magnified by a factor of 10 for clarity. Vertical black dotted lines designate the planes of the basal oxygen atoms.

d_{001} = 15.5 Å. For Na-MMT-CO_2-H_2O the compositions of carbon dioxide and water in the monolayer and the bilayer structures are $\sim$ 4.1 H_2O - 0.3 CO_2 and $\sim$ 8.9 H_2O - 0.2 CO_2 per unit cell, respectively. These numbers are in reasonable agreement with the results of grand canonical MC simulations of Botan *et al.*[17] (monolayer: 3.7 H_2O - 0.6 CO_2 and bilayer: 8.6 H_2O - 0.4 CO_2 per unit cell). For Na-BEI-CO_2-H_2O our simulations give $\sim$ 4.4 H_2O - 0.2 CO_2 and $\sim$ 8.6 H_2O - 0.2 CO_2 per unit cell for the monolayer and bilayer arrangement, respectively.

In an earlier paper[18], we reported the d_{001}-spacing of Na-MMT as a function of the number of water molecules at fixed numbers of CO_2 molecules per unit cell in order to estimate the effect of CO_2 intercalation on the interlayer distance of Na-MMT-CO_2-H_2O. It was deduced that the addition of 0.2-0.3 CO_2 molecules per unit cell led to an expansion of the d_{001}-spacing by $\sim$ 0.5-0.6 Å. In experimental studies performed at elevated (P,T) conditions the maximum expansion of Na-MMT upon interaction with dry $scCO_2$ was found at an initial d_{001}-spacing below 11.5 Å, which corresponds to a sub-1W state of hydrated Na-montmorillonite and was capped at a d_{001}-spacing equal to about 12.5 Å suggesting that expansion due to interaction with $scCO_2$ can be as much as $\sim$ 1 Å[15, 58]. Further, Loring *et al.*[16] estimated that the maximum CO_2 absorption in the interlayer of Na-exchanged MMT occurs at water concentrations close to the transition between 0W and 1W hydration states. Thus, the values of the equilibrium concentrations of intercalated CO_2 predicted in this work appear to be somewhat underestimated.

In contrast to the density profiles of O_w and C_{CO_2}, the density profiles of Na^+ are quite different for Na-MMT-CO_2-H_2O and Na-BEI-CO_2-H_2O. Since the major difference in these two phyllosilicates is the location of the negative charge in the mineral layers, we conclude that this is an important factor determining the sodium ion distributions. For the $d_{001} = 12.5$ Å case, the Na^+ density distribution is bimodal for both Na-MMT and Na-BEI. However, for Na-BEI, the positions of the peaks are shifted closer to the basal surfaces as a result of preferential coordination of sodium cations at the middle of the hexagonal rings formed by the silicon-oxygen polyhedra with isomorphic substitutions[18]. Effectively, the peak shift reflects a change from predominantly Na^+ outer-sphere coordination with water in case of Na-MMT to inner-sphere adsorption at the internal clay surfaces for Na-BEI where basal oxygens participate in the first solvation shell of sodium ions. Intercalation of carbon dioxide disrupts the water network[113] and also causes the Na^+ ions to be displaced toward the clay surfaces[18].

In the 2W state of the Na-MMT-CO_2-H_2O system, the Na^+ distribution peaks at the middle of interlayer. However, for Na-BEI-CO_2-H_2O, it is split into three peaks, with two more pronounced peaks corresponding to sodium ions adsorbed at the surfaces and a weaker central peak corresponding to Na^+ ions more fully solvated by water molecules. The surface-

adsorbed Na^+ ions have in their first solvation shell both basal oxygens of the ditrigonal rings and interlayer water molecules. Additional information on the solvation structure of the ions can be gained by examining the radial distribution functions (RDFs) for atomic pairs of interest. Figure 29 reports the RDFs for the sodium ion water oxygen pair computed for Na-MMT-CO_2-H_2O and Na-BEI-CO_2-H_2O at monolayer and bilayer arrangement and P = 125 bar. Figure 30 depicts the corresponding RDFs for the sodium ion basal oxygen pair. Additionally, cumulative number RDFs, i.e. the average number of atoms within a distance, r, were calculated.

For the monolayer arrangements of Na-MMT-CO_2-H_2O of Na-BEI-CO_2-H_2O, the Na^+ ions are hydrated on average by 4.0 and 3.6 water molecules, respectively. On the other hand, the average number of basal O atoms directly bonded to the Na^+ ions is 1.2 for Na-MMT, but 1.9 for Na-BEI. Thus, the total Na^+ coordination numbers in the monolayer case is about 5.3 in both cases. For the bilayer (d_{001}=15.5 Å) of Na-MMT-CO_2-H_2O the Na^+ ions tend to be coordinated by water molecules alone, achieving on average a coordination number of 5.5. On the other hand, for Na-BEI-CO_2-H_2O in the 2W state, the average Na^+ coordination number, 5.7, derives from 4.3 of water oxygens and 1.4 of basal oxygens (Figure 30). A simulation of sodium ions in bulk water using the same (P,T) conditions and force fields as used in the clay simulations gives an average Na^+ coordination number 5.6 for the first hydration shell, essentially the same as that calculated for Na^+ in the bilayer in Na-MMT. Experimental studies of Na^+ in bulk water lead to Na^+ coordination numbers in the range 4.4-5.4[132, 133] consistent with the results of CPMD simulations[134] which give an average coordination number of 4.9 at 300K. Thus, it appears that our simulations tend to slightly overestimate the average number of water molecules coordinating the Na^+ ions. This probably reflects a deficiency of the force field used in the simulations.

In Na-BEI the strong electrostatic interaction between ions and the surfaces makes it more favorable for the cations to be adsorbed at a surface than to be located at the middle of the interlayer. In Na-MMT, in which the negative charges are screened by the T sheets, the Na^+ ions are more stable near the center of the bilayer where they are essentially fully hydrated. Suter *et al.*[92] explored the thermodynamics of Li^+, Na^+ and K^+-montmorillonote and beidellite using ab initio molecular dynamics. These authors found that smectites with

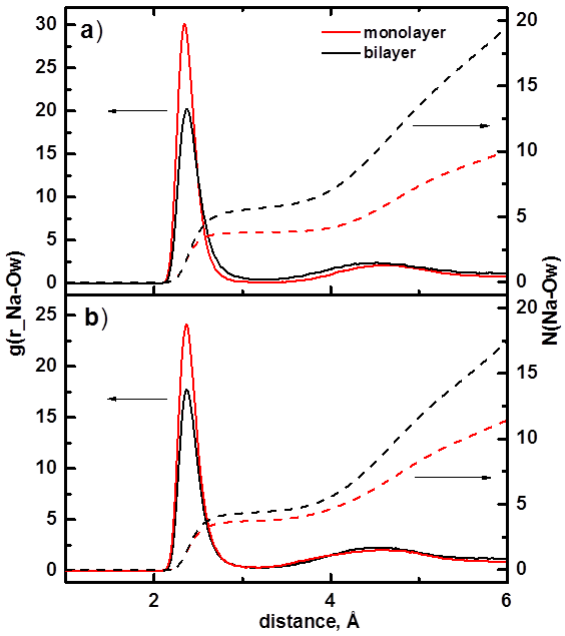

Figure 29: Radial distribution functions (solid curves) and cumulative number RDFs (dashed curves) of the Na^+-O_w pair for a) Na-MMT-CO_2-H_2O and b) Na-BEI-CO_2-H_2O at P = 125 bar and T=348.15 K. Dotted lines designate the cumulative number RDF, i.e. the average number of particles within a Na^+-O_w distance.

the free energy minimum in the middle of the interlayer for bilayer swell to the 2W hydration state with the ions forming a full hydration sphere. In Na-beidellite the position of the lowest energy region remains unchanged from monolayer to bilayer indicating that swelling would stop at monolayer. At that position, basal oxygens form a part of sodium hydration sphere. Thus, the interplay between the hydration of counter-balancing ions and the attraction to the basal surface determines the swelling behavior of smectites. Localization of charge in the O clay sheets supports swelling to 2W (and higher) while localization of the negative charge in the T sheets favors 1W (Figure 25 and 26).

We now consider the effects of layer charge localization and the interlayer ions on the CO_2-H_2O distributions. Figure 31 shows the calculated RDFs of carbon-water oxygen (C-Ow) and CO_2 oxygen water hydrogen (O_{CO_2}-H_W) pairs for Na-MMT-CO_2-H_2O for both monolayer

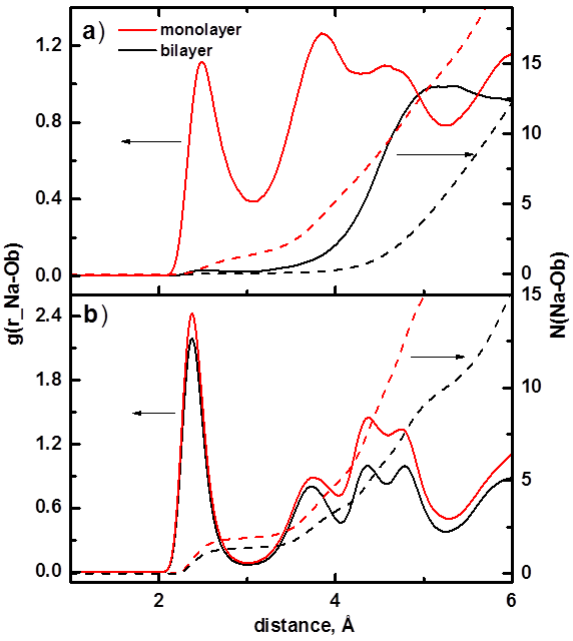

Figure 30: Radial distribution functions (solid curves) and cumulative number RDFs (dashed curves) of the Na^+-O_b pair for a) Na-MMT-CO_2-H_2O b) Na-BEI-CO_2-H_2O at P = 125 bar and T=348.15 K . the cumulative number RDF, i.e. the average number of particles within a Na^+-O_b distance.

and bilayer conditions at P = 125 bar. The corresponding RDFs for Na-BEI-CO_2-H_2O (monolayer and bilayer) display qualitatively similar shapes and are not shown here. The C-O_w RDF displays only a weak shoulder near 3.1 Å, corresponding to coordination of water to carbon of CO_2. The shoulder is more pronounced in the bilayer than in the monolayer case, consistent with a larger number of water oxygens surrounding CO_2 molecules in the former. However, the RDF of carbon basal oxygens indicates that the coordination number of basal oxygens is larger for the monolayer than for the bilayer, so on average the CO_2 molecules are surrounded by similar numbers of oxygens atoms in the monolayer and bilayer. This result is consistent with a prior analysis of the nearest-neighbor coordination numbers for CO_2 carbon atoms in hydrated Na-MMT[17]. For the monolayer arrangement of Na-MMT-H_2O-CO_2, the O_{CO_2}-H_W RDF displays a well-defined shoulder near 2.3 Å, consistent with

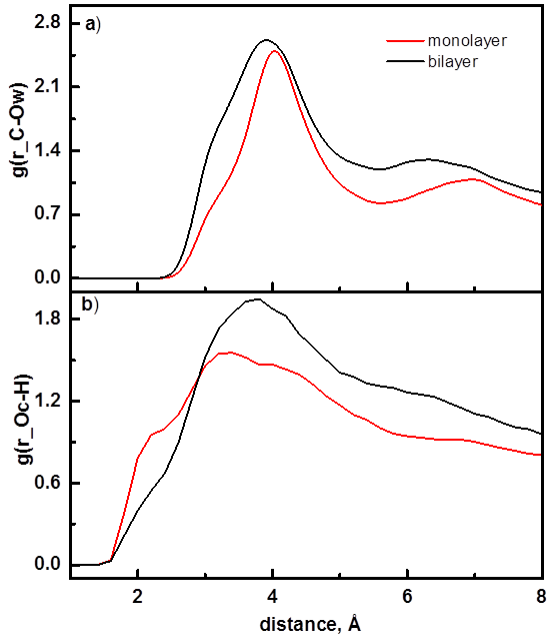

Figure 31: Radial distribution functions for a) carbon water oxygen (water) and b) CO_2 oxygen water hydrogen in Na-MMT-CO_2-H_2O at P = 125 bar and T = 348.15 K.

H-bond formation between H_2O and CO_2. This shoulder is much less pronounced for the bilayer. These results are consistent with the calculated average lifetimes[134] of the H bonds between the O_{CO_2} atoms and the hydrogen atoms of the water molecules. The values are 1.3 and 0.2 ps (P = 125 bar, Na-MMT-CO_2-H_2O) for the monolayer and the bilayer, respectively, implying stronger H-bonding in the former case. For Na-BEI-CO_2-H_2O the corresponding computed lifetimes are 2.2 and 0.4 ps for 1W and 2W, respectively. The different lifetimes in the two clays can be related to details of the CO_2 distributions in the interlayers.

Figure 32 depicts number density maps for carbon dioxide molecules residing in a selected monolayer or bilayer of Na-MMT-CO_2-H_2O, in a monolayer of Na-BEI-CO_2-H_2O, and in pyrophyllite at a CO_2-H_2O composition corresponding to that of the monolayer of Na-MMT-CO_2-H_2O. The maps were obtained by scanning the interlayer space to compute density distributions in planes parallel to the clay surfaces with a step size of 0.1 Å. Then, the distributions were projected onto the xy plane and averaged for 10 ns of simulation time.

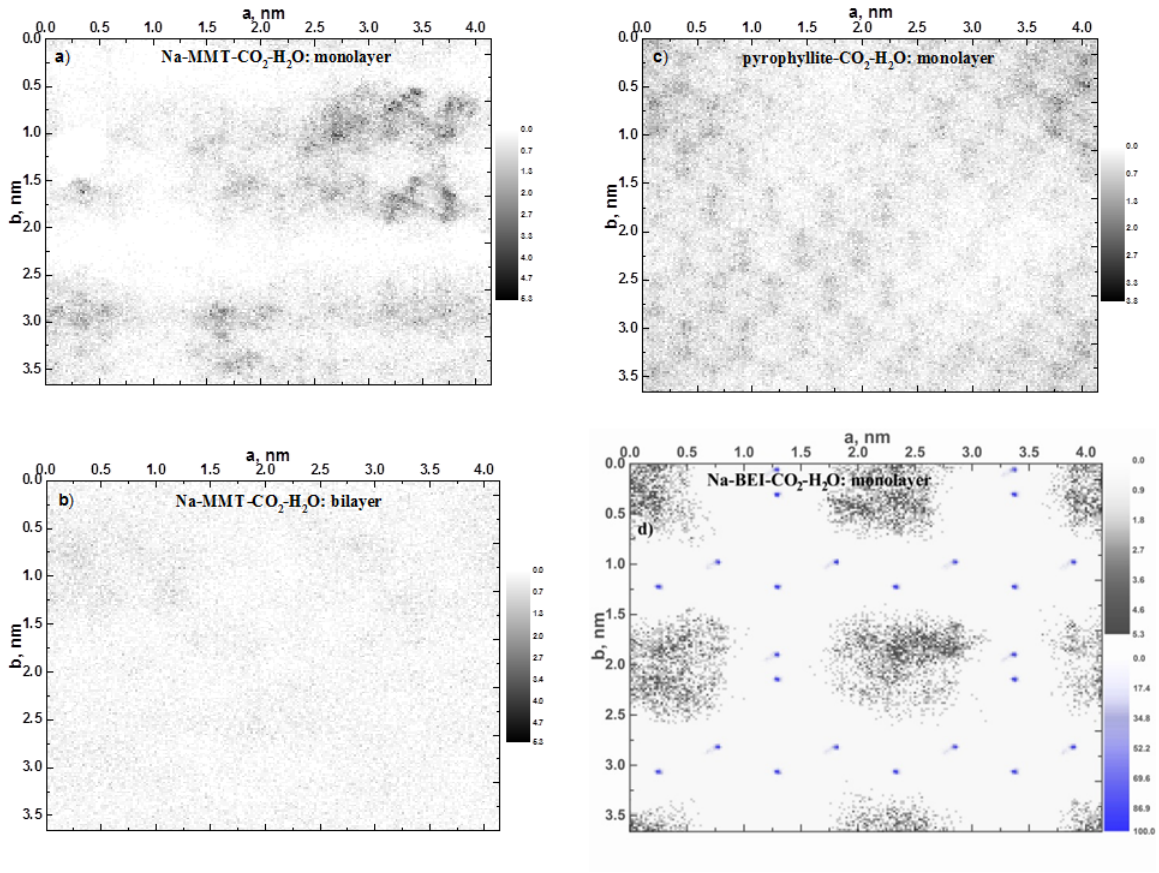

Figure 32: Density maps (number of molecules / nm3) showing carbon dioxide molecule distributions at P = 125 bar and T=348.15 K in the interlayer at d_{001}-spacing a) 12.5 Å for Na-MMT-CO_2-H_2O, b) 15.5 Å for Na-MMT-CO_2-H_2O, c) 12.5 Å for pyrophyllite, and d) 12.5 Å for Na-BEI-CO_2-H_2O with positions of Al substitutions in the adjacent tetrahedral layers given in blue. Results obtained by averaging over 10 ns of simulation time.

Pyrophyllite is a 2:1 dioctahedral phyllosilicate without charges on the mineral layers and, hence, no interlayer cations. The density map for pyrophyllite is included to provide additional insight into the effect of interlayer ions on the CO_2 distribution. For Na-MMT-CO_2-H_2O the distribution of CO_2 molecules is distinctly different in the monolayer and bilayer arrangements.

For the monolayer of Na-MMT-CO_2-H_2O, the density map reveals that the CO_2 molecules are non-uniformly distributed with respect to their xy coordinates and tend to conglomerate as represented by the dark regions in Figure 32. Analysis of distributions computed over various time frames shows that the clustered carbon dioxide molecules move over time in the interlayer. Migrating CO_2 clusters persist even in simulations carried out as long as for 50 ns. However, it is expected that averaged over sufficiently long times, the structure would smear out. The formation of CO_2 conglomerates in clay monolayers is supported by other studies that speculated that CO_2 enters the sub-1W interlayer "by pushing the structural units apart"[13]. Young and Smith[20] reported that for Sr-MMT under sub 1W conditions the water molecule aggregates around the cations leaving voids. The voids can be filled by carbon dioxide in a "prop-and-fill" mechanism[20] in which the clay is propped open by hydrated cations making possible entrance of CO_2. In this work, it is found that the instantaneous spatial distribution of the clustered CO_2 molecules in Na-MMT is not correlated with the positions of the substitutions in the O sheets. However, it should be kept in mind that we have used a periodic rather than random distribution of substitution sites in the T or O layers, and that the distribution of CO_2 conglomerates could depend on the distribution of substitution sites. Earlier Monte Carlo simulations of cation distributions in the octahedral sheets of phyllosilicates suggest a tendency for Mg cations not to cluster in the Al/Mg systems[135] whereas in some montmorillonite samples Mg^{2+} were observed to form clusters[136]. Palin *et al.*[137] using Monte Carlo simulations show short-range Al-Si ordering across the tetrahedral sheets of muscovite that depends on the Al:Si ratio and temperature. So, the ordering calculated in T sheets of muscovite supports the ordered placement of isomorphic substitutions in T sheets adopted in this work. In a previous study, we also found conglomerate formation of CO_2 for both Na- and Ca-MMT[53]. Thus, this behavior is not limited to clays with Na^+ ions.

We hypothesize that the interlayer ions facilitate CO_2 conglomeration in the monolayer of the clay systems by "tying" up water molecules. To investigate this possibility, a simulation was conducted on pyrophyllite using the equilibrium CO_2-H_2O compositions computed for monolayer of Na-MMT-CO_2-H_2O at P = 125 bar. The resulting density distribution map, depicted in Figure 32, shows that CO_2 develops a periodic pattern reminiscent of ditrigonal

rings of the basal surfaces. Thus, in the absence of interlayer ions, the tendency of CO_2 to conglomerate is suppressed, and its distribution is determined by the basal atoms of adjacent internal clay surfaces. In a previous paper devoted to turbostratic smectites, we showed that a rotational shift of one adjacent clay layer relative to the other creates Moir patterns consisting of basal atoms[53]. Those patterns play a role in determining the distribution of interlayer species including carbon dioxide.

The distribution of CO_2 in the monolayer of Na-BEI-CO_2-H_2O (Figure 32) is particularly striking. The CO_2 molecules are clustered in the regions defined by the positions of the isomorphic substitutions in the T sheets (depicted by blue dots in Figure 32). CO_2 clearly tends to locate in the areas away from the charge originated from the substitutions, while the interlayer space near substitutions is occupied by water and hydrated cations. In the bilayer, the CO_2 density profile displays two-peaks (Figure 28) implying that the CO_2 molecules are exposed to the internal surfaces at the comparable distances as in monolayer. Indeed, the corresponding distribution map (not shown) also reveals localized density regions controlled by the substitution positions, however, the structure is more smeared than in the monolayer Obviously, in natural samples the substitution pattern could be irregular, and the CO_2 distribution would be more complex than shown in Figure 32. Nonetheless, the location of the layer charges in Na-BEI is a key factor in determining the CO_2 distribution in monolayer and bilayer. In Na-BEI-CO_2-H_2O the CO_2 motion is significantly restricted compared to the more mobile CO_2 conglomerates in Na-MMT-CO_2-H_2O. To quantify the transport properties of the interlayer species, diffusion coefficients were calculated and analyzed for both clays.

II) Diffusion of the interlayer species

Table 6 reports the computed diffusion coefficients for the interlayer species in Na-MMT, Na-BEI, and bulk phases obtained in this work and in other studies[27, 138, 139, 140, 11] as well as from experimental measurements on similar systems. Both 3D and 2D (xy) values of the diffusion constants are given. In general, the diffusion constants for lateral motion of interlayer species are about 25-35% greater than those computed for 3D motion. As expected, the diffusion coefficients for CO_2, H_2O, and sodium ions increase in going from monolayer to bilayer arrangements, with the bilayer values being 5-10 times larger than the corresponding

monolayer values. For Na-MMT-CO_2-H_2O the diffusion coefficients computed in this work are systematically higher than those calculated by Botan *et al.*[17] (Table 6). This is attributed to differences in the force fields used in the two works. Nevertheless, the calculated values of the diffusion constants of water from the two studies are close to the experimental result obtained using QENS spectroscopy. Also, our calculated diffusion constant for lateral motion of H_2O in Na-MMT is comparable to that measured for water in the interlayer region of Na-hectorite[138, 139] (a trioctahedral smectite with isomorphous substitution in the octahedral sheet that displays swelling properties similar to those of MMT)[140]. The calculated diffusion coefficient of water in the bulk phase at is 8.4 $\times$ 10^{-5} cm^2/s, in reasonable agreement with the experimental value of 5.97(6) $\times$ 10^{-5} cm^2/s[141] at T = 347 K. More importantly, the calculated diffusion constant for water in the bulk is 9-28 times greater than that for water in the monolayer and about 2-6 times larger than that of the bilayer for the two clays[17].

For both the monolayer and bilayer cases, the diffusion constant for water in Na-BEI-CO_2-H_2O is about two times smaller than for water in Na-MMT-CO_2-H_2O. Similarly, the measured diffusion constant for CO_2 in bulk water, 5.40 0.10 $\times$ 10^{-5} cm^2/s (T = 348 K)[142], is about 1.5-3.0 times larger than for lateral motion of CO_2 in the clay bilayer and about an order of magnitude larger than that for lateral diffusion of CO_2 in the monolayer of Na-MMT-CO_2-H_2O. Due to the constrained motion of CO_2 in the monolayer of Na-BEI-CO_2-H_2O, the diffusion coefficient of CO_2 in that system is much smaller (by 5-10 times) than for Na-MMT-CO_2-H_2O.

Our calculated value of the Na^+ diffusion constant in bulk water, 2.7 $\times$ 10^{-7} cm^2/s, in reasonable agreement with the experimental value of 3.5 $\times$ 10^{-5} cm^2/s[143]. It is also about twice as large as that for diffusion in Na^+ in the bilayer and more than an order of magnitude larger than that for diffusion of Na^+ in the monolayer of Na-MMT-CO_2-H_2O. Predictably, Na-BEI-CO_2-H_2O, for which the Na^+ ions tend to be adsorbed at the internal surfaces, has much smaller Na^+ diffusion constants than for Na-MMT-CO_2-H_2O in both the monolayer and bilayer cases. Kozaki *et al.*[144] reported a diffusion constant of 1.8 $\times$ 10^{-6} cm^2/s for interlayer sodium ions in the 2W hydration state of MMT at 323 K and 0.1-0.3 M concentrations of NaCl. Even though that value is in good agreement with that calculated

Table 6: Diffusion coefficients (x 10^{-5} cm^2/s) of water, carbon dioxide molecules, and Na^+ cations in the interlayer spaces of Na-MMT and Na-BEI for the equilibrium CO_2-H_2O compositions corresponding to d_{001}-spacing of 12.5 and 15.5 Å at T=347.15 K.

system	P	D					
	[bar]	(H_2O)	$(H_2O)^a_{xy}$	(CO_2)	$(CO_2)^a_{xy}$	(Na^+)	$(Na^+)^a_{xy}$
Monolayer							
BEI-CO_2-H_2O	125	0.23(1)	0.32(2)	0.03(0)	0.04(0)	0.01(0)	0.01(0)
	25	0.33(3)	0.49(3)	0.05(1)	0.08(1)	0.01(0)	0.02(0)
MMT-CO_2-H_2O	125	0.41(3)	0.62(4)	0.28(3)	0.43(1)	0.11(1)	0.16(2)
	25	0.61(2)	0.91(4)	0.24(3)	0.35(4)	0.20(1)	0.27(1)
Bulk water	125	8.4(7)		10.3(8)		2.7(5)	
MMT-CO_2-H_2O[17]	125		0.32(2)		0.17(2)		0.13(2)
	25		0.51(2)		0.24(4)		0.19(2)
Hectorite-H_2O[138]	1		1.0(1)				0.13(2)[96]
(Expt., T=347K)							
Bilayer							
BEI-CO_2-H_2O	125	0.98(4)	1.48(4)	0.93(5)	1.50(6)	0.10(2)	0.14(2)
	25	1.39(5)	2.04(7)	1.29(4)	2.05(7)	0.11(3)	0.17(4)
MMT-CO_2-H_2O	125	2.39(3)	3.58(6)	1.55(6)	2.50(1)	1.12(2)	1.73(2)
	25	2.42(4)	3.63(7)	1.64(8)	2.81(5)	1.38(2)	1.92(3)
MMT-CO_2-H_2O[17]	125		3.2(1)		1.5(1)		1.4(1)
	25		3.5(1)		1.6(2)		1.3(1)
Hectorite-H_2O[139]	1		2.2(2)				
(Expt., T=347K)							

$^a_{xy}$ denotes the lateral diffusion coefficient of the motion parallel to clay surfaces.

in the present study for the 2W state of Na-MMT, direct comparison between calculated and measured ionic mobilities of smectite samples should be done with caution since the

experimental values can include substantial contributions from ions residing in pores and at external surfaces depending on experimental conditions and ionic strength[144].

4.4 SUMMARY

Molecular dynamics and multiphase Gibbs ensemble Monte Carlo simulations were carried out to study adsorption of carbon dioxide and water in the interlayer regions of Na-MMT and Na-BEI. The free energy calculations indicate that intercalation of pure CO_2 into the clay interlayers is not favorable, while pure H_2O adsorption may occur naturally at the (P, T) conditions relevant to carbon sequestration in deep geological formations. For Na-MMT-CO_2-H_2O the free energy of swelling shows two minima corresponding to monolayer and bilayer arrangements of the interlayer species, whereas for Na-BEI-CO_2-H_2O the expansion of the interlayer is limited to monolayer for both pure water and CO_2-water mixtures. This is a consequence of the strong interaction between the cations and the negatively charged clay layers.

The calculations predict the carbon dioxide concentrations in the interlayer of both clays greatly exceeding the solubility of CO_2 in bulk water at the (P, T) conditions of interest. In agreement with experiment, the maximum carbon dioxide adsorption occurs at the d_{001}-spacing range (11.5-12.5 Å) corresponding to the 1W hydration state. For both clays, CO_2 can fill the available space in sub-1W interlayer arrangements, resulting in expansion of d_{001} to 12.5 Å. The presence of interlayer cations leads to CO_2 conglomeration in the monolayer of Na-MMT-CO_2-H_2O. For Na-BEI-CO_2-H_2O, both the cations and the negative charges in the tetrahedral layers significantly impact the distributions of water and carbon dioxide molecules. CO_2 is driven away from the positions of isomorphic substitutions, whereas hydrated cations molecules are located close to Al^{3+}/Si^{4+} substitution sites. The results showed that in smectites, hydrated cations and substitutions into tetrahedral sheets promote segregation of water and CO_2 in the interlayers and affects the ability of the clay minerals to retain carbon dioxide.

Not surprisingly, in the monolayer region of smectite clays, the mobilities of all interlayer species: water, CO_2, and Na^+ are significantly retarded compared to the bulk phase. The corresponding diffusion constants in the bilayer regions are significantly less reduced compared to their values in bulk water. The most prominent reduction in mobility is found for CO_2 and Na^+ in Na-BEI-CO_2-H_2O.

The simulations predict that at equilibrium with a CO_2-bearing aquifer, carbon dioxide intercalation into hydrated clay phases is accompanied by expansion of the interlayer distance causing increase of clay volume, which, in turn, influences the porosity and permeability of formations enriched in expandable clay minerals. The greater solubility of CO_2 in the interlayer region of smectites than in bulk water suggests that smectite minerals are good candidates for carbon dioxide storage.

4.5 ACKNOWLEDGMENT

This technical effort was performed in support of the National Energy Technology Laboratory's ongoing research in Subtask 4000.4.641.061.002.254 under the RES contract $DE-FE0004000$. The simulations were carried out on NETL's High-Performance Computer for Energy and the Environment (HPCEE) and on computers in the University of Pittsburgh's Center for Simulation and Modeling.

This chapter is taken from a manuscript: *"Multiphase Monte Carlo and Molecular Dynamics Simulations of Water and CO_2 Intercalation in Montmorillonite and Beidellite"* which has already been submitted and has been performed in collaboration with K. Jordan, G. Guthrie and E. Myshakin.

5.0 CONCLUSION

In summary, the objective of this study was to investigate the behavioral response of smectites to the intercalation of CO_2 and H_2O molecules by employing classical atomistic simulations, and the work was divided into five chapters. In chapter 1, the motivation, introduction and outline of the work were described. In chapter 2, basics of classical molecular dynamics and Monte Carlo methods were introduced, different ensembles were defined and the force fields, employed for our simulations, were reviewed. The objective of chapter 3 was to carry out classical modeling to probe the effect of rotational disordering on the energetic and structural properties of Na-MMT and Ca-MMT clay minerals. Next, in chapter 4, we employed clay disjoining pressure and free energy computations to investigate the water and carbon dioxide adsorption in Na-MMT and Na-BEI by means of molecular dynamics and Monte Carlo techniques. Finally, in chapter 5, the significant results and contributions are outlined, and ongoing and future research is discussed.

5.1 FINDINGS AND CONTRIBUTIONS

5.1.1 Effect of Rotational Disordering on clay Energetic and Structuractural Parameters

We studied the role of rotational disordering, a naturally occurring defect in smectite, by two different approaches: position constraining and enforced rotation methods. The former was employed to investigate the stationary disordering, and the simulations were carried for the clay layers at constant rotational degrees (θ = 0, 3, 6, 9 and 12 °), while the latter was

used to deal with continuous rotational disordering evolving with time; therefore, clay layers with a constant angular rotation around the center of mass of the clay were simulated by using fixed velocities($\omega = 0.01$ and 0.001 °/ps).

We found that rotational disordering influences both internal energy and basal distance. The hydrated clay and the clay with intercalated water and CO_2 molecules showed resistance to rotation by increasing the potential energy, and expanding the basal spacing (0.1-0.2 Å), while the disordering was energetically favorable in the dry clay and led to the decrease of internal energy and interlayer spacing (about 0.1 Å). Moreover, the rotation of basal surfaces with respect to each other generates a configurational Moiré pattern. By investigating the density map of different species, we observed that the distribution of interlayer molecules (water and CO_2) and counterions depends on the Moiré pattern.

5.1.2 Role of Interlayer Cation Type on clay Parameters and disordering process

Counterions in the interlayer space can be from numerous metallic elements (such as Li^+, Na^+, K^+, Ca^{2+} and Mg^{2+}), including different charges and sizes, resulting in different physical and geometrical properties of the clay. To probe the effect of counterion type on the clay properties, molecular dynamics simulations were carried out to calculate the equilibrium d_{001}-spacing values of dry Na-MMT, Ca-MMT and K-MMT structures. These values, consistent with the previous DFT results of this group[32] and experimental data[83, 84], illustrated that K-MMT, with the largest atomic radius of the counterion, involves the largest lattice parameter in the z direction; therefore, by using this result and previous ones[83, 84, 32] there is a direct relation between the cation size and the interlayer spacing. In the second step, we simulated rotationally disordered (turbostratic) structures of the three montmorillointes (consisting of different interlayer cations) and also pyrophyllite (with no counterion inclusion). The simulations described that, due to rotation of layers, K-MMT and Ca-MMT experience larger fluctuations in potential energy and interlayer spacing than Na-MMT, thus suggesting that larger sizes and charges of the cations lead to larger fluctuations.

Next, the rotation of pyrophyllite layers was modeled by the position constraining method. Since pyrophyllite includes neutral layers and lacks interlayer cations, it is unable to adsorb water molecules; therefore, only the rotation of dry pyrophyillite was simulated. These simulations indicated that the disordering of this clay mineral is not energetically favorable and leads to the increase in both energy and basal d_{001}-spacing. We also investigated different components of the potential energy (such as electrostatic and VDW terms) and compared them to those of dry montmorillonites. The comparisons confirmed that the interaction of counterions with the clay surface atoms decreases the energy and makes the disordering favorable for the clay.

5.1.3 Swelling of Clay Minerals as a Consequence of Intercalation of Water and Carbon Dioxide

The swelling of smectites was studied by using multiphase Gibbs ensemble Monte Carlo and molecular dynamics simulations consisting of three different systems (binary clay-H_2O, binary clay-CO_2 and ternary clay-H_2O-CO_2 systems). To probe all hydration states in clay minerals, a full range of basal distance (9.5-17.5 Åwith an incremental distance 0.5 Å) was considered. To find stable hydration states, swelling free energy was computed from the normal disjoining pressure of clay layers.

Pure water intercalation to smectite was simulated by the two component clay-water system leading to three hydration states (including dry (0W), first hydration (1W) and second hydration (2W) states), for MMT, suggesting that the 0W state is highly unstable compared to the others and answering why it is almost impossible to find a completely dry clay sample in nature. Next, the clay-CO_2 system was modeled to consider the effect of pure CO_2 adsorption, and we found that in contrast to the previous system, the dry state is the most stable configuration for this system. As a result, we suggested that, while pure water intercalation is thermodynamically favorable, pure carbon dioxide adsorption is energetically demanding in deep underground formations.

We modeled the ternary clay-H_2O-CO_2 system to study CO_2 adsorption in hydrated smectites. We noticed that in this system water behaves similarly to how it does in the

binary clay-water system, while CO_2 has a totally different behavior and extensively depends on the amount of the intercalated water. Maximal CO_2 adsorption takes place at the first and sub-first hydration levels in which the amount of adsorbed water is limited. Hence, CO_2 can form conglomerations in the interlayer space resulting in the remarkably higher amount of adsorbed CO_2 in the mixed system, compared to that of the bulk phase. This confirms that underground smectite reservoirs can be suggested as appropriate candidates to resolve the CO_2 problem of earth's atmosphere.

5.1.4 Effect of Isomorphic Substitution on Swelling

We studied the effect of the isomorphic substitution by considering two kinds of clay minerals, Na-montmorillonite and Na-Beidellite. In the first, the Mg^{2+}/Al^{3+} substitution happens in the clay octahedral sheet, while in the second, the Al^{3+}/Si^{4+} occurs in tetrahedral sheets. These substitutions result in two different swelling profiles including three hydration (0W, 1W and 2W) states for the first clay and two hydration (0W and 1W) states for the second one. The place of substitution not only affects the hydration states of clay, but also influences the distribution of intercalated water and carbon dioxide molecules, and counterions. While, in the MMT-H_2O-CO_2 system, CO_2 conglomerations are moving and disordered in the interlayer space, in the ternary BEI-H_2O-CO_2 system, they are organized, and CO_2 conglomerations avoid isomorphic substitution sites, whereas cation-water complexes position close to those sites. Therefore beidellite could have a strong ability to retain CO_2 molecules. This was also confirmed by the MD diffusion calculations.

5.2 ONGOING AND FUTURE WORK

5.2.1 Response of Pyrophyllite to the Intercalation of Water and CO_2

This is ongoing research in which we study the swelling behavior of other structures to find the best possible structures for carbon sequestration. We have begun to simulate the pyrophyllite structure where there are no isomorphic substitutions in tetrahedral or octahedral sheets, leading to the charge neutrality of clay layers and the lack of interlayer cations.

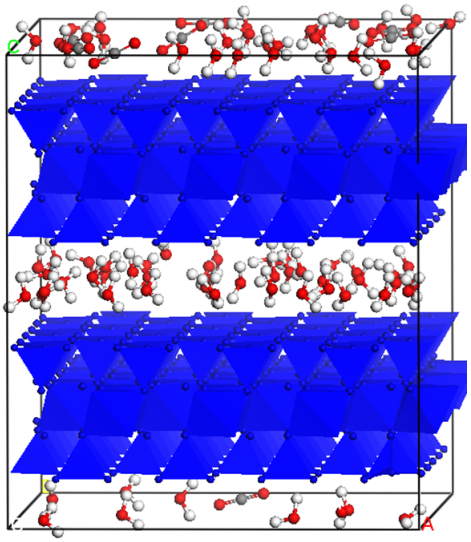

Figure 33: Pyrophyllite phase lacks any interlayer cations and any isomorphic substitutions. Blue color represents pyrophyllite layers, and the color coding of interlayer atoms includes red, white and gray for O, H and C, respectively.

Even though pyrophyllite is non-swelling in the presence of pure water, it might interact differently with pure CO_2 and mixed water-CO_2. The motivation for this work stems from our MMT-H_2O-CO_2 and BEI-H_2O-CO_2 simulations illustrating that montmorillonite involving isomorphic substitutions in octahedral sheets and thus providing less charge exposure in the interlayer space compared to beidellite, favors more CO_2 adsorption and less water intercalation. As a consequence, we are now investigating how the neutral layers of pyrophyllite may affect CO_2 adsorption to the surface.

5.2.2 Role of Open Surfaces in Water and Carbon Dioxide Adsorption

In lab experiments, it is observed that smectite layers are not purely continuous but naturally include discontinuities and breakage due to environmental cracks and defects. As a result, in another ongoing work, we have started investigating not only usual 001 surfaces, but also surfaces in other geometrical directions; such as 010 and 100; which include reactive sites and in the case of exposure to the interlayer species, they may impact the clay behavioral response. Therefore we consider discontinuous layers to study different clay reactive surfaces and to find if they can improve swelling or they might promote shrinking.

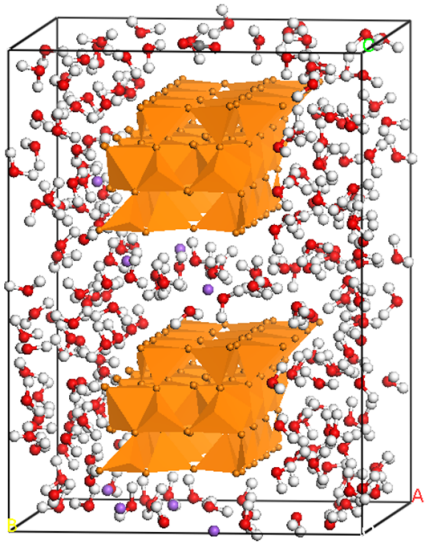

Figure 34: Nonopores involve open surfaces. orange color represents clay layers, and the color coding of interlayer atoms includes purple, red, white and gray for Na, O, H and C, respectively.

APPENDIX

SUPPORTING INFORMATION

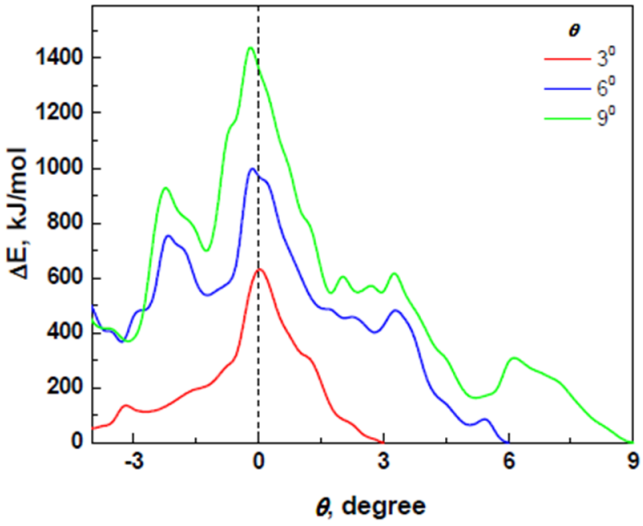

Figure 35: Potential energy change during backward enforced rotation using Na-MMT systems with the 0-0 composition equilibrated at θ = 3, 6, and 9.

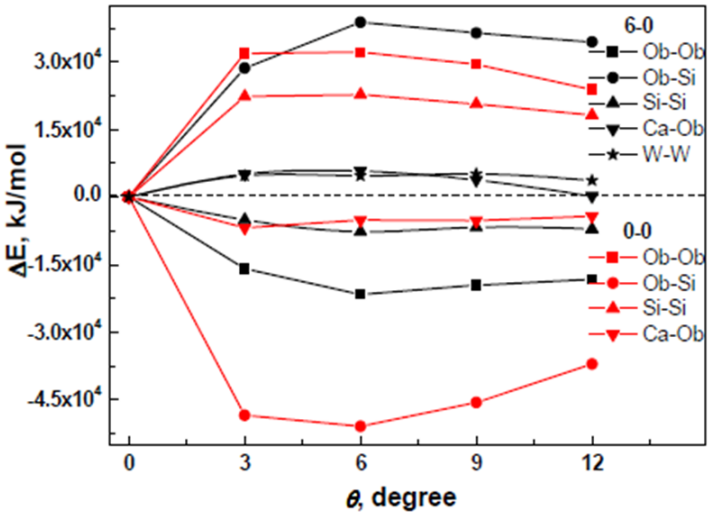

Figure 36: Comparison of real-space electrostatic contributions of various atomic pairs into the relative potential energy as a function of θ for Ca-MMT with the 6-0 (red lines) and 0-0 (black lines) compositions.

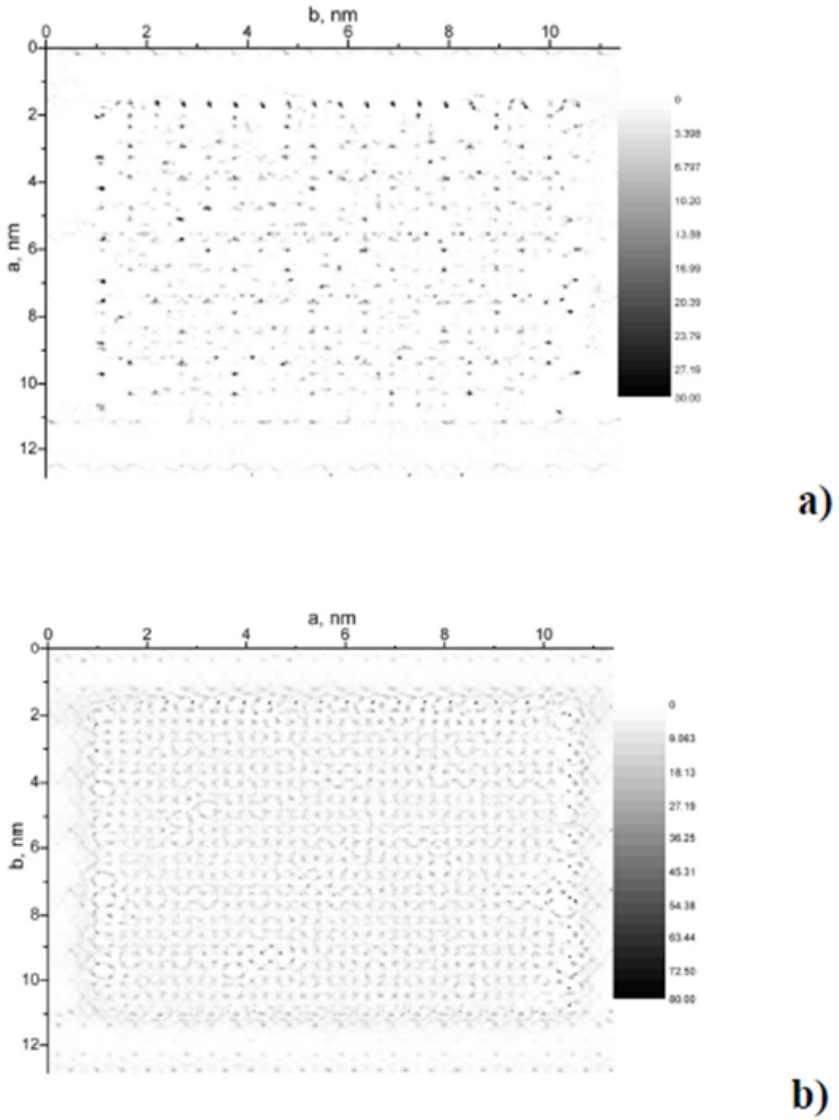

Figure 37: 2D density maps (density in number/ nm^3) of sodium ions (a) and water molecules (b) residing in the interlayer of hydrated Na-MMT with 6-0 composition at $\theta = 0°$(averaged over 5 ns of production run).

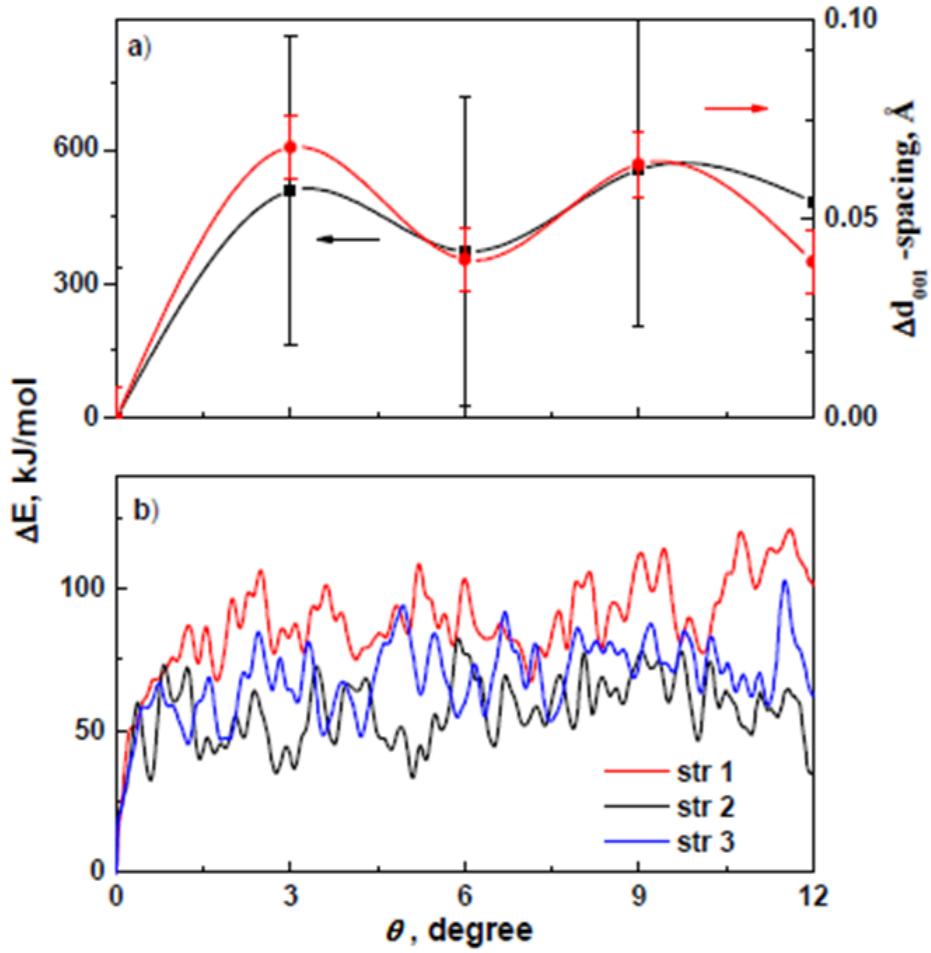

Figure 38: a) Relative potential energy and d_{001}-spacing change in Na-MMT systems with the 14-0 composition as a function of θ obtained using the position constraining method. b) Potential energy changes during enforced rotation for three independently equilibrated Na-MMT systems (strs 1-3) with the 14-0 composition.

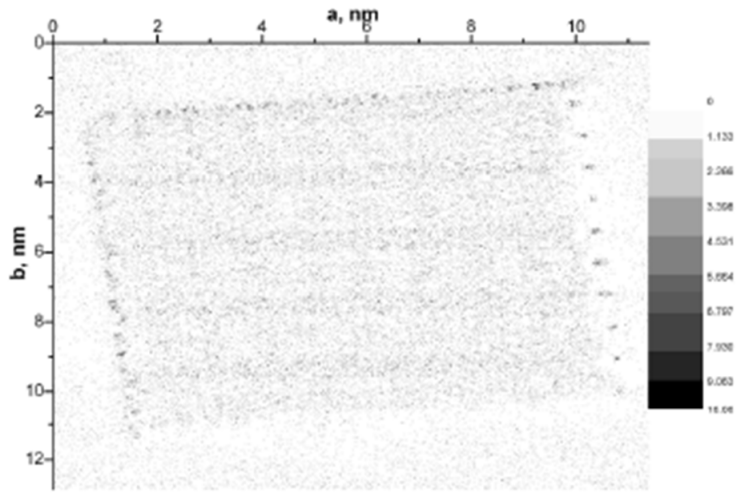

Figure 39: Density distribution computed for sodium ions.

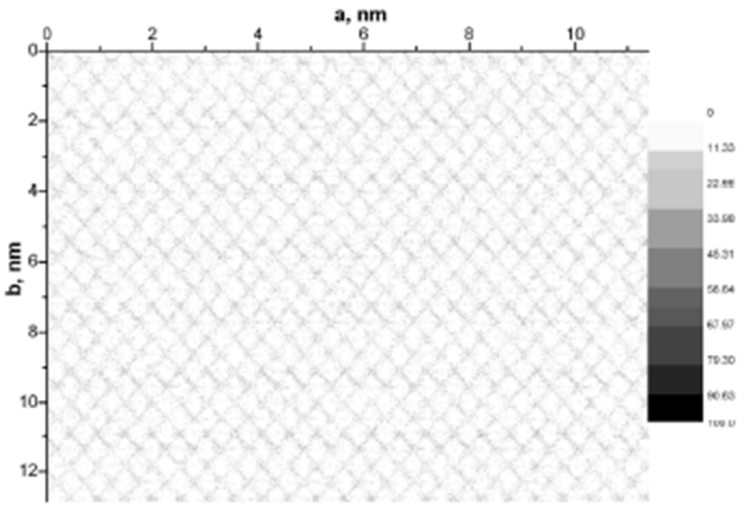

Figure 40: Density distribution computed for the first water layer in a bilayer.

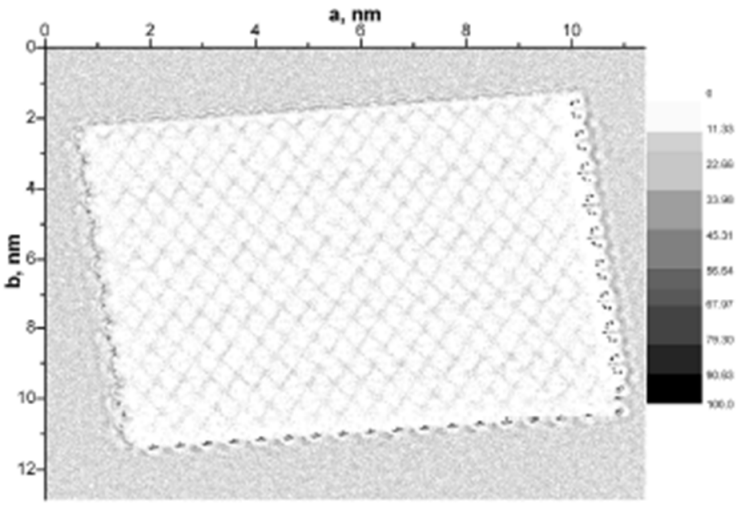

Figure 41: Density distribution computed for the second water layer in a bilayer.

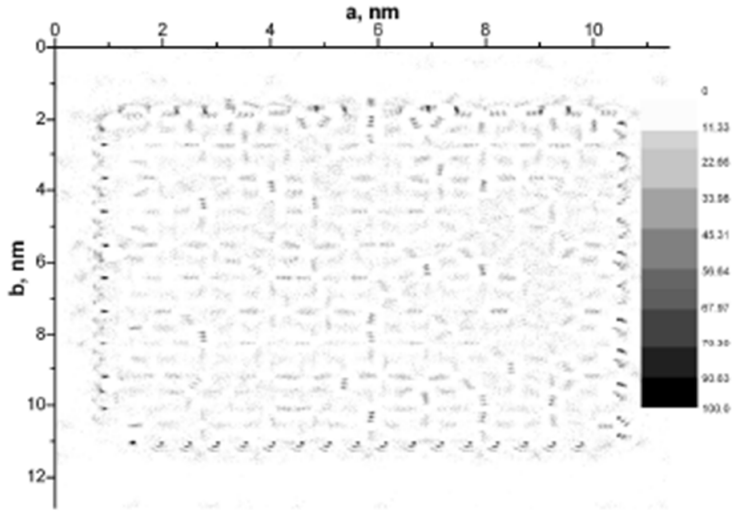

Figure 42: 2D density maps (density in number/ nm^3) of carbon dioxide molecules residing in the interlayer of hydrated Na-MMT with 0-2 composition at $\theta = 0^\circ$ (averaged over 5 ns of production run).

BIBLIOGRAPHY

[1] R. T. Cygan, J. A. Greathouse, H. Heinz, and A. G. Kalinichev, "Molecular models and simulations of layered materials," *Journal of Materials Chemistry*, vol. 19, no. 17, pp. 2470–2481, 2009.

[2] H. C. Greenwell, W. Jones, P. V. Coveney, and S. Stackhouse, "On the application of computer simulation techniques to anionic and cationic clays: A materials chemistry perspective," *Journal of Materials Chemistry*, vol. 16, no. 8, pp. 708–723, 2006.

[3] M. Allen and D. Tildesley, *Computer simulation of liquids. 1987*. New York: Oxford, 1989.

[4] S. M. Benson and D. R. Cole, "CO_2 sequestration in deep sedimentary formations," *Elements*, vol. 4, no. 5, pp. 325–331, 2008.

[5] J. Fripiat, M. Cruz, B. Bohor, and J. Thomas Jr, "Interlamellar adsorption of carbon dioxide by smectites," *Clays and Clay Minerals*, vol. 22, no. 1, pp. 23–30, 1974.

[6] N. Skipper, F.-R. C. Chang, and G. Sposito, "Monte Carlo simulation of interlayer molecular structure in swelling clay minerals. 1. methodology," *Clays and Clay Minerals*, vol. 43, no. 3, pp. 285–293, 1995.

[7] N. Skipper, G. Sposito, and F.-R. C. Chang, "Monte Carlo simulation of interlayer molecular structure in swelling clay minerals. 2. monolayer hydrates," *Clays and Clay minerals*, vol. 43, no. 3, pp. 294–303, 1995.

[8] A. Delville, "Structure and properties of confined liquids: a molecular model of the clay-water interface," *The Journal of Physical Chemistry*, vol. 97, no. 38, pp. 9703–9712, 1993.

[9] F.-R. C. Chang, N. Skipper, and G. Sposito, "Computer simulation of interlayer molecular structure in sodium montmorillonite hydrates," *Langmuir*, vol. 11, no. 7, pp. 2734–2741, 1995.

[10] P. Bordarier, B. Rousseau, and A. H. Fuchs, "Rheology of model confined ultrathin fluid films. i. statistical mechanics of the surface force apparatus experiments," *The Journal of Chemical Physics*, vol. 106, no. 17, pp. 7295–7302, 1997.

[11] V. Marry, P. Turq, T. Cartailler, and D. Levesque, "Microscopic simulation of structure and dynamics of water and counterions in a monohydrated montmorillonite," *The Journal of Chemical Physics*, vol. 117, no. 7, pp. 3454–3463, 2002.

[12] V. Chertkov and I. Ravina, "Effect of interaggregate capillary cracks on the hydraulic conductivity of swelling clay soils," *Water Resources Research*, vol. 37, no. 5, pp. 1245–1256, 2001.

[13] P. Giesting, S. Guggenheim, A. F. Koster van Groos, and A. Busch, "X-ray diffraction study of K-and Ca-exchanged montmorillonites in CO_2 atmospheres," *Environmental Science and Technology*, vol. 46, no. 10, pp. 5623–5630, 2012.

[14] H. T. Schaef, E. S. Ilton, O. Qafoku, P. F. Martin, A. R. Felmy, and K. M. Rosso, "In situ XRD study of Ca^{2+} saturated montmorillonite (STX-1) exposed to anhydrous and wet supercritical carbon dioxide," *International Journal of Greenhouse Gas Control*, vol. 6, pp. 220–229, 2012.

[15] P. Giesting, S. Guggenheim, A. F. Koster van Groos, and A. Busch, "Interaction of carbon dioxide with Na-exchanged montmorillonite at pressures to 640 bars: implications for CO_2 sequestration," *International Journal of Greenhouse Gas Control*, vol. 8, pp. 73–81, 2012.

[16] J. S. Loring, E. S. Ilton, J. Chen, C. J. Thompson, P. F. Martin, P. Bénézeth, K. M. Rosso, A. R. Felmy, and H. T. Schaef, "In situ study of CO_2 and H_2O partitioning between Na-montmorillonite and variably wet supercritical carbon dioxide," *Langmuir*, vol. 30, no. 21, pp. 6120–6128, 2014.

[17] A. Botan, B. Rotenberg, V. Marry, P. Turq, and B. Noetinger, "Carbon dioxide in montmorillonite clay hydrates: thermodynamics, structure, and transport from molecular simulation," *The Journal of Physical Chemistry C*, vol. 114, no. 35, pp. 14962–14969, 2010.

[18] E. M. Myshakin, W. A. Saidi, V. N. Romanov, R. T. Cygan, and K. D. Jordan, "Molecular dynamics simulations of carbon dioxide intercalation in hydrated Na-montmorillonite," *The Journal of Physical Chemistry C*, vol. 117, no. 21, pp. 11028–11039, 2013.

[19] I. Berend, J. Cases, M. Francois, J. Uriot, L. Michot, A. Masion, and F. Thomas, "Mechanism of adsorption and desorption of water vapor by homoionic montmorillonites: 2. the Li, Na, K, Rb and Cs-exchanged forms," *Clays and Clay Minerals*, vol. 43, no. 3, pp. 324–336, 1995.

[20] D. A. Young and D. E. Smith, "Simulations of clay mineral swelling and hydration: dependence upon interlayer ion size and charge," *The Journal of Physical Chemistry B*, vol. 104, no. 39, pp. 9163–9170, 2000.

[21] J.-M. Douillard, S. Lantenois, B. Prelot, J. Zajac, and M. Henry, "Study of the influence of location of substitutions on the surface energy of dioctahedral smectites," *Journal of Colloid and Interface science*, vol. 325, no. 1, pp. 275–281, 2008.

[22] E. J. Hensen and B. Smit, "Why clays swell," *The Journal of Physical Chemistry B*, vol. 106, no. 49, pp. 12664–12667, 2002.

[23] G. Guthrie and R. Reynolds, "A coherent TEM-and XRD-description of mixed-layer illite/smectite," *The Canadian Mineralogist*, vol. 36, no. 6, pp. 1421–1434, 1998.

[24] A. Viani, A. F. Gualtieri, and G. Artioli, "The nature of disorder in montmorillonite by simulation of X-ray powder patterns," *American Mineralogist*, vol. 87, no. 7, pp. 966–975, 2002.

[25] L. Lutterotti, M. Voltolini, H.-R. Wenk, K. Bandyopadhyay, and T. Vanorio, "Texture analysis of a turbostratically disordered Ca-montmorillonite," *American Mineralogist*, vol. 95, no. 1, pp. 98–103, 2010.

[26] J. Titiloye and N. Skipper, "Computer simulation of the structure and dynamics of methane in hydrated Na-smectite clay," *Chemical Physics Letters*, vol. 329, no. 1, pp. 23–28, 2000.

[27] J. O. Titiloye and N. T. Skipper, "Monte Carlo and molecular dynamics simulations of methane in potassium montmorillonite clay hydrates at elevated pressures and temperatures," *Journal of Colloid and Interface Science*, vol. 282, no. 2, pp. 422–427, 2005.

[28] X.-D. Liu and X.-C. Lu, "A thermodynamic understanding of clay-swelling inhibition by potassium ions," *Angewandte Chemie International Edition*, vol. 45, no. 38, pp. 6300–6303, 2006.

[29] B. Rotenberg, J.-P. Morel, V. Marry, P. Turq, and N. Morel-Desrosiers, "On the driving force of cation exchange in clays: Insights from combined microcalorimetry experiments and molecular simulation," *Geochimica et Cosmochimica Acta*, vol. 73, no. 14, pp. 4034–4044, 2009.

[30] D. Tunega, B. A. Goodman, G. Haberhauer, T. G. Reichenauer, M. H. Gerzabek, and H. Lischka, "Ab initio calculations of relative stabilities of different structural arrangements in dioctahedral phyllosilicates," *Clays and Clay minerals*, vol. 55, no. 2, pp. 220–232, 2007.

[31] B. Minisini and F. Tsobnang, "Ab initio comparative study of montmorillonite structural models," *Applied Surface Science*, vol. 242, no. 1, pp. 21–28, 2005.

[32] V. K. Voora, W. Al-Saidi, and K. D. Jordan, "Density functional theory study of pyrophyllite and M-montmorillonites (M= Li, Na, K, Mg, and Ca): Role of dispersion

interactions," *The Journal of Physical Chemistry A*, vol. 115, no. 34, pp. 9695–9703, 2011.

[33] C. I. Sainz-Díaz, E. Escamilla-Roa, and A. Hernández-Laguna, "Quantum mechanical calculations of trans-vacant and cis-vacant polymorphism in dioctahedral 2:1 phyllosilicates," *American Mineralogist*, vol. 90, no. 11-12, pp. 1827–1834, 2005.

[34] R. Mooney, A. Keenan, and L. Wood, "Adsorption of water vapor by montmorillonite. i. heat of desorption and application of BET theory1," *Journal of the American Chemical Society*, vol. 74, no. 6, pp. 1367–1371, 1952.

[35] J. Cases, I. Bérend, G. Besson, M. Francois, J. Uriot, F. Thomas, and J. Poirier, "Mechanism of adsorption and desorption of water vapor by homoionic montmorillonite. 1. the sodium-exchanged form," *Langmuir*, vol. 8, no. 11, pp. 2730–2739, 1992.

[36] S. Karaborni, B. Smit, W. Heidug, J. Urai, and E. Van Oort, "The swelling of clays: molecular simulations of the hydration of montmorillonite," *Science*, vol. 271, p. 1102, 1996.

[37] M. Chávez-Páez, K. Van Workum, L. De Pablo, and J. J. de Pablo, "Monte Carlo simulations of wyoming sodium montmorillonite hydrates," *The Journal of Chemical Physics*, vol. 114, no. 3, pp. 1405–1413, 2001.

[38] R. Anderson, I. Ratcliffe, H. Greenwell, P. Williams, S. Cliffe, and P. Coveney, "Clay swelling, a challenge in the oil field," *Earth-Science Reviews*, vol. 98, no. 3, pp. 201–216, 2010.

[39] G. Sposito, *The chemistry of soils*. Oxford university press, 2008.

[40] D. Diestler, M. Schoen, J. E. Curry, and J. H. Cushman, "Thermodynamics of a fluid confined to a slit pore with structured walls," *The Journal of Chemical Physics*, vol. 100, no. 12, pp. 9140–9146, 1994.

[41] D. E. Smith, "Molecular computer simulations of the swelling properties and interlayer structure of cesium montmorillonite," *Langmuir*, vol. 14, no. 20, pp. 5959–5967, 1998.

[42] H. Goldstein and C. Poole, *Classical mechanics. Classical mechanics*. San Francisco: Addison-Wesley, 2002.

[43] W. Van Gunsteren and H. Berendsen, "A leap-frog algorithm for stochastic dynamics," *Molecular Simulation*, vol. 1, no. 3, pp. 173–185, 1988.

[44] H. C. Andersen, "Molecular dynamics simulations at constant pressure and/or temperature," *The Journal of Chemical Physics*, vol. 72, no. 4, pp. 2384–2393, 1980.

[45] H. J. Berendsen, J. P. M. Postma, W. F. van Gunsteren, A. DiNola, and J. Haak, "Molecular dynamics with coupling to an external bath," *The Journal of Chemical Physics*, vol. 81, no. 8, pp. 3684–3690, 1984.

[46] W. G. Hoover, "Canonical dynamics: equilibrium phase-space distributions," *Physical Review A*, vol. 31, no. 3, p. 1695, 1985.

[47] M. Parrinello and A. Rahman, "Polymorphic transitions in single crystals: A new molecular dynamics method," *Journal of Applied Physics*, vol. 52, no. 12, pp. 7182–7190, 1981.

[48] N. Metropolis, A. W. Rosenbluth, M. N. Rosenbluth, A. H. Teller, and E. Teller, "Equation of state calculations by fast computing machines," *The Journal of Chemical Physics*, vol. 21, no. 6, pp. 1087–1092, 1953.

[49] D. Frenkel and B. Smit, *Understanding molecular simulation: from algorithms to applications*, vol. 1. Academic press, 2001.

[50] A. Z. Panagiotopoulos, "Adsorption and capillary condensation of fluids in cylindrical pores by Monte Carlo simulation in the Gibbs ensemble," *Molecular Physics*, vol. 62, no. 3, pp. 701–719, 1987.

[51] S. C. McGrother and K. E. Gubbins, "Constant pressure Gibbs ensemble Monte Carlo simulations of adsorption into narrow pores," *Molecular Physics*, vol. 97, no. 8, pp. 955–965, 1999.

[52] R. T. Cygan, J.-J. Liang, and A. G. Kalinichev, "Molecular models of hydroxide, oxyhydroxide, and clay phases and the development of a general force field," *The Journal of Physical Chemistry B*, vol. 108, no. 4, pp. 1255–1266, 2004.

[53] R. T. Cygan, V. N. Romanov, and E. M. Myshakin, "Molecular simulation of carbon dioxide capture by montmorillonite using an accurate and flexible force field," *The Journal of Physical Chemistry C*, vol. 116, no. 24, pp. 13079–13091, 2012.

[54] H. J. Berendsen, J. P. Postma, W. F. van Gunsteren, and J. Hermans, "Interaction models for water in relation to protein hydration," in *Intermolecular Forces*, pp. 331–342, Springer, 1981.

[55] "Geologic carbon dioxide storage, NETL." http://www.netl.doe.gov/research/coal/carbon-storage/research-and-development/storage. Accessed: 2014-06-30.

[56] P. A. Allen and J. R. Allen, *Basin analysis: principles and application*. Blackwell Publishing, 2005.

[57] M. Abdou and H. Ahmaed, "Evaluation of low-solids mud reological behavior during drilling shale formation and their effect on the pay zone productivity," *Petroleum Science and Technology*, vol. 28, no. 9, pp. 934–945, 2010.

[58] E. S. Ilton, H. T. Schaef, O. Qafoku, K. M. Rosso, and A. R. Felmy, "In situ X-ray diffraction study of Na^+ saturated montmorillonite exposed to variably wet super critical CO_2," *Environmental Science and Technology*, vol. 46, no. 7, pp. 4241–4248, 2012.

[59] J. H. Kwak, J. Z. Hu, R. V. Turcu, K. M. Rosso, E. S. Ilton, C. Wang, J. A. Sears, M. H. Engelhard, A. R. Felmy, and D. W. Hoyt, "The role of H_2O in the carbonation of forsterite in supercritical CO_2," *International Journal of Greenhouse Gas Control*, vol. 5, no. 4, pp. 1081–1092, 2011.

[60] G. Rother, E. S. Ilton, D. Wallacher, T. Hauβ, H. T. Schaef, O. Qafoku, K. M. Rosso, A. R. Felmy, E. G. Krukowski, and Stack, "CO_2 sorption to subsingle hydration layer montmorillonite clay studied by excess sorption and neutron diffraction measurements," *Environmental Science and Technology*, vol. 47, no. 1, pp. 205–211, 2012.

[61] V. N. Romanov, "Evidence of irreversible CO_2 intercalation in montmorillonite," *International Journal of Greenhouse Gas Control*, vol. 14, pp. 220–226, 2013.

[62] V. Romanov, B. Howard, R. Lynn, R. Warzinski, T. Hur, E. Myshakin, C. Lopano, V. Voora, W. Al-Saidi, K. Jordan, *et al.*, "CO_2 interaction with geomaterials," in *AGU Fall Meeting Abstracts*, vol. 1, p. 01, 2010.

[63] J. S. Loring, H. T. Schaef, R. V. Turcu, C. J. Thompson, Q. R. Miller, P. F. Martin, J. Hu, D. W. Hoyt, O. Qafoku, E. S. Ilton, *et al.*, "In situ molecular spectroscopic evidence for CO_2 intercalation into montmorillonite in supercritical carbon dioxide," *Langmuir*, vol. 28, no. 18, pp. 7125–7128, 2012.

[64] T.-B. Hur, J. P. Baltrus, B. H. Howard, W. P. Harbert, and V. N. Romanov, "Carbonate formation in wyoming montmorillonite under high pressure carbon dioxide," *International Journal of Greenhouse Gas Control*, vol. 13, pp. 149–155, 2013.

[65] M. Fu, Z. Zhang, and P. Low, "Changes in the properties of a montmorillonite-water system during the adsorption and desorption of water: hysteresis," *Clays and Clay Minerals*, vol. 38, no. 5, pp. 485–492, 1990.

[66] J. G. Harris and K. H. Yung, "Carbon dioxide's liquid-vapor coexistence curve and critical properties as predicted by a simple molecular model," *The Journal of Physical Chemistry*, vol. 99, no. 31, pp. 12021–12024, 1995.

[67] X. Yang and C. Zhang, "Structure and diffusion behavior of dense carbon dioxide fluid in clay-like slit pores by molecular dynamics simulation," *Chemical Physics Letters*, vol. 407, no. 4, pp. 427–432, 2005.

[68] X. Peng, J. Zhao, and D. Cao, "Adsorption of carbon dioxide of 1-site and 3-site models in pillared clays: A Gibbs ensemble Monte Carlo simulation," *Journal of Colloid and Interface Science*, vol. 310, no. 2, pp. 391–401, 2007.

[69] D. R. Cole, A. A. Chialvo, G. Rother, L. Vlcek, and P. T. Cummings, "Supercritical fluid behavior at nanoscale interfaces: Implications for CO_2 sequestration in geologic formations," *Philosophical Magazine*, vol. 90, no. 17-18, pp. 2339–2363, 2010.

[70] M. Krishnan, M. Saharay, and R. J. Kirkpatrick, "Molecular dynamics modeling of CO_2 and poly (ethylene glycol) in montmorillonite: The structure of clay–polymer composites and the incorporation of CO_2," *The Journal of Physical Chemistry C*, vol. 117, no. 40, pp. 20592–20609, 2013.

[71] L. M. Hamm, I. C. Bourg, A. F. Wallace, and B. Rotenberg, "Molecular simulation of CO_2-and CO_3-brine-mineral systems," *Reviews in Mineralogy and Geochemistry*, vol. 77, no. 1, pp. 189–228, 2013.

[72] D. M. Moore and R. C. Reynolds, *X-ray Diffraction and the Identification and Analysis of Clay Minerals*, vol. 378. Oxford university press Oxford, 1989.

[73] D. R. Veblen, G. D. Guthrie, K. J. Livi, and R. C. Reynolds, "High-resolution transmission electron microscopy and electron diffraction of mixed-layer illite/smectite: Experimental results," *Clays and Clay Minerals*, vol. 38, no. 1, pp. 1–13, 1990.

[74] N. Güven, "Montmorillonite: Electron-optical observations," *Science*, vol. 181, no. 4104, pp. 1049–1051, 1973.

[75] J. Mering, "Electron-optical study of smectites," *Clays and Clay Minerals*, vol. 15, pp. 3–25, 1967.

[76] R. Reynolds, "X-ray diffraction studies of illite/smectite from rocks,< 1 m randomly oriented powders, and< 1 m oriented powder aggregates: The absence of laboratory-induced artifacts," *Clays and Clay Minerals*, vol. 40, pp. 387–387, 1992.

[77] B. H. D. van der Spoel, E. Lindahl and the GROMACS development team, "GROMACS user manual version 4.6.5, www.gromacs.org," 2013.

[78] L. Vlcek, A. A. Chialvo, and D. R. Cole, "Optimized unlike-pair interactions for water–carbon dioxide mixtures described by the SPC/E and EPM2 models," *The Journal of Physical Chemistry B*, vol. 115, no. 27, pp. 8775–8784, 2011.

[79] S. Nosé and M. Klein, "Constant pressure molecular dynamics for molecular systems," *Molecular Physics*, vol. 50, no. 5, pp. 1055–1076, 1983.

[80] S. Nosé, "A molecular dynamics method for simulations in the canonical ensemble," *Molecular Physics*, vol. 52, no. 2, pp. 255–268, 1984.

[81] S. I. Tsipursky and V. Drits, "The distribution of octahedral cations in the 2:1 layers of dioctahedral smectites studied by oblique-texture electron diffraction," *Clay Minerals*, vol. 19, no. 2, pp. 177–193, 1984.

[82] C. Kutzner, J. Czub, and H. Grubmuller, "Keep it flexible: Driving macromolecular rotary motions in atomistic simulations with ROMACS," *Journal of Chemical Theory and Computation*, vol. 7, no. 5, pp. 1381–1393, 2011.

[83] E. Ferrage, B. Lanson, B. A. Sakharov, and V. A. Drits, "Investigation of smectite hydration properties by modeling experimental X-ray diffraction patterns: Part i. montmorillonite hydration properties," *American Mineralogist*, vol. 90, no. 8-9, pp. 1358–1374, 2005.

[84] E. Abramova, I. Lapides, and S. Yariv, "Thermo-XRD investigation of monoionic montmorillonites mechanochemically treated with urea," *Journal of Thermal Analysis and Calorimetry*, vol. 90, no. 1, pp. 99–106, 2007.

[85] S. Morodome and K. Kawamura, "In situ X-ray diffraction study of the swelling of montmorillonite as affected by exchangeable cations and temperature," *Clays and Clay Minerals*, vol. 59, no. 2, pp. 165–175, 2011.

[86] E. Boek, P. Coveney, and N. Skipper, "Molecular modeling of clay hydration: a study of hysteresis loops in the swelling curves of sodium montmorillonites," *Langmuir*, vol. 11, no. 12, pp. 4629–4631, 1995.

[87] T. J. Tambach, P. G. Bolhuis, and B. Smit, "A molecular mechanism of hysteresis in clay swelling," *Angewandte Chemie*, vol. 116, no. 20, pp. 2704–2706, 2004.

[88] C. P. Morrow, A. O. Yazaydin, M. Krishnan, G. M. Bowers, A. G. Kalinichev, and R. J. Kirkpatrick, "Structure, energetics, and dynamics of smectite clay interlayer hydration: molecular dynamics and metadynamics investigation of Na-hectorite," *The Journal of Physical Chemistry C*, vol. 117, no. 10, pp. 5172–5187, 2013.

[89] Z. Jinhong, L. Xiancai, Z. Jianxi, L. Xiandong, W. Jingming, Z. Qing, Y. Peng, and H. Hongping, "Interlayer structure and dynamics of HDTMA-intercalated rectorite with and without water: a molecular dynamics study," *The Journal of Physical Chemistry C*, vol. 116, no. 24, pp. 13071–13078, 2012.

[90] H. D. Whitley and D. E. Smith, "Free energy, energy, and entropy of swelling in Cs-, Na-, and Sr-montmorillonite clays," *The Journal of Chemical Physics*, vol. 120, no. 11, pp. 5387–5395, 2004.

[91] D. E. Smith, Y. Wang, and H. D. Whitley, "Molecular simulations of hydration and swelling in clay minerals," *Fluid Phase Equilibria*, vol. 222, pp. 189–194, 2004.

[92] J. L. Suter, M. Sprik, and E. S. Boek, "Free energies of absorption of alkali ions onto beidellite and montmorillonite surfaces from constrained molecular dynamics simulations," *Geochimica et Cosmochimica Acta*, vol. 91, pp. 109–119, 2012.

[93] D. van der Spoel, P. J. van Maaren, P. Larsson, and N. Timneanu, "Thermodynamics of hydrogen bonding in hydrophilic and hydrophobic media," *The Journal of Physical Chemistry B*, vol. 110, no. 9, pp. 4393–4398, 2006.

[94] G. Zhang, W. A. Al-Saidi, E. M. Myshakin, and K. D. Jordan, "Dispersion-corrected density functional theory and classical force field calculations of water loading on a

pyrophyllite(001) surface," *The Journal of Physical Chemistry C*, vol. 116, pp. 17134–17141, July 2012.

[95] B. Rotenberg, A. J. Patel, and D. Chandler, "Molecular explanation for why talc surfaces can be both hydrophilic and hydrophobic," *Journal of the American Chemical Society*, vol. 133, no. 50, pp. 20521–20527, 2011.

[96] V. Marry, B. Rotenberg, and P. Turq, "Structure and dynamics of water at a clay surface from molecular dynamics simulation," *Physical Chemistry Chemical Physics*, vol. 10, no. 32, pp. 4802–4813, 2008.

[97] P. Nadeau, M. Wilson, W. McHardy, and J. Tait, "Interstratified clays as fundamental particles," *Science*, vol. 225, no. 4665, pp. 923–925, 1984.

[98] P. Nadeau, "The physical dimensions of fundamental clay particles," *Clay Minerals*, vol. 20, no. 4, p. 499, 1985.

[99] B. Rotenberg, V. Marry, R. Vuilleumier, N. Malikova, C. Simon, and P. Turq, "Water and ions in clays: Unraveling the interlayer/micropore exchange using molecular dynamics," *Geochimica et Cosmochimica Acta*, vol. 71, no. 21, pp. 5089–5101, 2007.

[100] R. P. Tenório, M. Engelsberg, J. O. Fossum, and G. J. da Silva, "Intercalated water in synthetic fluorhectorite clay," *Langmuir*, vol. 26, no. 12, pp. 9703–9709, 2010.

[101] T. J. Tambach, P. G. Bolhuis, E. J. Hensen, and B. Smit, "Hysteresis in clay swelling induced by hydrogen bonding: accurate prediction of swelling states," *Langmuir*, vol. 22, no. 3, pp. 1223–1234, 2006.

[102] T. Sato, T. Watanabe, and R. Otsuka, "Effects of layer charge, charge location, and energy change on expansion properties of dioctahedral smectites," *Clays and Clay Minerals*, vol. 40, no. 1, pp. 103–113, 1992.

[103] E. Ferrage, C. A. Kirk, G. Cressey, and J. Cuadros, "Dehydration of Ca-montmorillonite at the crystal scale. part i: Structure evolution," *American Mineralogist*, vol. 92, no. 7, pp. 994–1006, 2007.

[104] J. Houghton, *Global warming: the complete briefing*. Cambridge University Press, 2009.

[105] K. Norrish, "The swelling of montmorillonite," *Discussions of the Faraday Society*, vol. 18, pp. 120–134, 1954.

[106] N. Skipper, K. Refson, and J. McConnell, "Computer simulation of interlayer water in 2:1 clays," *The Journal of Chemical Physics*, vol. 94, no. 11, pp. 7434–7445, 1991.

[107] A. Delville, "Modeling the clay-water interface," *Langmuir*, vol. 7, no. 3, pp. 547–555, 1991.

[108] A. Delville, "Structure of liquids at a solid interface: an application to the swelling of clay by water," *Langmuir*, vol. 8, no. 7, pp. 1796–1805, 1992.

[109] B. J. Teppen, K. Rasmussen, P. M. Bertsch, D. M. Miller, and L. Schaefer, "Molecular dynamics modeling of clay minerals. 1. gibbsite, kaolinite, pyrophyllite, and beidellite," *The Journal of Physical Chemistry B*, vol. 101, no. 9, pp. 1579–1587, 1997.

[110] J. A. Greathouse and R. T. Cygan, "Water structure and aqueous uranyl (VI) adsorption equilibria onto external surfaces of beidellite, montmorillonite, and pyrophyllite: results from molecular simulations," *Environmental Science and Technology*, vol. 40, no. 12, pp. 3865–3871, 2006.

[111] R. Calvet, *Hydratation de la montmorillonite et diffusion des cations compensateurs*. Université VI, Faculté des Sciences Physiques, 1972.

[112] G. Odriozola, J. Aguilar, and J. López-Lemus, "Na-montmorillonite hydrates under ethane rich reservoirs: NPzzT and μPzzT simulations," *The Journal of Chemical Physics*, vol. 121, no. 9, pp. 4266–4275, 2004.

[113] P. Billemont, B. Coasne, and G. De Weireld, "An experimental and molecular simulation study of the adsorption of carbon dioxide and methane in nanoporous carbons in the presence of water," *Langmuir*, vol. 27, no. 3, pp. 1015–1024, 2010.

[114] E. Ferrage, B. A. Sakharov, L. J. Michot, A. Delville, A. Bauer, B. Lanson, S. Grangeon, G. Frapper, M. Jiménez-Ruiz, and G. J. Cuello, "Hydration properties and interlayer organization of water and ions in synthetic Na-smectite with tetrahedral layer charge. part 2. toward a precise coupling between molecular simulations and diffraction data," *The Journal of Physical Chemistry C*, vol. 115, no. 5, pp. 1867–1881, 2011.

[115] S. V. Churakov, "Mobility of Na and Cs on montmorillonite surface under partially saturated conditions," *Environmental Science and Technology*, vol. 47, no. 17, pp. 9816–9823, 2013.

[116] E. M. Myshakin, M. Makaremi, V. N. Romanov, K. D. Jordan, and G. D. Guthrie, "Molecular dynamics simulations of turbostratic dry and hydrated montmorillonite with intercalated carbon dioxide," *The Journal of Physical Chemistry A*, vol. 118, no. 35, pp. 7454–7468, 2014.

[117] J. C. Lopes and D. Tildesley, "Multiphase equilibria using the Gibbs ensemble Monte Carlo method," *Molecular Physics*, vol. 92, no. 2, pp. 187–196, 1997.

[118] M. G. Martin and J. I. Siepmann, "Calculating Gibbs free energies of transfer from Gibbs ensemble Monte Carlo simulations," *Theoretical Chemistry Accounts*, vol. 99, no. 5, pp. 347–350, 1998.

[119] A. Liu and T. L. Beck, "Vapor-liquid equilibria of binary and ternary mixtures containing methane, ethane, and carbon dioxide from Gibbs ensemble simulations," *The Journal of Physical Chemistry B*, vol. 102, no. 39, pp. 7627–7631, 1998.

[120] T. Kristóf, J. Vorholz, and G. Maurer, "Molecular simulation of the high-pressure phase equilibrium of the system carbon dioxide-methanol-water," *The Journal of Physical Chemistry B*, vol. 106, no. 30, pp. 7547–7553, 2002.

[121] J. Carrero-Mantilla and M. Llano-Restrepo, "Vapor–liquid equilibria of the binary mixtures nitrogen+methane, nitrogen+ethane and nitrogen+carbon dioxide, and the ternary mixture nitrogen+methane+ethane from Gibbs-ensemble molecular simulation," *Fluid Phase Equilibria*, vol. 208, no. 1, pp. 155–169, 2003.

[122] L. Zhang and J. I. Siepmann, "Pressure dependence of the vapor-liquid-liquid phase behavior in ternary mixtures consisting of n-alkanes, n-perfluoroalkanes, and carbon dioxide," *The Journal of Physical Chemistry B*, vol. 109, no. 7, pp. 2911–2919, 2005.

[123] W. Loewenstein, "The distribution of aluminum in the tetrahedra of silicates and aluminates," *American Mineralogist*, vol. 39, no. 1-2, pp. 92–96, 1954.

[124] R. Wiebe, "The binary system carbon dioxide-water under pressure.," *Chemical Reviews*, vol. 29, no. 3, pp. 475–481, 1941.

[125] P. C. Gillespie and G. M. Wilson, *Vapor-liquid and liquid-liquid equilibria: water-methane, water-carbon dioxide, water-hydrogen sulfide, water-npentane, water-methane-npentane*. Gas Processors Association, 1982.

[126] J. Vorholz, V. Harismiadis, B. Rumpf, A. Panagiotopoulos, and G. Maurer, "Vapor+liquid equilibrium of water, carbon dioxide, and the binary system, water+carbon dioxide, from molecular simulation," *Fluid Phase Equilibria*, vol. 170, no. 2, pp. 203–234, 2000.

[127] I. McDonald, "NPT-ensemble Monte Carlo calculations for binary liquid mixtures," *Molecular Physics*, vol. 23, no. 1, pp. 41–58, 1972.

[128] G. Mooij, D. Frenkel, and B. Smit, "Direct simulation of phase equilibria of chain molecules," *Journal of Physics: Condensed Matter*, vol. 4, no. 16, p. L255, 1992.

[129] M. G. Martin and A. L. Frischknecht, "Using arbitrary trial distributions to improve intramolecular sampling in configurational-bias Monte Carlo," *Molecular Physics*, vol. 104, no. 15, pp. 2439–2456, 2006.

[130] "MCCCS Towhee version 7.0.6." http://towhee.sourceforge.net. Accessed: 2014-02-1.

[131] J. T. Kloprogge, J. B. H. Jansen, and J. W. Geus, "Characterization of synthetic Na-beidellite," *Clays and Clay Minerals*, vol. 38, no. 4, pp. 409–414, 1990.

[132] S. Ansell, A. Barnes, P. Mason, G. Neilson, and S. Ramos, "X-ray and neutron scattering studies of the hydration structure of alkali ions in concentrated aqueous solutions," *Biophysical Chemistry*, vol. 124, no. 3, pp. 171–179, 2006.

[133] A. K. Soper and K. Weckström, "Ion solvation and water structure in potassium halide aqueous solutions," *Biophysical Chemistry*, vol. 124, no. 3, pp. 180–191, 2006.

[134] J. Khalack and A. Lyubartsev, "Car-Parrinello molecular dynamics simulations of Na^+-Cl^- ion pair in liquid water," *Condensed Matter Physics*, vol. 7, pp. 683–698, 2004.

[135] E. J. Palin, M. T. Dove, A. Hernández-Laguna, and C. I. Sainz-Díaz, "A computational investigation of the Al/Fe/Mg order-disorder behavior in the dioctahedral sheet of phyllosilicates," *American Mineralogist*, vol. 89, no. 1, pp. 164–175, 2004.

[136] F. Muller, G. Besson, A. Manceau, and V.-A. Drits, "Distribution of isomorphous cations within octahedral sheets in montmorillonite from Camp-Bertaux," *Physics and Chemistry of Minerals*, vol. 24, no. 3, pp. 159–166, 1997.

[137] E. Palin, M. Dove, S. Redfern, A. Bosenick, C. Sainz-Diaz, and M. Warren, "Computational study of tetrahedral Al-Si ordering in muscovite," *Physics and Chemistry of Minerals*, vol. 28, no. 8, pp. 534–544, 2001.

[138] V. Marry, E. Dubois, N. Malikova, S. Durand-Vidal, S. Longeville, and J. Breu, "Water dynamics in hectorite clays: infuence of temperature studied by coupling neutron spin echo and molecular dynamics," *Environmental Science and Technology*, vol. 45, no. 7, pp. 2850–2855, 2011.

[139] V. Marry, E. Dubois, N. Malikova, J. Breu, and W. Haussler, "Anisotropy of water dynamics in clays: Insights from molecular simulations for experimental QENS analysis," *The Journal of Physical Chemistry C*, vol. 117, no. 29, pp. 15106–15115, 2013.

[140] N. Malikova, A. Cadene, E. Dubois, V. Marry, S. Durand-Vidal, P. Turq, J. Breu, S. Longeville, and J.-M. Zanotti, "Water diffusion in a synthetic hectorite clay studied by quasi-elastic neutron scattering," *The Journal of Physical Chemistry C*, vol. 111, no. 47, pp. 17603–17611, 2007.

[141] M. Holz, S. R. Heil, and A. Sacco, "Temperature-dependent self-diffusion coefficients of water and six selected molecular liquids for calibration in accurate 1H NMR PFG measurements," *Physical Chemistry Chemical Physics*, vol. 2, no. 20, pp. 4740–4742, 2000.

[142] E. Lindeberg and D. Wessel-Berg, "Vertical convection in an aquifer column under a gas cap of CO_2," *Energy Conversion and Management*, vol. 38, pp. S229–S234, 1997.

[143] R. Stokes and R. Robinson, "Electrolyte solutions," *Butterworths, London*, pp. 393–429, 1959.

[144] T. Kozaki, A. Fujishima, S. Sato, and H. Ohashi, "Self-diffusion of sodium ions in compacted sodium montmorillonite," *Nuclear Technology*, vol. 121, no. 1, pp. 63–69, 1998.